Monte Carlo Modeling of the Sensitivity of X-ray Photoconductors

A Thesis
Submitted to the College of Graduate Studies and Research
in Partial Fulfillment of the Requirements
for the Degree of
Master of Science
in the Department of Electrical Engineering
University of Saskatchewan

By

Mohammad Yunus
Saskatoon, Saskatchewan

COPYRIGHT

Head of the Department of Electrical Engineering
University of Saskatchewan
Saskatoon, SK, S7N 5A9

ABSTRACT

The sensitivity reduction or ghosting mechanism of x-ray photoconductor is studied based on Monte Carlo simulation techniques. We have calculated the sensitivity reduction for different detector operating conditions (applied electric field, x-ray spectrum and photoconductor thickness) and for different levels of carrier trapping. We have analyzed the effect of photoconductor biasing (positive or negative) on ghosting. The following effects are taken into account in modeling the ghosting phenomena: (i) recombination between trapped and oppositely charged drifting carriers, (ii) trap filling, (iii) nonuniform electric field, (iv) detrapping of trapped holes, and (v) x-ray induced trap generation.

Our calculation shows that not only the recombination between trapped and oppositely charged drifting carriers but the x-ray induced trap generation is also responsible for ghosting in photoconductor based x-ray image detectors. Moreover not all the trapped carriers take part in recombination; rather only a fraction of the trapped carriers are involved in recombination. Electric field also plays an important role in ghosting calculations via the electron hole pair generation mechanism. Trap filling has also non trivial effects on ghosting.

The simulation results show that the amount of ghosting strongly depends on the applied electric field. Ghosting increases with decreasing applied electric field and vice versa. It is observed that ghosting is higher at high carrier trapping level than at low trapping level. Again ghosting is more pronounced in chest radiographic detector than mammographic detector. In chest radiographic detector, carrier trapping is high due to greater thickness hence recombination and electric field effects are prominent in chest radiographic detector. Biasing dependent ghosting depends on the carrier mobility lifetime product. For positively biased detectors, ghosting is less if the mobility lifetime product of hole is higher than that of electron and vice versa for negatively biased detectors. It also appears that the use of only recombination to calculate ghosting, as believed the primary source of ghosting in some literatures, will lead to significant error in the calculation of ghosting.

ACKNOWLEDGEMENTS

I am deeply grateful to my supervisor, Professor S. O. Kasap, for his continuous guidance, suggestions, encouragement, wholehearted supervision, and financial support throughout the progress of the work. This work could never be materialized without his help. I would like to thank Mr. Zahangir Kabir for many insightful discussions. I am grateful to Zahid Shakoor, Shaikh Hasibul Majid and all my colleagues in our lab for their support, encouragement and helpful discussion. Finally I would like to express my appreciation to Anrad Corporation, Canada and the University of Saskatchewan for the financial support I have received during the course of this thesis.

TABLE OF CONTENTS

COPYRIGHT ………………………………………………………………………….. i
ABSTRACT ……………………………………………………………………………ii
ACKNOWLEDGEMENTS ……………………………………………………….. iii
TABLE OF CONTENTS ………………………………………………………………iv
LIST OF FIGURS ………………………………………………………………………...vi
LIST OF TABLES……………………………………………………………………x
LIST OF ABBREVIATIONS …………………………………………………….xi

1. Introduction 1
- 1.1 X-ray Imaging ………………………………………………………. 2
- 1.2 Film based Radiography ……………………………………………. 4
- 1.3 Digital Radiography ………………………………………………… 5
  - 1.3.1 Phosphor based Detectors …………………………………….6
  - 1.3.2 Photostimulable Phosphor based Detectors …………………….8
  - 1.3.3 Image Intensifier based Detectors ……………………………….9
  - 1.3.4 Flat Panel Detectors ……………………………………………10
  - 1.3.5 Direct Conversion Flat Panel Detectors ……………………… 16

- 1.4 Detector properties …………………………………………………… 19
- 1.5 Background Theory ……………………………………………………21
- 1.6 Research Objectives …………………………………………………...24
- 1.7 Thesis Layout ……………………………………………………….25

2 X-ray Photoconductors 27
- 2.1 Properties of X-ray Photoconductor ………………………………….. 27
- 2.2 Potential Candidates ………………………………………………….. 31
  - 2.2.1 Amorphous Selenium (a-Se) …………………………………..31
  - 2.2.2 Mercuric Iodide (HgI_2) ………………………………………..33
  - 2.2.3 Lead Iodide (PbI_2) ……………………………………………..34
  - 2.2.4 Cadmium Zinc Telluride (CdZnTe) …………………………...35
  - 2.2.5 Lead Oxide (PbO) ……………………………………………..36
  - 2.2.6 Summary of Potential Candidates ……………………………..37

3 **Sensitivity** 40
3.1 X-ray Sensitivity ……………………………………………………40
3.1.1 X-ray Absorption and Quantum Efficiency …………………...41
3.1.2 EHP Generation and Ionization Energy ($W_{\pm}$) …………………45
3.1.3 Normalized Sensitivity ……………………………………….. 50
3.2 Induced Current and Collected Charge ……………………………… 52
3.3 Drift Mobility and Deep Trapping Time ………………………………53

4 **Monte Carlo Modeling** 58
4.1 Random Number Generation ………………………………………….58
4.2 Initial Position of Generated EHPs ……………………………………60
4.2.1 Uniform Electric field ………………………………………….61
4.2.2 Non uniform Electric field ……………………………………..63
4.3 Trap Limited Model …………………………………………………….. 63
4.4 Recombination between Drifting Carriers …………………………….66
4.5 Recombination between Drifting and Trapped Carriers ………………68
4.6 Trap Filling Effects ……………………………………………………..72
4.7 Nonuniform Electric Field Effects ……………………………………..73
4.8 X-ray Induced Effects …………………………………………………..75
4.9 Detrapping of Trapped Carrier ……………………………………….. 76

5 **Results and Discussion** 78
5.1 Results for Trap Limited Model ……………………………………….78
5.2 Results for Bimolecular Recombination……………………………….85
5.3 Results for Ghosting ……………………………………………………..88
5.3.1 Effect of Recombination ……………………………………….88
5.3.2 Trap Filling Effects ……………………………………………..94
5.3.3 Nonuniform Electric Field Effects …………………………....98
5.3.4 Effects of X-ray induced Trap Generation …………………...107
5.3.5 Effects of Trapped hole Detrapping ………………………….111
5.4 Comparison with Experimental Data ……………………………….. 113
5.5 Modification of Recombination Coefficient …………………………115

6 **Conclusions and Recommendations** 124
6.1 Summary ……………………………………………………………...124
6.2 Suggestions for Future Work ………………………………………...126

7 **References** ……………………………………………………………...128

8 **Appendix A** Random Number Generators…………………………133

9 **Appendix B** Defects in a-Se…………..…………………………136

LIST OF FIGURES

Figure 1.1 A typical radiographic x-ray imaging technique ………………………. 3

Figure 1.2 Schematic diagram of differential attenuation of x-rays in human body..3

Figure 1.3 Schematic illustration of a digital radiography system …………………6

Figure 1.4 Light spread in a thin (a) and thick (b) phosphor screen………………...7

Figure 1.5 Methods to couple a phosphor to a photodetector: (a) lens, (b) fibre optic………………………………………………………………...8

Figure 1.6 (a) Schematic illustration of a flat panel X-ray image detector; (b) X-ray image taken using traditional film technology (left) and using flat panel detector (right)……………………………………………………….11

Figure 1.7 Schematic illustrations of the two kinds of flat panel x-ray image detectors: (a) indirect conversion (b) direct conversion…..……………13

Figure 1.8 Thin film transistor (TFT) active matrix array (AMA) used in flat panel x-ray image detectors……………………………………………15

Figure 1.9 Amorphous Selenium based FPD with an active area of 43 cm × 43 cm for general radiography………………………………..……………17

Figure 1.10 Cross sectional structure of a flat panel active matrix direct conversion x-ray image detector (two pixels) ……………………………………. 18

Figure 1.11 Schematic illustration of ghosting in x-ray photoconductors…………..22

Figure 1.12 Schematic diagram of possible electron hole recombination process in a-Se...…..23

Figure 3.1 Schematic illustration of the photoconductor sandwiched between two parallel plate electrodes………………………………………………...41

Figure 3.2 Schematic illustration of attenuation of x-ray photons in a medium..…42

Figure 3.3 Schematic representation of x-ray attenuation, energy absorption and carrier generation……………………………………………………44

Figure 3.4 EHP creation energy vs energy bandgap E_g for various materials [8]…46

Figure 3.5 EHP creation energy of a-Se as a function of electric field for various x-ray photon energies [34]……………………………………………. 47

Figure 3.6 Comparison of the ionization energy, $W_\pm$ between the experimental data and the calculated values using the relation as given by equation 3.13. The experimental data has been extracted from figure 5 of Ref. 34…...49

Figure 3.7 Schematic illustrations of carriers drift and current in a positively biased x-ray photoconductor. ………………………………………………….53

Figure 3.8 Schematic illustration of shallow and deep traps for electrons in amorphous semiconductors...……………………............................54
Figure 3.9 Carrier trapping and release in amorphous semiconductors …………..55
Figure 3.10 A simplified diagram of DOS in amorphous selenium……………….. 56
Figure 4.1 A histogram of generated random numbers as discussed in section 4.1.59
Figure 4.1 Schematic illustration of probability density function calculation……. 60
Figure 4.2 Sensitivity calculations with different values of *N*……………………..61
Figure 4.3 Schematic illustrations showing the calculation of the probability density function…………………………………………………………62
Figure 4.4 Graphical interpretations showing the calculation of the initial position of the generated carriers………………………………………………..62
Figure 4.5 Current as a function of time in the x-ray photoconductor…………….64
Figure 4.6 Schematic illustration showing the initial position, x_i and final position, x_f for one time step Δt in a positively biased detector………………….65
Figure 4.7 Schematic illustration showing positions x_1 and x_2 for bimolecular recombination within time interval Δt…………………………………67
Figure 4.8 Schematic illustration showing positions x_1 and x_2 for carrier trapping and recombination within time interval Δt in a positively biased detector……………………………………………………………69
Figure 4.9 Block diagram representation determining carrier trapping and recombination…………………………………………………………..71
Figure 4.10 Schematic illustration of trap filling effect……………………………..73
Figure 5.1 The normalized sensitivity of mammographic detectors as a function of photoconductor thickness. (a) Positively biased detectors and (b) negatively biased detectors……………………………………………..80
Figure 5.2 The normalized sensitivity of chest radiographic detectors as a function of photoconductor thickness for both positive and negative biasing…..81
Figure 5.3 The normalized sensitivity versus mobility lifetime product for both positive and negative biasing. Mobility lifetime product of electrons (a) and holes (b)………………………………………………………83
Figure 5.4 The charge collection efficiency of mammographic detectors as a function of exposure rate. Bimolecular recombination is considered only……………………………………………………………………..85
Figure 5.5 The charge collection efficiency as a function of total carrier generation rate for mammographic and chest radiographic detectors……………...87
Figure 5.6 The charge collection efficiency as a function of total carrier generation rate for different electric fields………………………………………87
Figure 5.7 The normalized sensitivity versus cumulative x-ray exposure for mammographic applications. (a) Positively biased detectors and (b) negatively biased detectors……………………………………………..89
Figure 5.8 The normalized sensitivity versus cumulative x-ray exposure for chest radiographic applications. (a) Positively biased detectors and (b) negatively biased detectors……………………………………………..90
Figure 5.9 The relative sensitivity versus cumulative x-ray exposure for mammographic applications. (a) Positively biased detectors and (b) negatively biased detectors……………………………………………..92

Figure 5.10 The relative sensitivity versus cumulative x-ray exposure for chest radiographic applications. (a) Positively biased detectors and (b) negatively biased detectors……………………………………………..93
Figure 5.11 Trapped carrier concentrations inside the photoconductor after one R exposure for mammographic applications. (a) Positively biased detectors and (b) negatively biased detectors……………………………………95
Figure 5.12 Trap filling effects on the relative sensitivity for mammographic applications. (a) Positively biased detectors and (b) negatively biased detectors…………………………………………………………..97
Figure 5.13 Nonuniform electric field effects on the relative sensitivity for mammographic applications. (a) Positively biased detectors and (b) negatively biased detectors……………………………………………..99
Figure 5.14 Nonuniform electric field effects on the relative sensitivity for chest radiographic applications. (a) Positively biased detectors and (b) negatively biased detectors……………………………………………100
Figure 5.15 The normalized electric field versus normalized distance from radiation receiving electrodes after different x-ray exposures for mammographic applications. (a) Positively biased detectors and (b) negatively biased detectors…………………………………………………………102
Figure 5.16 The normalized electric field versus normalized distance from radiation receiving electrodes after different x-ray exposures for chest radiographic applications. (a) Positively biased detectors and (b) negatively biased detectors……………………………………………103
Figure 5.17 Charge collection efficiency (CCE), photogeneration ratio (PGR), and relative sensitivity versus cumulative x-ray exposure for mammographic applications. (a) Positively biased detectors and (b) negatively biased detectors…………………………………………………………104
Figure 5.18 Charge collection efficiency (CCE), photogeneration ratio (PGR), and relative sensitivity versus cumulative x-ray exposure for chest radiographic applications. (a) Positively biased detectors and (b) negatively biased detectors……………………………………………105
Figure 5.19 The relative sensitivity as a function of cumulative x-ray exposure for a positively biased mammographic detector……………………………107
Figure 5.20 Effects of the x-ray induced deep trap center generation on the relative sensitivity for mammographic applications. (a) Positively biased detectors and (b) negatively biased detectors…………………………108
Figure 5.21 Effects of the x-ray induced deep trap center generation on the relative sensitivity for chest radiographic applications. (a) Positively biased detectors and (b) negatively biased detectors…………………………109
Figure 5.22 Effect of trapped hole detrapping on the relative sensitivity mammographic applications. (a) Positively biased detectors and (b) negatively biased detector……………………………………………112
Figure 5.23 The relative sensitivity as a function of cumulative water equivalent dose. (a) Applied electric field is 2.9 V/μm and (b) applied electric field is 1.7 V/μm. The experimental data has been extracted from figure 7 of Ref. 17…………………………………………………………...114

Figure 5.24 The relative sensitivity as a function of cumulative water equivalent dose. The experimental data has been extracted from figure 7 of Ref. 17……………………………………………………………...116

Figure 5.25 The relative sensitivity versus cumulative exposure for a negative biased a-Se detector with different applied electric fields. The experimental data has been supplied by the Anrad Corporation…………………………117

Figure 5.26 The relative sensitivity versus cumulative exposure for a negative biased a-Se detector with different applied electric fields. The experimental data has been supplied by the Anrad Corporation…………………………118

Figure 5.27 The relative sensitivity versus cumulative exposure for a negatively biased a-Se detector with different applied electric fields, including an effective recombination coefficient. The experimental data has been supplied by the Anrad Corporation………………………………...119

Figure 5.28 The relative sensitivity versus cumulative exposure for a positively biased a-Se detector with different applied electric fields including an effective recombination coefficient. The experimental data has been supplied by the Anrad Corporation………………………………...121

Figure 5.29 The charge collection efficiency versus cumulative exposure for both positive and negative biasing conditions. The applied electric field is 3 V/µm……………………………………………………………..122

Figure 5.30 The photogeneration ratio versus cumulative exposure for both positive and negative biasing conditions. The applied electric field is 3 V/µm.122

Figure B.1 Structure and energy of simple bonding configuration for selenium atoms. Straight lines represent bonding orbitals, lobes represents lone-pair (nonbonding) orbitals, and circles represent antibonding orbitals. The energy of lone-pair is taken as the zero energy (Ref. 50)………..137

LIST OF TABLES

Table 1.1 Parameters for digital x-ray imaging systems. ……………………….. 15
Table 1.2 Flat panel detectors based on a-Se marketed by ANRAD Corporation..17
Table 2.1 Preparation methods and temperature for different photoconductors.....37
Table 2.2 Comparison of the physical properties of the candidates discussed above to be used as x-ray photoconductor…………………………………….38
Table 2.3 Comparison of the imaging properties of different photoconductors as discussed above……………………………………………………...39

LIST OF ABBREVIATIONS

A/D	analog to digital
a-Si:H	hydrogenated amorphous-silicon
a-Se	amorphous selenium
AMA	active matrix arrays
CCD	charge coupled device
CR	computed radiography
CB	conduction band
CCE	charge collection efficiency
DR	digital radiography
DQE	detective quantum efficiency
DOS	density of states
EHP	electron hole pair
ESR	electron spin resonance
FPD	flat panel detector
II	image intensifier
IFTOF	interrupted field time-of-flight
IVAP	intimate valence alternation pair
kV_p	kilo volt peak
keV	kilo electron volt
LSF	line spread function
LP	lone pair
MTF	modulation transfer function
PVD	physical vapour deposition

PIB	particle in binder
PGR	photo generation ratio
SNR	signal to noise ratio
TFT	thin film transistor
TOF	time-of-flight
VB	valence band
VAP	valence alternation pair

1. Introduction

Broadly, solid state materials can be classified into two categories: those which possess long-range-order in the distribution of their constituent atoms, and those which do not. The first type of material is known as a *crystal*, while the second one is termed as *amorphous***.**

Advancement of semiconductor devices based on crystalline materials has already reached maturity. The device physics of crystalline solids is easy to understand thereby the use of quantum mechanics due to the mathematical simplicities in dealing with long range translational order or periodic structures. In contrast, device science of amorphous materials did not experience the same explosion of growth as their crystalline counterparts did, predominantly due to the mathematical complexities inherent in dealing with non-periodic structures. However, amorphous materials were suspected to exhibit limited charge transport properties compared to crystalline solids which prevented their wide use in microelectronics. In the last two decades, however, amorphous semiconductors have found a number of applications in electronics.

Although, the modern electronics industry is dominated by crystalline materials, these materials fail to cover large-area applications for human needs; this has opened up a new area of research to fulfill this requirement. Amorphous semiconductors have been found to be easily coated over large areas in a cost effective way, which makes them available for large area applications. As our understanding of the physics of amorphous semiconductors evolved, numerous new applications have begun to emerge which showed that theses materials could be used for a variety of applications. Amorphous semiconductors possess a greater diversity of physical properties and their preparation does not require the carefully controlled growth as their crystalline opponents do. These lead to the prediction that amorphous semiconductors will dominate in the next era of the microelectronics industry [1].

Amorphous semiconductors have already established themselves in several commercial applications. Before 1990's, the three major applications for large area electronics were xerography, thin film transistors, and solar cells. But in the last decade, there have been a number of new applications, such as detectors in image sensors and photoconductors in x-ray image detectors.

1.1 X-ray Imaging

X-ray imaging is one of the fastest and easiest ways for a physician to view the internal organs and structures of the human body. X-rays, discovered by Roentgen more than 100 years ago, may be the most important scientific discovery with the fastest implementation into practice. Within six months of its discovery, x-rays were being applied for the purposes of medical imaging and diagnostics, and led to the development of a new branch of medical sciences known as diagnostic radiology. Diagnostic radiology is the art and science of image acquisition using x-ray radiation. The radiographer applies x-ray radiation as the information carrier to the patient to produce diagnostic images of the human body, commonly known as *X-ray pictures*.

Although diagnostic radiology was developed over 100 years ago, there is still much on-going research in this important imaging technology. One active area of research is the acquisition of x-ray images. Figure 1.1 shows a typical imaging technique, in which an object is placed between the x-ray sensitive image receptor (detector) and the x-ray source. The x-ray sensitive receptor captures the image of the internal structure of the object from the x-rays.

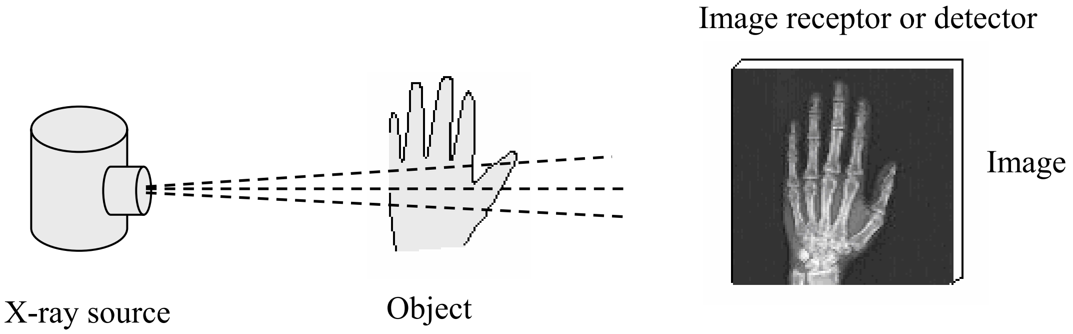

Figure 1.1 A typical radiographic x-ray imaging technique.

The attenuation of x-rays is different in different parts of the human body (bone, soft tissue or other kinds of human organs). Radiographic imaging systems rely on this differential attenuation of x-rays passing through the human body. When x-rays, of uniform intensity, impinge upon the human body, the x-rays undergo differential attenuation. Thus, the intensity of the radiation is modulated by this differential absorption, as shown in figure 1.2.

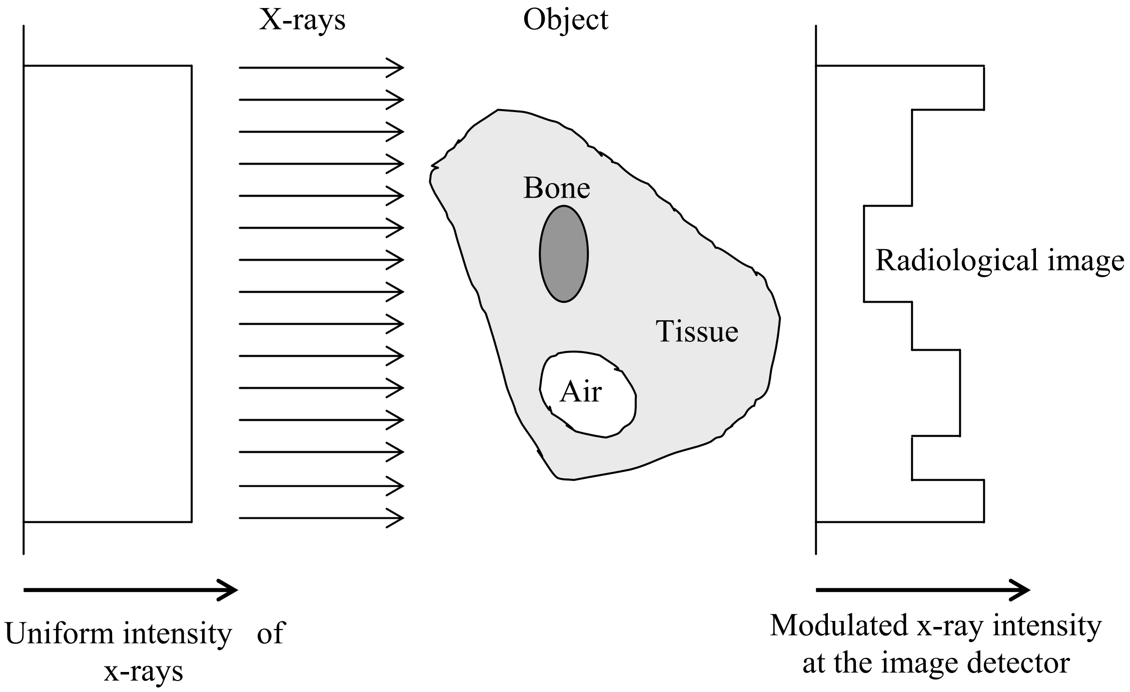

Figure 1.2 Schematic diagram of differential attenuation of x-rays in human body.

The modulated radiation intensity is known as the *remnant radiation*. So, the remnant radiation that exits the body contains the information about the internal structure of the body. If remnant radiation is detected, we can then obtain the image of the human body. The medium or device that transforms the remnant x-ray flux into a visible image is called the *image receptor or image detector*.

Like other forms of ionizing radiation, x-rays can cause damage to living tissues; which is known as biological damage. In order to minimize this biological damage, exposure of the human body to x-rays must be minimized. Several techniques have been developed in order to obtain high quality images with minimum exposure. All of these techniques are largely based on the proper design of the image receptor (according to Fig 1.1).

1.2 Film based Radiography

Film was the first image receptor chosen by Roentgen and it still remains the most popular and widely used technique for radiographic images. Although several computer based digital imaging systems have been developed, about 65% to 70% of medical imaging system is film based analog technology. Film has an extremely high spatial and temporal resolution and film based imaging is cheap and permanent. Traditional film based image receptors consist of a photographic film sandwiched between two fluorescent screens and mounted in a protective cassette [2]. The fluorescent screens convert the x-ray energy into visible light which is recorded in the photographic film to form a *latent image*. The latent image is the invisible change induced in the photographic film. With proper chemical processing, the final image is obtained. Thus, the process involves the following steps:

1. The cassette is first loaded with film
2. The loaded cassette is taken to the examination room, then to the x-ray equipment

3. After x-ray exposure, the cassette is taken to darkroom for development and the processed film is checked to ensure that there is no problem and that the film is suitable for making a medical diagnosis.

This laborious process takes several minutes, which is considered to be too long for emergency imaging, and over this time the x-ray room is locked. Although film based technology offers good image quality, this technology suffers from the following disadvantages:

1. Only about 3-5% of the x-ray radiation is converted into a visible image.
2. The delay between exposure and obtaining the final image is long.
3. The image is not electronically captured.
4. Real time imaging is impossible.
5. Image processing is not possible without digitizing the image on the film.
6. Noise cannot be easily minimized.
7. Archiving and post processing represents a challenge.

1.3 Digital Radiography

Digital radiography (DR) overcomes nearly all of the disadvantages inherent film based traditional radiography. It provides image viewing immediately after the patient's x-ray exposure, a high quality radiograph on a video monitor with reduced x-ray dose, less handling, more convenient patient management, computer aided diagnosis and image processing, ease of storage on a computer disk rather than in archaic film stacks, electronic transportation of the image, and finally high quality real time imaging. A schematic diagram of a digital radiography system is shown in figure 1.3.

Here, the image receptor (according to figure 1.1) is replaced by an x-ray image detector that converts the x-rays into an electronic signal which is then digitized by an analog to digital (A/D) converter and recorded on a computer memory. The image can then be processed, displayed, transmitted or archived using a computer.

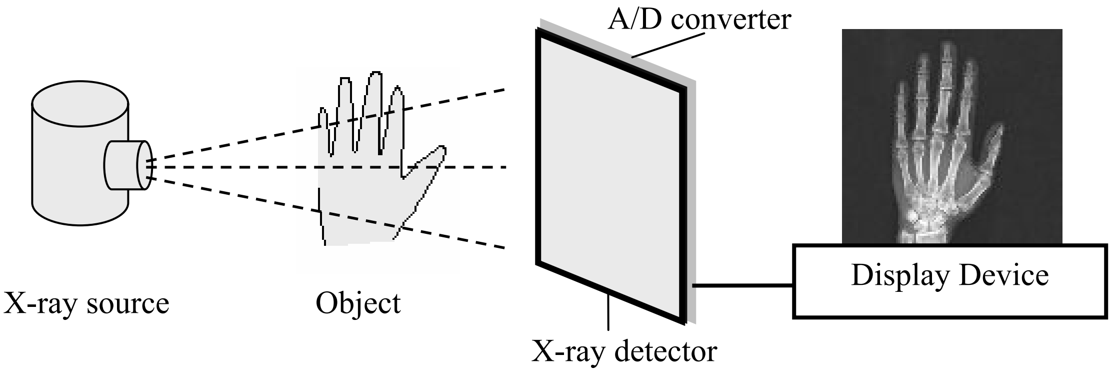

Figure 1.3 Schematic illustration of a digital radiography system.

In digital imaging systems, the captured x-ray image must be sampled both in the spatial and intensity dimensions (performed by an array of x-ray detectors). In spatial dimensions, samples are obtained as averages of the intensity over picture elements known as *pixels*. Pixels are usually square and spaced at equal intervals throughout the plane of the image. In the intensity dimensions, the signal is digitized into *bits*. For a digital system, image quality is determined by the pixel size and bit-depth. To avoid degradation of the image quality, pixel size and bit depth are engineered to be optimal for a particular application. Several techniques for digital radiography have been described. Only a brief review of some suitable techniques is presented here [3, 4].

1.3.1 Phosphor based Detectors

Most digital imaging systems are cesium iodide (CsI) phosphor based detectors and involve indirect conversion from x-ray photons to a detectable electrical signal. A phosphor absorbs the x-ray radiation and converts it to light, which is then coupled to an optical sensor. The latter may be a *charge coupled device* (CCD). One of the main disadvantages of converting the x-ray radiation into light is that when light passes through a phosphor, it is dispersed. The amount of dispersion is proportional to the path length required to escape the phosphor, as shown in figures 1.4 (a) and (b).

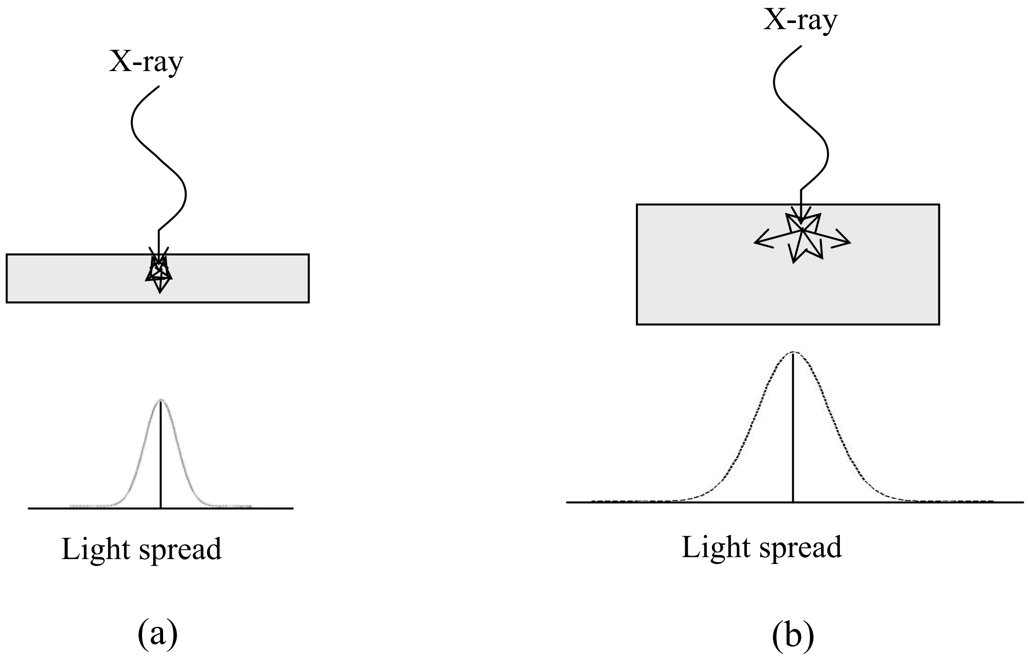

Figure 1.4 Light spread in a thin (a) and thick (b) phosphor screen.

Light dispersion deteriorates the spatial resolution. If the phosphor layer is made thin to enhance the spatial resolution, the conversion from x-rays to light (which is known as quantum efficiency) will decrease. This means that compromises must be made between the spatial resolution and the quantum efficiency. Further losses occur in the coupling of the light to the CCD. Another disadvantage lies in the CCD readout device. An x-ray detector for general medical applications needs to be relatively large (maximum is 35 cm × 43 cm for chest radiology), but CCDs can only be made for relatively small areas (~4 to 16 cm^2) and thus cannot be used directly as large area x-ray detectors. The output from the phosphor must be demagnified to the dimensions of the CCD using either an expensive lens system or tapered fiber optic bundles, as shown in figure 1.5. This minification leads to poor optical coupling and introduces additional noise called *secondary quantum noise*.

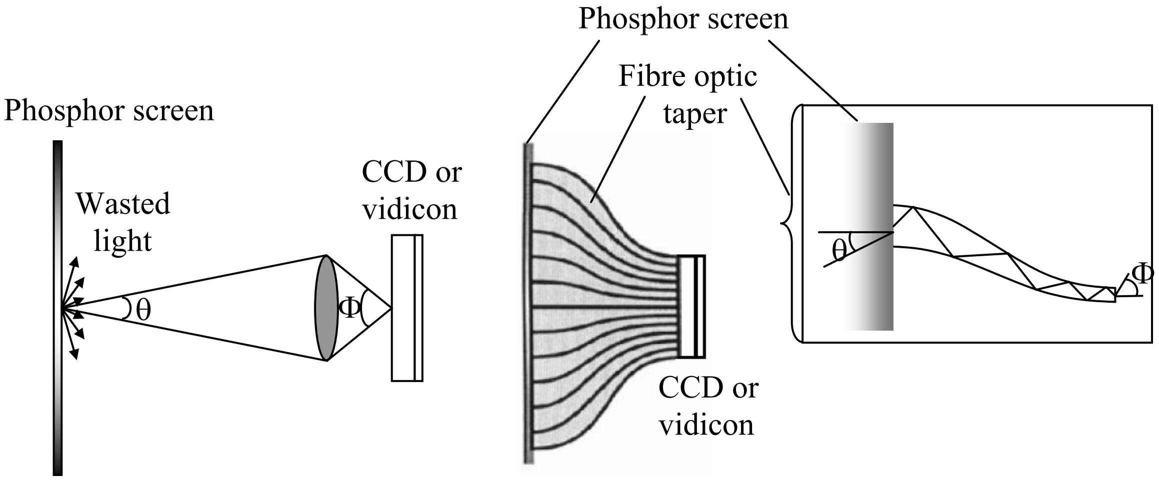

(a) Optical lens coupling (b) Fibre optic coupling

Figure 1.5 Methods to couple a phosphor to a photodetector: (a) lens, (b) fibre optic.

1.3.2 Photostimulable Phosphor based Detectors

Photostimulable phosphor (also known as a storage phosphor) based detectors are very popular in DR to date. These phosphors are commonly in the barium fluorohalide family, typically BaFBr:Eu. This system also relies on indirect conversion and can store a latent image. X-ray absorption mechanisms are identical to those of a conventional phosphor but differ in that the useful optical signal is not derived from the light emitted in prompt response to the incident radiation, as in conventional film/screen systems, rather from subsequent stimulated emission when electrons and holes are released from traps of the materials. The initial x-ray interaction with the phosphor crystal causes electrons to be excited. Some of these electrons produce light in phosphor in the normal manner but this is not used. Instead, the phosphor is intentionally designed to contain electron traps that store a latent image as a spatial distribution of trapped charges. By stimulating the phosphors through irradiation with a suitable light, the electrons are released from the traps and raised to the conduction band. This subsequently triggers the emission of a shorter wavelength light. This process is called photostimulated luminescence. The digital imaging system based on this mechanism is commonly called computed radiography (CR). In CR systems, the imaging plate (a screen made using photostimulabe phosphor) is positioned in a light tight cassette or enclosure, exposed, and then readout by raster scanning the plate with a laser to release the luminescence. The emitted light is then collected and detected with a photomultiplier tube, whose output signal is digitized to form the image. The plate is then flooded with light to erase any residual image left in the plate and is then ready to reuse. The photostimulabe phosphor is an excellent detector for DR in that, when placed in a cassette, it can be used with a conventional x-ray machine. They have linear response over a wide range of x-ray intensities; the plates are reusable and large area plates can be conveniently produced, which is essential in medical imaging. This system is similar to film based radiography, and so requires the carrying of the cassette from a loading/unloading station to the patient examination room and back. Moreover, photostimulabe phosphors are not as efficient as conventional film based detectors and the resolution is not as good as in film based technology.

1.3.3 Image Intensifier based Detectors

Image intensifier based fluoroscopy has been used for real time image visualization and interaction. The resulting real time images are usually displayed using a video system (conventional or CCD) optically coupled to the x-ray image intensifier. The emergent x-rays from the object are made incident on the input screen of the image intensifier (II) tube. The II tube is a complex electronic device with an x-ray sensitive phosphor as the input screen, a photocathode, a set of electro-optics incorporating accelerating potentials, and an output phosphor for a small bright image. The input phosphor screen converts the x-rays into visible light which is then converted into electrons efficiently through the photocathode. The greatest efficiency is obtained when the spectral sensitivity of the photocathode is matched to the phosphor spectrum. The electrons are accelerated through a large potential difference and electrostatically focused by the electrodes onto a small output phosphor. The output phosphor converts incident electrons into visible light. This II tube is coupled to a video camera, recorder, and monitor. Thus, the II tube converts the emergent x-rays into visible light of high intensity; the camera converts light into an electrical signal; a monitor reproduces the image and a recorder is used to take a *spot film* for further study. Digital imaging systems based on II based detectors have several disadvantages: the bulky nature of the intensifier tube impedes the clinician, limiting access to the patient and prevents the acquisition of some important radiographic views; loss of image contrast due to x-ray and light scattering within the tube; and the geometric distortion of the image largely due to the curved input phosphor.

1.3.4 Flat Panel Detectors

If a radiologist were to speculate about the ideal x-ray imaging system, he would imagine a digital flat panel detector (FPD) that can perform all current radiological modalities – radiography, fluoroscopy, and mammography at reduced x-ray doses. It would provide the image just after the patient's x-ray exposure, a high quality image on a video monitor, and would also be usable for real time imaging with a large image detection area. Existing imaging systems can be easily adapted to flat panel image detectors, the x-ray image can be directly recorded on a computer, rapidly displayed and image processing techniques can be applied to analyze the image. It is believed that all the requirements for ideal imaging can be fulfilled through the use of flat panel detectors.

The key factor for DR is the large area readout device that is required because x-rays cannot readily be focused. Recent research has identified that large area thin film transistor (TFT) active matrix array (AMA) can be used as a readout technique. This approach permits essentially instantaneous readout and higher quality imaging. The development of AMA matured as the fabrication and doping of large area hydrogenated amorphous-silicon (a-Si:H) films became technologically possible in the early 1990s [5]. This development was primarily directed to displays used in various consumer applications. But soon it facilitated the development of a new class of medical imaging device that solves many of the limitations inherent in the methods of acquiring an instantaneous large area x-ray image. Coupling the traditional x-ray detectors, such as phosphors or photoconductors, with the AMA solves the large area readout problem. The flat panel x-ray imaging concept is illustrated in figure1.6.

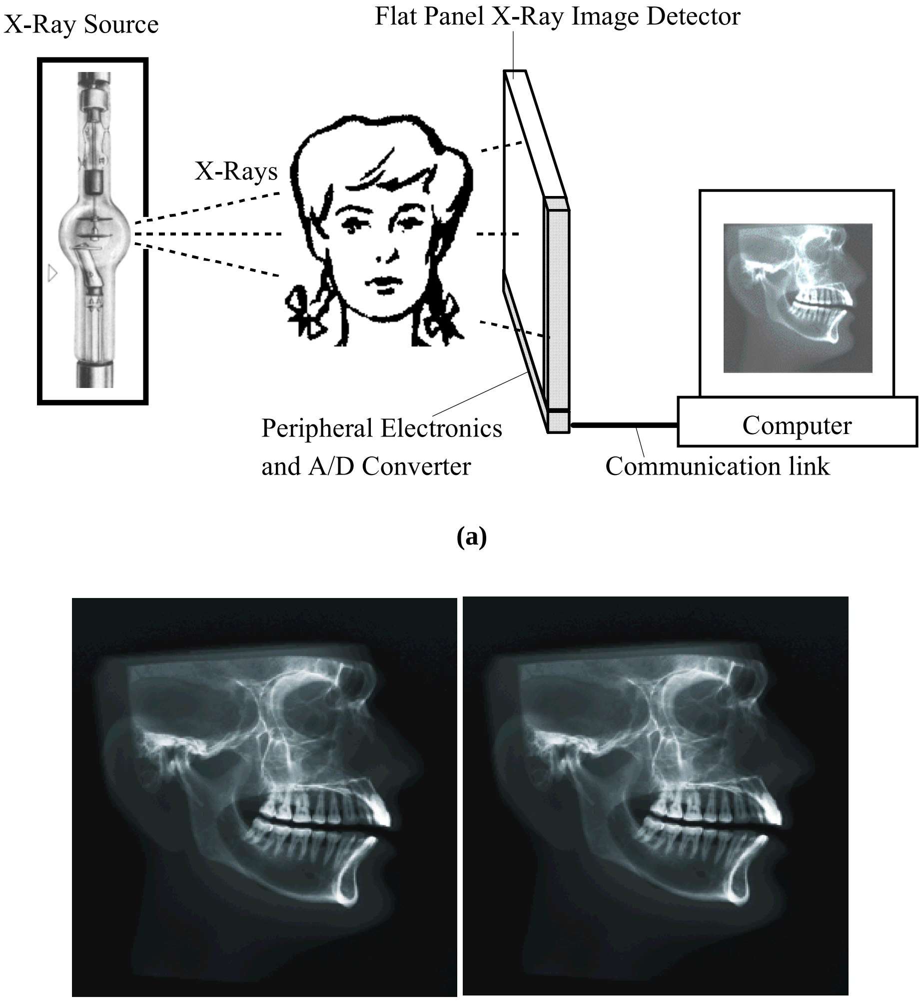

(a)

(b)

Figure 1.6 (a) Schematic illustration of a flat panel X-ray image detector; (b) X-ray image taken using traditional film technology (left) and using flat panel detector (right).

In flat panel systems, x-rays passing from an object are incident on a large area flat panel sensor. The flat panel sensor consists of millions of pixels, each of which acts as an individual detector. Each pixel converts the radiation that it receives into a measurable amount of signal that is proportional to the amount of the radiation it has received. The signal is then stored and readout by scanning the arrays. So the formation of the x-ray image through the use of a flat panel AMA is carried out in three steps. In the first step, x-rays interact with a suitable detection medium (detector) to generate a measurable response, such as a quantity of charge (ΔQ). The second step is the storage of the response (charge ΔQ) with a recording device, and the final step is the measurement of the stored response and its digitization for computer acquisition and display. Two types of x-ray detection processes, *direct* and *indirect* conversion, are currently used for flat panel image detectors, and are shown in figures 1.7 (a) and (b).

In the indirect detection approach [6, 7], a phosphor layer is used with the AMA to convert the x-ray radiation into visible light. The intensity of the light emitted from a particular location of the phosphor is a measure of the intensity of the x-ray beam incident on the surface of the detector at that point or pixel. Each pixel on the AMA has a photosensitive layer or a pin photodiode to convert that light signal into an electrical signal. The electrical signal or charge is stored until the AMA is readout. The magnitude of the electrical signal from the different pixels contains the imaging information inherent in the intensity variations of the x-ray beam. The conversion process involves x-ray → photons (visible light) → electrical signal. So the indirect approach involves an intermediate conversion step from x-ray radiation to light.

In the direct conversion approach [3, 4]**,** the x-ray detection process is performed with the help of a thick layer of photoconductor material. At first, a thick layer of photoconductor material is coated over the AMA. On the top of the photoconductor layer, an electrode is deposited for biasing, which creates an electric field across the photoconductor. The photoconductor material converts the absorbed radiation directly into electrical charges, which are then stored on the pixel-storage capacitor until the AMA is readout. The detection process is direct in that, the image information is transferred from x-rays directly into an electrical signal.

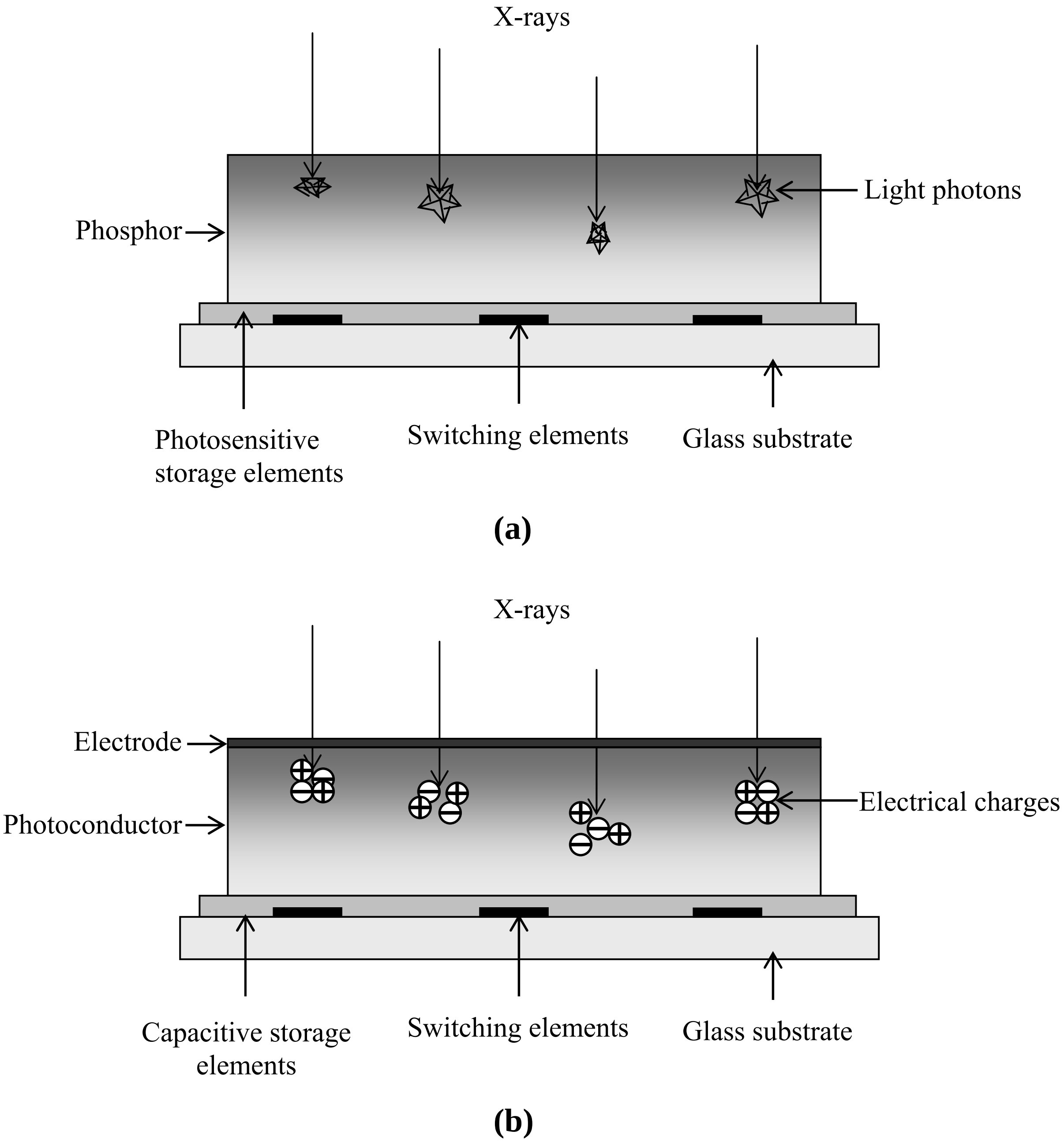

Figure 1.7 Schematic illustrations of the two kinds of flat panel x-ray image detectors: (a) indirect conversion (b) direct conversion.

The direct and indirect approaches are more meaningful in terms of the initial x-ray detection mechanism rather than the details of the flat panel array design. In both approaches, the latent image is a charge distribution residing on the panel's pixels. The charges are simply readout by scanning the arrays row by row using peripheral electronics and multiplexing the parallel columns into a serial digital signal. This signal is then transmitted to a computer system.

An AMA, as shown in figure1.8, consists of millions of pixel [5, 8]. Each pixel has its own storage capacitor and TFT switch. The pixels are connected to a set of row and column electrodes. In figure 1.8, gates in a given row are connected together to a single line electrode and TFT sources are connected to a single column line electrode. The TFT switches control the image charge so that one line of pixels is activated electronically at a time. Normally, all the TFT are off, permitting the latent image charge to accumulate on the array.

The readout is achieved through external electronics and software controlling the state of the TFT switches. Very large area AMAs are now available. The AMA consists of M × N numbers of TFT-based pixels and each pixel (i,j) has a charge collection electrode B connected to a signal storage capacitor C_{ij} whose charge can be read by properly addressing the TFT_{ij} via the gate line i and source line j. An external readout electronics and software, by proper self scanning, converts the charges read on each C_{ij} to a digital image. All TFTs in a row have their gate electrodes connected whereas all the TFTs in a column have their sources connected. When gate line i is activated, all TFTs in that row are now turned "on" and N data lines from $j = 1$ to N then read the charges on the pixel electrodes in the row i. The parallel data are then multiplexed into serial data, digitized, and then fed into a computer for imaging. The scanning control then activates the next row, $i+1$ and so on until the whole matrix has been readout from the first to the last row (M-th row). Different medical applications required different x-ray spectra. The size of the detector and pixel depends on the x-ray spectrum and hence on the type of medical application. The requirements for the x-ray spectrum and pixel sizes for different clinical tasks are shown in Table 1.1.

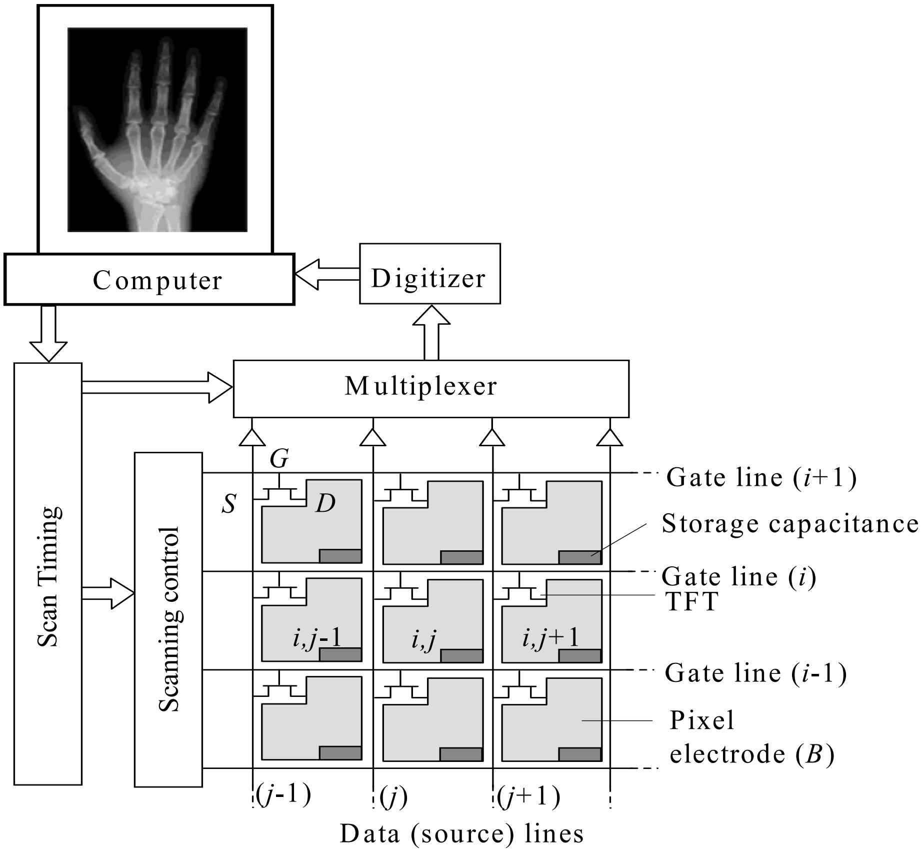

Figure 1.8 Thin film transistor (TFT) active matrix array (AMA) used in flat panel x-ray image detectors [8].

Table 1.1 Parameters for digital x-ray imaging systems (Data from Ref. 3).

Clinical task	Chest radiology	Mammography	Fluoroscopy
Detector size	35 cm × 43 cm	18 cm × 24 cm	25 cm × 25 cm
Pixel size	200 μm × 200 μm	50 μm × 50 μm	250 μm × 250 μm
Number of pixels	1750 × 2150	3600 × 4800	1000 × 1000
Readout time	~ 1 s	~ 1 s	~ 1/30 s
X-ray spectrum	120 kVp	30 kVp	70 kVp
Mean energy	60 keV	20 keV	40 keV

Research and development are on-going into both indirect and direct conversion flat panel detectors; however, the direct conversion method offers some advantages over its indirect counterpart. As discussed earlier, in the indirect conversion method x-rays absorbed in the phosphor screen release light which must escape to the surface to create an image, but while travelling through the phosphor light spreads and the amount of spreading is proportional to the path length of the phosphor. This spreading results in a loss of spatial resolution. Spreading of light can be reduced by using a structured phosphor, such as CsI, but still sufficient to deteriorate the resolution. Lateral spreading of information and hence the loss of resolution can also take place in photoconductor based direct conversion systems, but the inherent resolution of the photoconductor based direct conversion system is far superior to that of the indirect phosphor based system. The reported experimental resolution of an amorphous selenium (a-Se) based detector is much better than that of the phosphor based detector [9]. Other advantages associated with the direct conversion approach are the absence of optical coupling, hence the absence of noise associated with the optical coupling, and the ease of integrating the photoconductor with the AMA.

1.3.5 Direct Conversion Flat Panel Detectors

Stabilized a-Se (a-Se alloyed with 0.2-0.5% As and doped with 10-40 ppm Cl) photoconductor based flat panel detectors have been shown to be excellent x-ray imagers [8]. The requirements of a photoconductor for use in flat panel detectors will be discussed in chapter 2. The direct conversion flat panel detector is now a very attractive technology due to its compact detector size, fast image readout, high resolution and extremely low noise. This technology has been recently commercialized through several Corporations in the USA (Direct Radiography Corporation), Canada (Anrad Corporation), and Japan (Toshiba Corporation). Table 1.2 shows the a-Se based FPDs marketed by Anrad Corporation, Canada for mammography, general radiography, and real time or fluoroscopic applications [10]. The performances of these detectors have been presented in several papers [11-16]. It has been shown that they have very good resolution, fast image acquisition and readout, and extremely low noise. Figure 1.9 shows a 43 cm × 43 cm FPD for general radiography marketed by Anrad Corporation, Canada.

Table 1.2 Flat panel detectors based on a-Se marketed by ANRAD Corporation.

PFD	Size and application
SMAM	17 cm × 24 cm flat-panel for digital mammography
LMAM	24 cm × 30 cm flat-panel for digital mammography
GR17	43 cm × 43 cm flat-panel for general radiography
FPD9	23 cm × 23 cm flat-panel for real-time applications
FPD14	35 cm × 35 cm flat-panel for real-time applications

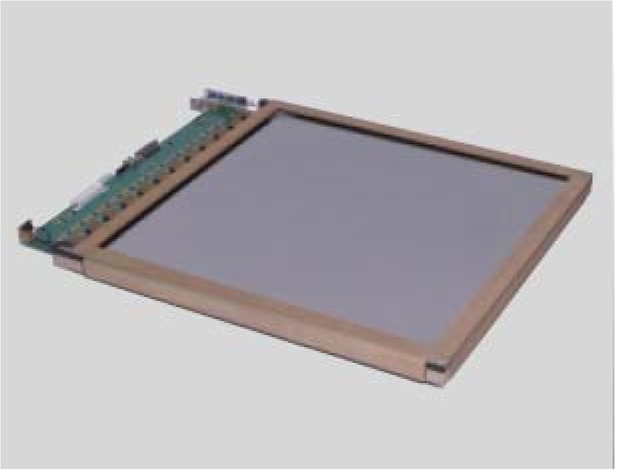

Figure 1.9 Amorphous Selenium based FPD with an active area of 43 cm × 43 cm for general radiography (Courtesy of Anrad Corporation).

A simplified cross sectional diagram of a direct conversion flat panel x-ray image detector is shown in figure 1.10 [8]. Stabilized a-Se layer is coated onto the AMA to serve as an x-ray photoconductor. In order to apply a biasing potential, a metal electrode, A, is deposited onto the a-Se layer. This bias potential creates an electric field inside the photoconductor. The electrode on the other side is pixelated which is B as shown in figure 1.10. The applied bias voltage to the radiation receiving electrode A may be positive or negative depending on the charge transport properties of the photoconductor. The applied bias is such that the electric field is 10 V/μm (standard) for an a-Se photoconductor. When incident x-ray photons are absorbed by the photoconductor, electron hole pairs (EHPs) are generated in the photoconductor. Electrons and holes move towards their respective electrodes under the action of the applied electric field. With a positive bias on electrode A, electrons are collected by the positive bias electrode A and holes are collected by the pixelated electrode B. Collected carriers provide a charge signal ΔQ_{ij} on the pixel storage capacitor C_{ij}. This charge signal is readout during self scanning. So, each pixel electrode carries an amount of charge ΔQ_{ij} that is proportional to the amount of incident x-ray radiation over the pixel area. All of the charges stored on the pixel electrode capacitors form the latent image.

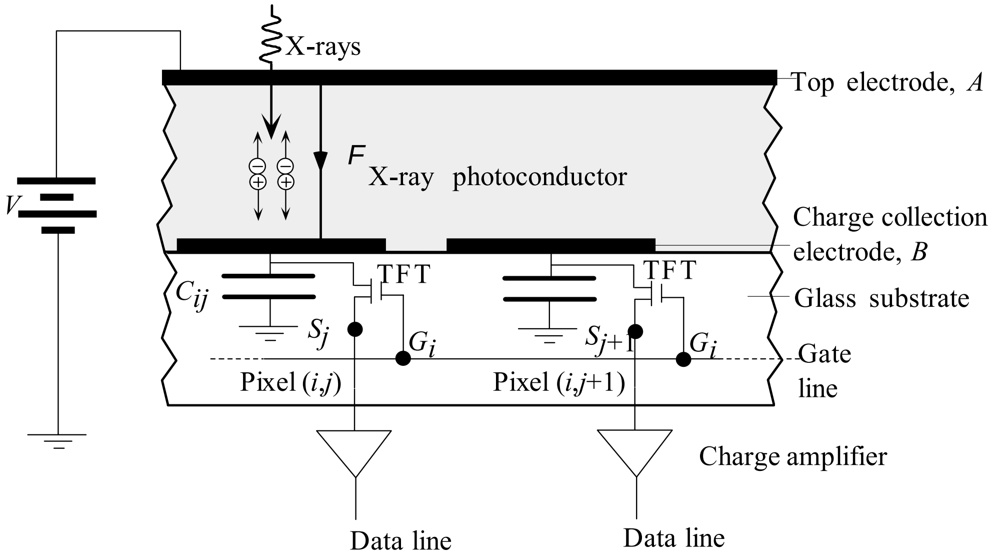

Figure 1.10 Cross sectional structure of a flat panel active matrix direct conversion x-ray image detector (two pixels).

To readout the latent image charge at a pixel, the appropriate TFT is turned on at every Δt seconds and the charge signal is transferred to the data line via a charge amplifier.

These signals are then multiplexed into serial data, digitized, and sent to a computer for imaging.

1.4 Detector properties

There are some important properties that all detectors should meet in order to provide improved performance. These properties are field coverage, quantum efficiency, sensitivity, spatial resolution, noise characteristics, homogeneity, uniformity, acquisition speed, frame rate, and cost. Different detectors technologies necessitate compromises among these factors.

The imaging system must be able to record the transmitted x-ray signals over the projected area of the object under investigation. The size of the detector for different medical applications was given in table 1.1. Uniformity and linearity are important requirements for the detector. Uniformity means that the response of a detector to x-rays should be same over the entire area of the detector. This means that the sensitivity of each pixel should be same. Linearity of a detector means that the output signal increases linearly with the amount of input x-ray radiation.

The initial image acquisition operation is identical in all x-ray detectors. In order to produce a signal, the x-ray quanta must interact with the detector material. The fraction of the x-ray photons that interact with the photoconductor, referred to as the quantum efficiency, and is denoted by η. For improved imaging, the quantum efficiency of a detector should be high. For the ideal case, the quantum efficiency is unity.

The final output from an x-ray detector is an electrical signal. The sensitivity is defined as the collected charge or output electrical signal per unit x-ray radiation per unit area. The sensitivity of any imaging system depends on the quantum efficiency and on the primary conversion efficiency (i.e. the EHP pair creation energy). For all detectors, the output electrical signal or the sensitivity should be maximized to maintain a signal size larger than the system noise.

Spatial resolution in radiography is determined both by the detector characteristics and by factors unrelated to photoconductors. The latter category includes unsharpness arising from geometrical factors such as penumbra due to the effective size of the x-ray source and relative motion between the x-ray source, patient and photoconductor during the exposure. Detector-related factors arising from its effective aperture size, spatial sampling interval between measurements and any lateral signal spreading effects within the detector readout. The spatial resolution of an imaging device or system is described in terms of *Modulation Transfer Function* (MTF). When x-rays are incident on a particular pixel, signals are induced not only on that pixel but also on the side pixels. The induced signal on the pixel that receives the radiation is the actual signal and the induced signals on the side pixel reduce the resolution of the system. MTF is the Fourier transform of the *Line Spread Function* (LSF). When x-rays are incident along a line of pixels, the LSF is defined by the ratio of the collected charges of the line pixels that receive the radiation to the collected charges of lateral pixels.

All images generated through x-ray quanta are statistical in nature. Although the image pattern can be predicted by the attenuation properties of the patient, it will fluctuate randomly about the mean predicted value. A useful quantity for characterizing the overall signal and noise performances of imaging detectors is their spatial frequency-dependent *detective quantum efficiency*, DQE(f). Detective quantum efficiency is defined as the ratio of the squared output signal to noise ratio (SNR) to squared input signal to noise ratio. Ideally DQE(f) is equal to quantum efficiency for all f, but additional noise sources reduce this value and often cause the DQE to decrease with increasing spatial frequency.

1.5 Background Theory

Much interest has been devoted to direct conversion flat panel x-ray detectors in the last decade. As discussed earlier, direct conversion flat panel x-ray imager provides better imaging than other sorts of imaging techniques. The performance of direct conversion flat panel x-ray imagers critically depends on the choice of the x-ray photoconductor material. The type of material to be used as an x-ray photoconductor in direct conversion flat panel x-ray detector has been a subject of enormous research. So, modeling of the x-ray photoconductors for direct conversion flat panel detector is an important research topic.

Several parameters determine the performance of a photoconductor as described in section 1.4. These parameters mainly are (i) Sensitivity, (ii) MTF, and (iii) DQE. Among these parameters, sensitivity is considered to be the most important metric in gauging the overall performances of a photoconductor. The x-ray sensitivity is defined as the collected charge per unit area per unit exposure of radiation.

"Although a-Se photoconductor based flat panel detectors have shown to be excellent x-ray imagers, however, recent experiments indicate that an x-ray photoconductor can suffer from *ghosting* [17, 18]". "Ghosting" refers to the change in the x-ray sensitivity of the detector in a subsequent exposure as a result of accumulated previous exposures. Normally ghosting causes the detector sensitivity to decrease. A shadow of the previous image is observed because the detector's sensitivity in each pixel has been decreased due to previous exposures. More realistic definition of ghosting is given in figures 1.11 (a) and (b). In the first exposure, a small rectangular area of the photoconductor is irradiated with x-rays and we obtain the sensitivity S as shown in figure 1.11 (a). In the subsequent exposure, a relatively larger area of the photoconductor is irradiated with uniform x-rays. Now the sensitivity of the previously irradiated portion (S′) is less than the sensitivity of the non-irradiated portion (S) as shown in figure 1.11 (b).

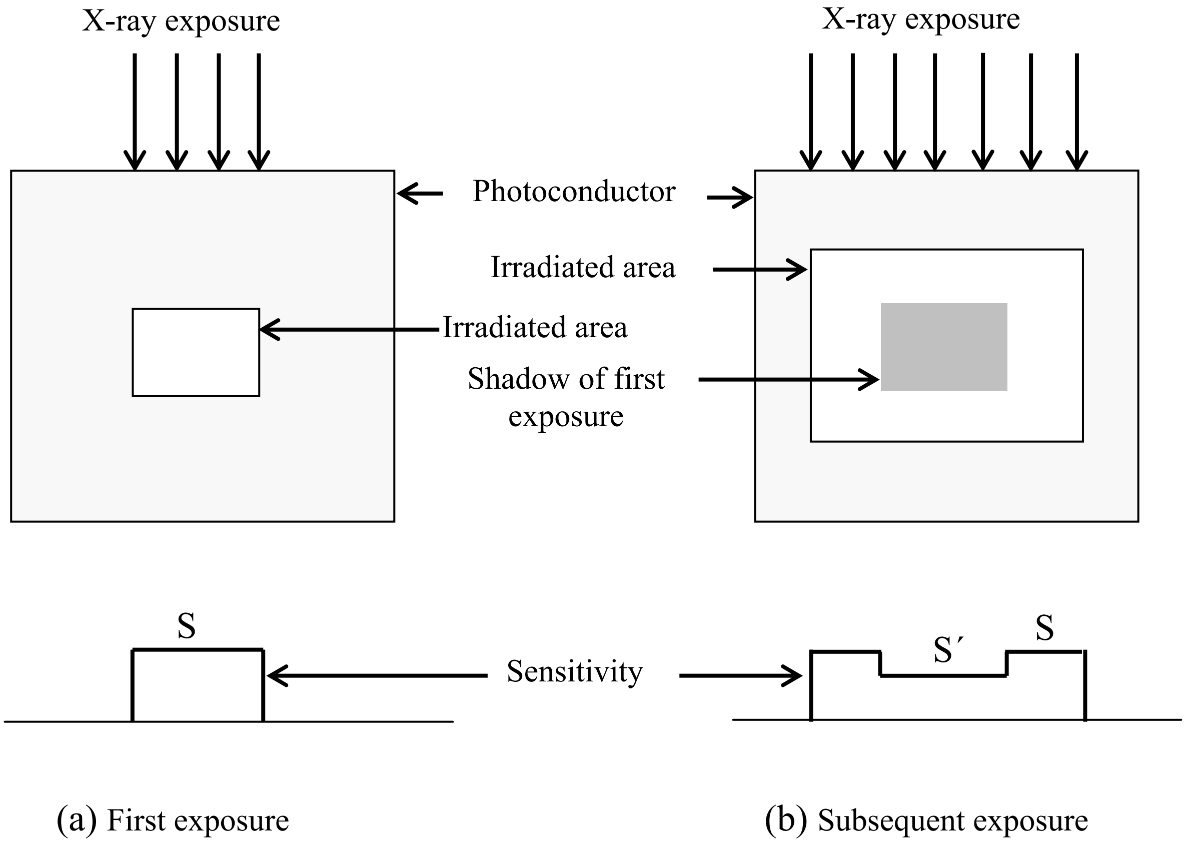

(a) First exposure (b) Subsequent exposure

Figure 1.11 Schematic illustration of ghosting in x-ray photoconductors.

The study of ghosting mechanism in photoconductor based flat panel x-ray image detectors is considered as a topical research area since the exact origins of ghosting have not been resolved. Although the amount of ghosting is not significant in the clinical dose range, the amount of ghosting is not trivial at higher doses.

The x-ray sensitivity of photoconductors that includes the effects of charge carrier trapping has already been reported in the literature [19, 20]. In previous studies, several approximations were adopted in order to make the mathematical manipulation tractable. These simplifying assumptions were: (i) the bulk space charge due to the x-ray generated and trapped electrons and holes within the photoconductor does not appreciably perturb the electric field, i.e., the electric field remains uniform throughout the length of the detector over the period of exposure, (ii) bimolecular carrier recombination (i. e., carrier recombination between two oppositely drifting carriers) is negligible, (iii) there is no trapped charges in the photoconductor before the x-ray exposure, and (iv) the loss of the carrier is only due to deep carrier trapping and the carrier lifetime is characterized by carrier deep trapping time. Based on these assumptions, an expression for the x-ray sensitivity has been developed. The x-ray sensitivity of the detector depends on the quantum efficiency of the photoconductor, the carrier (both electron and hole) lifetime, τ; and EHP creation energy $W_{\pm}$ of the photoconductor material. Since electric field is taken to be uniform throughout the photoconductor, which means that $W_{\pm}$ is taken to be constant throughout the photoconductor thickness. These assumptions are valid for a single and low exposure. But for repeated exposures or high exposure rate, one cannot justify the assumptions above; rather one has to include the nonuniform electric field effect or recombination effect.

Instead of trapping, carriers can be lost due to recombination. There are three possible mechanism of recombination in amorphous semiconductors [21] which are illustrated in figure 1.12: (a) recombination between the drifting electrons in the conduction band (CB) with the drifting holes in the valence band (VB), (b) recombination of a CB electrons (or VB holes) with a deep trapped hole (or electron), and (c) recombination between a trapped electron with a trapped hole. The first type of recombination is known as bimolecular recombination. This recombination occurs between free electrons and holes. Electrons and holes in a photoconductor move in opposite direction due to the applied electric field. During their drift they can come close and recombine. The second or third type of recombination depends on the trapped carrier concentration and hence on the carrier lifetime. Since the carrier release time is longer, the trapped carriers accumulate inside the photoconductor. Once the trapped carrier concentration becomes large, recombination between trapped and drifting carriers (type b) becomes dominant. The trapped carriers also change the electric field distribution inside the photoconductor. For accurate modeling of the x-ray sensitivity of photoconductors, the effects of recombination or the electric field should be included. One also needs to explore the possible effects of x-ray induced deep trap center generation or the effects of dark current.

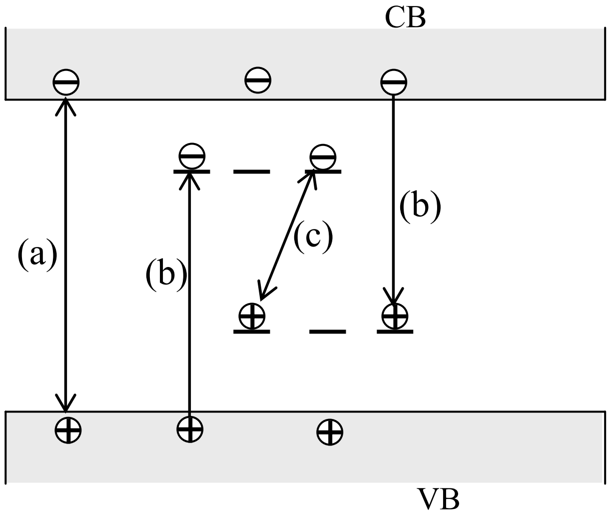

Figure 1.12 Schematic diagram of possible electron hole recombination process in a-Se.

1.6 Research Objectives

The objective of this research is to model the x-ray sensitivity of photoconductors used in direct conversion flat panel detectors based on *Monte Carlo* techniques and compare the calculations with recent experimental data.

As part of the objectives of this thesis, the model should include the following effects:

1. Trap limited sensitivity model.
2. Effects of bimolecular recombination between two oppositely drifting carriers
3. Effects of recombination between drifting and trapped carriers.
4. Trap filling effects.
5. Nonuniform electric field effects.

6. Effects of x-ray induced deep states generation.
7. Detrapping of trapped carriers.

For repeated exposures, bulk trapped carriers from one exposure can recombine with oppositely charged drifting carriers in the succeeding exposures. Deep trapping of carriers can also lead the trap filling effects, which modify the carrier lifetime. Further, the trapped carriers, or bulk space charge, perturb the uniform applied electric field, which alters the charge carrier generation via the EHP creation energy $W_{\pm}$. Typical detrapping times for trapped holes and electrons in a-Se are in the order of minutes and several hours respectively. Therefore, a considerable amount of hole (trapped) detrapping is expected during the experimental study of ghosting. It is also reported that upon exposure to x-rays, some new trap centers are generated in the photoconductor, which changes the carrier lifetime. All of these factors discussed above affect the sensitivity of the x-ray photoconductor in subsequent exposures.

In this study, the sensitivity of x-ray photoconductors for direct conversion flat panel detectors is modeled by taking into account the effects described above for different detector operating conditions: the applied bias, mammography, and chest radiography. The work described in this thesis should result a more accurate model for the x-ray sensitivity. The simulated results are then compared with the experimental data. Our study provides much insight into understanding the ghosting mechanisms in x-ray photoconductors. Since, we are dealing with carrier trapping, release and recombination, and all these processes are random, the proposed model is based on Monte Carlo simulation techniques.

1.7 Thesis Layout

This thesis consists of six chapters. Following this introductory chapter, a discussion of the properties of ideal x-ray photoconductors along with the several candidate materials to be used as an x-ray photoconductor in direct conversion flat panel detectors will be discussed in chapter 2.

Chapter 3 provides the theory of sensitivity and some important definitions related to sensitivity.

Chapter 4 deals with the Monte Carlo modeling of sensitivity. At first, we will start with the simple trap limited model, and then we will include the different effects as discussed in the research objectives.

The simulation results, explanation and a comparison with analytical/numerical and experimental results will be presented in chapter 5.

Conclusive remarks of the work and recommendations for future study are suggested in chapter 6.

2. X-ray Photoconductors

The x-ray photoconductor used in direct conversion flat panel detectors acts as an x-ray photon to electrical charge transducer, and thus plays the most important role. The performance of direct conversion flat panel x-ray detectors significantly depends on the choice and design of the x-ray photoconductor. The properties of an ideal x-ray photoconductor will be discussed in this chapter along with several candidate materials to be used as a photoconductor in a flat panel detector.

2.1 Properties of X-ray Photoconductor

Before searching for x-ray photoconductors, it is instructive to identify what characteristics will make a photoconductor perfect for a direct conversion flat panel detector. There are some general requirements that the photoconductor should meet in order to provide better performance. Ideally the photoconductor layer should posses the following material properties [8, 22-24]

- The photoconductor material must be conveniently deposited onto the large area AMA panel without the loss of uniformity and without substantially raising the temperature of the AMA. The photoconductor deposition technique has to be economically cheap and should not cause any damage to the AMA. The damaging temperature for a-Si:H panels (TFT) is around 300 °C. So the deposition should be performed below this temperature. Large area coating for use in an x-ray image detector is essential.

- Most of the incident x-ray radiation on the photoconductor should be absorbed within a practical photoconductor thickness. X-ray absorption depends on the linear attenuation coefficients (α) of the photoconductor material. The linear attenuation coefficient increases with increasing atomic number Z ($\alpha \propto Z^n$, n=3 to 5); therefore a material with higher atomic number would be preferred for this purpose. The detector thickness should be substantially greater than the absorption depth δ ($=1/\alpha$). Strong x-ray absorption is necessary in order to make use of the maximum number of x-ray photons that pass through the patient; the higher the absorption, less photons are wasted in detection and the lower the x-ray exposure required for the patient.

- Charge collection is the primary object of the detector, so the photoconductor should liberate as many electrons hole pairs (EHPs) as possible from the incident radiation in order to maximize the detected signal. This means that the amount of radiation energy required, denoted as $W_\pm$, to create a single free EHP must be low. For many material, $W_\pm$ is proportional to the bandgap energy E_g, therefore a material with a small bandgap is required. Again for some materials, $W_\pm$ depends on the applied electric field, which means that the applied field should be large for these types of materials.

- The dark current should be negligibly small. Ideally, the dark current should be zero in order to maximize the signal to noise ratio (SNR) of the detector. The dark current can arise from two sources: one from the injection of charge carriers at the electrodes, another caused by the thermal generation of free carriers in the bulk of the photoconductor itself. Carrier injection from the electrode can be blocked by making a blocking contact. A relatively wide bandgap photoconductor will reduce the thermally generated carriers from various defects or states. The dark current should preferably not exceed ~10 – 100 pA cm^{-2}, depending on the clinical application.

- The charge carriers generated through the absorption of x-ray radiation, should not be lost due to bulk recombination or deep trapping. The bulk recombination is proportional to the product of the concentrations of electrons and holes and typically it is negligible. In order to reduce the loss due to deep trapping, the *schubweg* for both electrons and holes must be greater than the photoconductor layer thickness. The schubweg, $\mu\tau F$ (where μ is the drift mobility, τ is the carrier lifetime, and F is the applied electric field) is the mean distance that a carrier drifts before it is trapped and unavailable for conduction.

- During fluoroscopic applications, the detector is continually irradiated and polled by the accompanying electronics to form real time image. Therefore, the longest carrier transit time, which depends on the smallest drift mobility, must be shorter than the access time of the pixel and inter-frame time.

- Image lag and ghosting should be low. Image lag is the carry over image charge generated by previous x-ray exposures into subsequent image frames, i.e., readout of the detector without an exposure. Ghosting is the change of the x-ray sensitivity of the detector as a result of previous exposure to radiation.

- The properties of the photoconductor should not change or deteriorate with time as a consequence of repeated exposure to x-rays, i.e., x-ray fatigue and x-ray damage should be negligible.

Large area coating requirement (maximum 35 cm × 43 cm for chest radiology) rules out the use of crystalline materials as photoconductors because they are difficult to grow in large areas. In order to meet this requirement, amorphous and polycrystalline materials are preferred as photoconductors for x-ray image detectors. The initial material that has been tried and found to be highly successful is amorphous selenium (a-Se) due to its commercial use as an electrophotographic photoreceptor [25]. Direct conversion flat panel x-ray image detectors based on a-Se photoconductors are now commercially available. An interesting feature of the a-Se based flat panel x-ray detectors is that this technology has been made possible by the use of two key elemental amorphous semiconductors: a-Si:H (used for the AMA) and a-Se (used for the x-ray photoconductor layer). Although their properties are different, both can be easily prepared in large areas, which is essential for x-ray imaging.

Amorphous selenium possesses some unique features that make it appropriate as an x-ray photoconductor in flat panel detectors. It can be easily coated as thick films (e.g., 100-1000 μm) onto suitable substrates through conventional vacuum deposition techniques without raising the substrate temperature beyond 60-70 °C. Its amorphous state maintains uniform characteristics to very fine scales over large areas. The x-ray absorption coefficient ($Z=34$) is acceptable, charge transport properties are good for both holes and electrons and the dark current level in a-Se is much smaller than many competing polycrystalline materials [8, 23, 24]. All these properties make it the preferred practical choice of photoconductor material for medical x-ray image sensors today.

Although stabilized a-Se is still the preferred choice for the photoconductor material in flat panel detectors, there has been an active research to find other potential photoconductor materials to replace a-Se because it has some properties that are disadvantageous for x-ray imaging. The intrinsic sensitivity of a-Se is low due to its high $W_{\pm}$ which decreases with increasing electric field. So, we need to apply a high electric field. A typical value of the electric field used in a-Se devices is ~ 10 V/μm and at this operating electric field, the value of $W_{\pm}$ is about 45 eV which is still much higher than other polycrystalline photoconductor materials like mercuric iodide (HgI_2) or cadmium zinc telluride (CdZnTe) where the typical value of $W_{\pm}$ is around 5-6 eV. The main drawback of polycrystalline materials is the nonuniformity of the sensitivity over large area and the higher dark current. However, there has been active research to improve the material properties and reduce the dark current in polycrystalline photoconductors and use them in flat panel x-ray image detectors. Recent experiments on large area HgI_2, PbI_2, CdZnTe, and PbO polycrystalline x-ray photoconductive layers on active matrix arrays have shown encouraging results [26-28]. More detailed descriptions of these potential photoconductors are presented in the next section.

2.2 Potential Candidates

For direct conversion flat panel x-ray detectors, a-Se has been used first and the detectors are commercially available. Later several materials have been introduced; unfortunately no material meets all the ideal characteristics as described in section 2.1. Some materials are excellent for some properties but poor for others. This section will give a brief review about the different photoconductor materials, which have been introduced for direct conversion flat panel detectors.

2.2.1 Amorphous Selenium (a-Se)

As mentioned earlier, stabilized a-Se is the most attractive photoconductor for digital flat panel detectors. Pure a-Se crystallizes over time and crystalline selenium is unsuitable as an x-ray photoconductor because it has a much lower dark resistivity than a-Se, which leads to a dark current that is orders of magnitude greater than in amorphous solids. Alloying pure a-Se with small amount of arsenic (0.2–0.5 %) prevents crystallization. However, the introduction of arsenic has adverse effect on hole lifetime because arsenic introduces deep hole traps. It was found that if the alloy is doped with 10–20 parts per million (ppm) of halogen such as chlorine, the hole lifetime is improved. This alloy is called *stabilized a-Se*.

Amorphous selenium finds widespread use as an x-ray photoconductor due to its ability to be coated over a large area and its low dark conductivity. Large area stabilized a-Se can be easily coated as thick films (e.g., 100-1000 μm) onto suitable substrates through conventional vacuum deposition techniques. Another factor in favour of a-Se is the fact that the substrate temperature during deposition can be kept below 60-70 °C and this ensures the safety of the underlying detector electronics (e.g. AMA). The temperatures that damage the AMA are around 300 ^{0}C. The dark current in a-Se is very low, usually 0.01 nA/cm^2 with conventional electrodes even for applied electric field as high as 10 V/μm.

Stabilized a-Se alloys have excellent charge transport properties (e.g. mobility, μ and carrier lifetime, τ). At room temperature, the hole drift mobility is about 0.12 cm^2/V-s, whereas the electron drift mobility is ~0.003-0.006 cm^2/V-s [8]. So, the electron drift mobility is roughly 20-40 times smaller than the hole drift mobility. The electron mobility has a weak dependence on the applied field and tends to decrease with arsenic addition. On the other hand, the charge carrier lifetimes vary substantially between different samples and have been observed to depend on factors such as the source of a-Se, impurities, and the preparation methods. The hole lifetime drops sharply with the substrate temperature, whereas the electron lifetime does not seem to depend on the substrate temperature. The electron lifetime is particularly sensitive to impurities in the a-Se source material. The reported lifetimes are 10-500 μs for holes and 100-1000 μs for electrons [8]. At typical operating fields (10 V/μm), the hole schubweg is 6-60 mm and electron schubweg is 0.3-3 mm. Since most a-Se detectors are at most ~ 1 mm thick, these large schubwegs ensure that the loss of carrier due to trapping is negligible. Note, however, that the lowest electron schubweg (0.3 mm) is less than the photoconductor thickness (1 mm), which means that electron trapping can reduce the sensitivity if the quality of the a-Se material used is not carefully controlled.

Stabilized a-Se suffers somewhat in comparison to other materials in two areas: x-ray absorption and EHP creation energy ($W_{\pm}$). First, the atomic number of selenium (Z=34) is less compared with other photoconductor materials (Z_{eff} ~ 50 for CdZnTe and Z_{eff} ~ 82 for PbO). So, a-Se is rather a poor absorber of x-rays and a thick photoconductor layer must be used to absorb the same amount of x-ray radiation as compared to a thin layer of a material with a higher atomic number. Second, $W_{\pm}$ of a-Se is highly electric field dependent; it decreases with increasing field. At typical operating fields (~ 10

V/µm), $W_{\pm}$ is reported to be approximately 35-55 eV over the diagnostic beam energy range. Detailed description of $W_{\pm}$ will be presented in chapter three.

2.2.2 Mercuric Iodide (HgI_2)

Polycrystalline mercuric iodide (HgI_2) has been under development for several years to use as an x-ray photoconductor in direct conversion flat panel detectors. The detector size of 20 cm × 25 cm for radiographic and fluoroscopic medical application has been reported [29]. One of the main disadvantages of using HgI_2 as photoconductor is its nonuniform response over the entire detector area. However, the nonuniform response from pixel to pixel has been improved by reducing the grain size [26]. One of the main advantages of using the polycrystalline HgI_2 films in direct conversion flat panel detector is that the sensitivity of HgI_2 based detector is much better than that of a-Se based detector. This is due to the material's high atomic number, low ionization energy, $W_{\pm}$, and the high mobility lifetime product of the charge carriers. The polycrystalline HgI_2 films are either vacuum deposited by physical vapour deposition (PVD) or coated on to the AMA by a wet particle-in-binder (PIB) process. After deposition of the HgI_2 photoconductor, a bias electrode is deposited on the top of the film followed by a polymer encapsulation layer. The ionization energy, $W_{\pm}$ of HgI_2 is close to 5 eV, which is independent of the electric field and much better than that of a-Se.

The dark current for HgI_2 depends on the applied electric field, operating temperature, and preparation techniques. For PVD detectors, the dark current varies from ~0.2 nA/cm^2 at 10 °C to ~18 nA/cm^2 at 25 °C for an applied electric field of 0.95 V/µm. The maximum acceptable dark current for medical imaging is 0.1 nA/cm^2. The wide range of dark currents in PVD HgI_2 detectors suggest that these detectors should be operated at relatively low electric fields (~0.5 V/µm to ~0.8 V/µm) and at relatively low temperatures (<25 °C). But the dark current level of PIB detectors is about an order of magnitude lower than that of PVD detectors. Thus, PIB detectors can be operated at temperatures up to 35 °C and at an applied electric field of 1 V/µm. Such operating conditions are not practical for PVD detectors. The disadvantage of PIB detectors is that the sensitivity of these detectors is low.

The charge transport properties (μ and τ) are superior for electrons than those of holes and also depend on the preparation process. HgI_2 deposited by the PVD process has shown better charge transport properties with $\mu\tau$ in the range of 1.4×10^{-5} cm^2/V to 1.6×10^{-5} cm^2/V for electrons [26]. The reported $\mu\tau$ for holes is of the order of $\sim10^{-7}$ cm^2/V. As reported in the literature, polycrystalline HgI_2 imagers show excellent sensitivity and good resolution.

2.2.3 Lead Iodide (PbI_2)

Polycrystalline lead iodide (PbI_2) photoconductive layers have been deposited over the AMA through the PVD technique at a substrate temperature of 200 to 230 °C and at a source temperature of 408 °C. PbI_2 evaporation is carried out in a vacuum chamber over the AMA and the evaporation is followed by the deposition of the top electrode. The detector size of 20 cm × 25 cm has been reported for radiographic and fluoroscopic medical applications [30]. The Z (atomic number) of PbI_2 is ~80 which is much higher than that of a-Se (34). The high Z value of PbI_2 indicates that PbI_2 is an efficient material for absorbing x-rays. The bandgap energy of polycrystalline PbI_2 is 2.3 eV and the effective ionization energy, $W_{\pm}$ is ~5.5 eV. The lower value of $W_{\pm}$ ensures a higher sensitivity of PbI_2 based detectors.

The dark current in PbI_2 imagers increases sublinearly with the applied electric field and the level of dark current is too high for long exposure time applications. With an applied field of 0.5 V/μm, dark current is ~15 nA/cm^2. The hole and electron ranges ($\mu\tau$) are 1.8×10^{-6} cm^2/V and 7×10^{-8} cm^2/V, respectively. The x-ray sensitivity of PbI_2 detectors increases with the electric field due to the increase of charge collection efficiency with the electric field. The sensitivity almost saturates at the electric field of 0.2 V/μm. The reported sensitivity of PbI_2 detector is over 6 μC/R/cm^2. The spatial resolution and DQE of PbI_2 based detector are in the acceptable range for imaging applications.

2.2.4 Cadmium Zinc Telluride (CdZnTe)

Polycrystalline cadmium zinc telluride (CdZnTe) photoconductive layer has been reported for flat panel x-ray detectors [27]. The attractive feature of CdZnTe detectors is that they exhibit excellent efficiency at low x-ray exposures due to their high sensitivity. CdZnTe films were deposited by closed spaced sublimation method. The furnace temperature is about 600 °C. A sintered mixture of cadmium telluride (CdTe) and zinc telluride (ZnTe) are used as source materials. One of the main disadvantages of CdZnTe is that it can not be deposited directly onto the AMA, but instead a hybrid technique is applied in which CdZnTe is pre-deposited on a substrate and then bonded to the AMA substrate.

The ionization energy $W_{\pm}$ is ~5 eV, and bandgap energy is ~1.7 eV (bandgap energy depends on Zn concentration), and resistivity of the material is ~10^{11} Ω-cm. The $\mu\tau$ of electrons in polycrystalline CdZnTe is better than that of holes. The $\mu\tau$ for holes and electrons are ~10^{-4} cm^2/V and ~5×10^{-4} cm^2/V, respectively, both much larger than those of polycrystalline HgI_2 and a-Se.

The dark current in polycrystalline CdZnTe increases with the applied electric field and has been reported to be 7 nA/cm^2 at an applied electric field of 0.25 V/μm. The dark current decreases with increasing Zn concentration in CdZnTe. Both the dark current and the image lag characteristics are higher than HgI_2, but the sensitivity of CdZnTe is much greater than any other photoconductor layer. The sensitivity of the CdZnTe detector depends on the applied electric field and increases with increasing electric field. At an applied field of 0.4 V/μm, the reported sensitivity is 68.8 μC/R/cm^2. But the disadvantages of CdZnTe are poor spatial resolution, large image lag, and a lack of uniformity. Chlorine doping into CdZnTe photoconductive layer improves their performance. Long term stability and ghosting have not yet been investigated in CdZnTe based detectors.

2.2.5 Lead Oxide (PbO)

Recently, flat panel detectors with lead oxide (PbO) as direct conversion photoconductive material, with an active area of 18 cm × 20 cm, has been reported [28]. PbO layers have been prepared through a direct evaporation process onto the substrate in a high vacuum chamber. The substrate temperature can be maintained at 100 °C and the source temperature was 900-950 °C. Using this technique, it is possible to deposit PbO layers 300 μm thick on a size of 25 cm × 25 cm. One of the main advantages of using PbO as an x-ray photoconductor is that PbO is an excellent absorber of x-ray photons. The bandgap energy of PbO is 2.3 eV and the ionization energy is ~8 eV.

PbO photoconductive detectors exhibit a linear response over the entire area of the detectors. The dark current of PbO is ~5 nA/cm^2 at 3 V/μm. Residual signal (lag) is around 10 % which is quite high for imaging application. So the temporal behaviour or residual lag should be improved to compete with other photoconductor materials. The sensitivity is sufficient for low dose applications. Imaging performances, such as linear response, high DQE, and spatial resolution have been reported to be acceptable for imaging applications.

2.2.6 Summary of Potential Candidates

Tables 2.1, 2.2, and 2.3 summarize the preparation methods, properties, and imaging performance of the photoconductor discussed above to use as an x-ray photoconductor in flat panel detectors.

Table 2.1 Preparation methods and temperature for different photoconductors.

Photo Conductor	Preparation technique	Temperature	Reported max. Size for use in AMA
a-Se	Vacuum deposition	Source temp. 250 °C and substrate temp. 60-70 °C	43 cm×43 cm
HgI_2	Vacuum deposition by PVD	Suitable evaporator and array temperature	20 cm×25 cm
PbI_2	Vacuum deposition by PVD	Source temp. 408 °C and substrate temp. 200-230 °C	20 cm×25 cm
CdZnTe	Close-spaced sublimation (CdZnTe is pre-deposited on a substrate and then connected with the AMA)	Furnace temperature 600 °C	7.7 cm×7.7 cm
PbO	Vacuum deposition by direct evaporation	Source temp. 900-950 °C and substrate temp. 100 °C	18 cm× 20 cm

Table 2.2 Comparison of the physical properties of the candidates discussed above to be used as x-ray photoconductor.

	Desired	a-Se	HgI_2	PbI_2	CdZnTe	PbO
δ (µm) at 20 keV	Low	48	32	28	~ 60	11.8
δ (µm) at 60 keV	Low	976	252	259	~ 280	218
E_g (eV)	High	2.3	2.1	2.3	1.7	1.9
$W_{\pm}$ (eV)	Low	45 at 10 V/µm	~5	~5.5	~5	8
$\mu_h \tau_h$ (cm^2/V)	High	0.6×10^{-5} - 6×10^{-5}	$\sim10^{-7}$	1.8×10^{-6}	$\sim10^{-4}$	?
$\mu_e \tau_e$ (cm^2/V)	High	0.3×10^{-6} - 3×10^{-6}	1.4×10^{-5} - 1.6×10^{-5}	7×10^{-8}	$\sim5\times10^{-4}$	?

Table 2.3 Comparison of the imaging properties of different photoconductors as discussed above

Photo conductor	Normal operating field (V/μm)	Dark current (nA/cm^2)	Sensitivity ($\mu C/R/cm^2$)	Image lag	Comments
Desired	Low	Low	High	Low	
a-Se	10	~ 0.1	~0.2 (L = 200 μm and 60 kV_p)	< 1 % (After 1s)	Although sensitivity is low but dark current and image lag is are very low which make it an ideal photoconductor for FPD
HgI_2	1	~ 13	10 (L = 300 μm and 60 kV_p)	<10 % (After 67 ms)	The dark current and image lag are not good but sensitivity is very high.
PbI_2	0.2	~ 10	6 (L = 120 μm and 60 kV_p)	50 % (After 67 ms)	Image lag is very high, dark current is not in the acceptable range but sensitivity is high
CdZnTe	0.25	7	24 (L = 314 μm and 80 kV_p)	18 % (After 33 ms)	Sensitivity is very high but dark current and image lag are not good. It also suffers from the lack of homogeneity.
PbO	3	5	?	8 % (After 33 ms)	It suffers from lack of lateral homogeneity. Sensitivity is good but dark current and image lag are not good.

3. Sensitivity

The sensitivity of a photoconductor material to x-rays is of major concern in x-ray imaging. The more sensitive the detector is, the image quality is greater and fewer doses are required to expose the patient. The total collectable charge from absorbed x-ray photons must be maximized for an x-ray detector. The theory of sensitivity and some important parameters required to calculate sensitivity are discussed in this chapter.

3.1 X-ray Sensitivity

The sensitivity of an x-ray photoconductor is defined as the collected charge per unit area per unit exposure of radiation,

$$S = \frac{Q_{coll}}{AX} \tag{3.1}$$

where A is the radiation receiving area, and X is the radiation exposure normally measured in *Roentgen*, and Q_{coll} is the collected charge in the external circuit. The amount of exposure required to deposit 0.00873 *Joules* energy in one kilogram (kg) of air is one Roentgen. When x-ray radiation is incident on a photoconductor, three events or processes can take place:

(i) Some of the x-ray energy is absorbed in the photoconductor, which depends on *energy absorption coefficient* and the *quantum efficiency* of the photoconductor material.

(ii) The absorbed energy liberates electron hole pairs (EHPs) and the number of liberated EHPs depends on the electron hole pair creation energy $W_{\pm}$ of the photoconductor materials.

(iii) From the generated EHPs, some carriers will be lost and some carriers will be collected in the external circuit, which depends on the charge transport properties of the photoconductor.

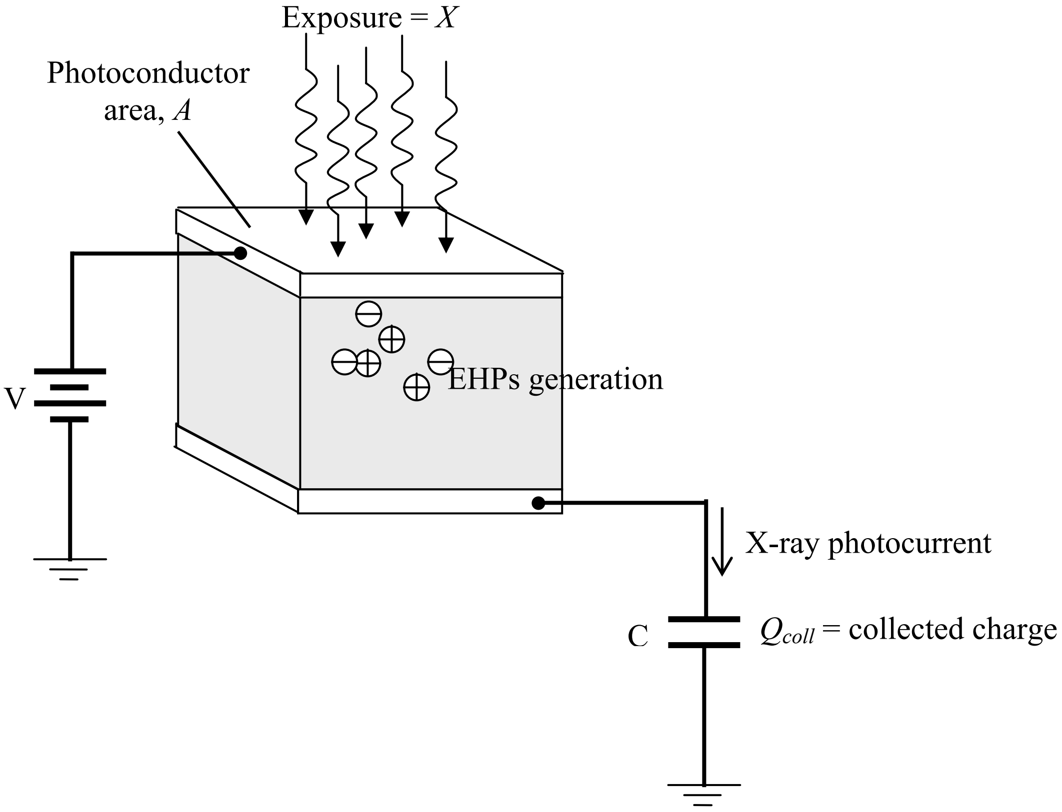

Figure 3.1 Schematic illustration of the photoconductor sandwiched between two parallel plate electrodes.

3.1.1 X-ray Absorption and Quantum Efficiency

When x-ray photons are incident on a medium (attenuator), they interact with the medium. Not all x-ray photons interact with the medium. If an attenuator of thickness *dx* is placed in the path of the x-ray radiation, the number of x-ray photons that interact with the attenuator is proportional to the product of the attenuator thickness and the number of x-ray photons in the beam [31]. A schematic illustration of this attenuation is shown in figure 3.2.

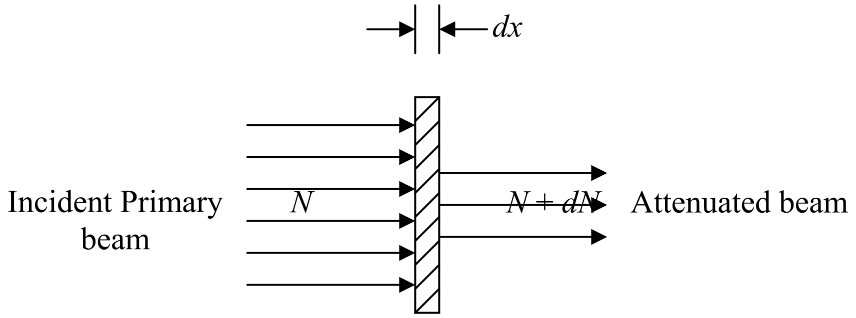

Figure 3.2 Schematic illustration of attenuation of x-ray photons in a medium.

If *dN* represents the change in the number of x-ray photons in the beam passing through a thickness *dx*, than

$$dN \propto Ndx$$

$$\therefore \quad dN = -\alpha N dx \qquad 3.2$$

where α is the proportionality constant, which is called the *linear attenuation coefficient* of the medium. Negative sign indicates the reduction of transmitted photons. The definition of α can be given by

$$\alpha = \frac{dN/N}{dx} = \frac{\text{Fraction of photons that interract within } dx}{\text{Thickness of the medium } dx} \qquad 3.3$$

Hence the linear attenuation coefficient of a medium is defined as the fraction of the x-ray photons that interact per unit thickness of the medium. From Eq. 3.2, we get

$$\int_{N_0}^{N} \frac{dN}{N} = -\int_0^x \alpha dx$$

$$\therefore \quad N(x) = N_0 e^{-\alpha x} \qquad 3.4$$

where N_0 is the number of incident photons and N is the transmitted photons at a thickness x measured from the radiation receiving surface of the photoconductor. Thus, the x-ray photon flux attenuates exponentially in the medium characterized by the attenuation coefficient of the medium. Equation 3.4 can be expressed as the photon concentration per unit thickness as

$$N_{ph}(x) = N_0 \alpha e^{-\alpha x}. \qquad 3.5$$

Here $N_{ph}(x)$ represents the photon concentration per unit thickness. The linear attenuation coefficient of the material depends on the incident photon energy, E_{ph}, the atomic number of the material, Z, and the density d of the material. The linear attenuation coefficient varies with photon energy approximately as E_{ph}^{-3}, and it increases with the atomic number Z of the material, as $\alpha \propto \mathrm{Z}^n$, where n ~ 3-4. The fraction of the x-ray photons attenuated by the photoconductor is referred to as the quantum efficiency and is denoted by η. If the photoconductor thickness is L, then the quantum efficiency can be expressed as

$$\eta = \frac{\int_0^L N_0 \alpha e^{-\alpha x} dx}{N_0}$$

$$\therefore \qquad \eta = [1 - \exp(-\alpha L)] \qquad 3.6$$

The reciprocal of α is called the attenuation depth δ, where the x-ray photon beam has been attenuated by 63%. Table 2.2 summarized the attenuation depths for various x-ray photoconductor materials at photon energies of 20 keV (x-ray spectrum for mammographic application) and 60 keV (x-ray spectrum for chest radiographic application). In general, a high absorption coefficient is preferred (low δ), since the minimization of patient dose requires that most of the x-ray radiation incident on the detector should be absorbed within it, i.e. the detector length, L, must be greater than δ. Hence the required detector thickness depends on the photon energy and thus on the type of imaging applications. Typically, L should be several times δ.

However, the detector cannot be made very thick. A thick detector would absorb more x-ray radiation but there is a higher probability that the freed charges will be lost due to trapping as they have to drift greater distances to reach the electrodes. The response speed of the detector must also be considered if it is designed to operate in the fluoroscopic mode (real time imaging).

When an x-ray photon interacts with the photoconductor material, a complicated series of interactions take place and it may not impart all its energy to the photoconductor material. Some of the energy is absorbed by the material and part of the energy is radiated or scattered out, as shown in figure 3.3.

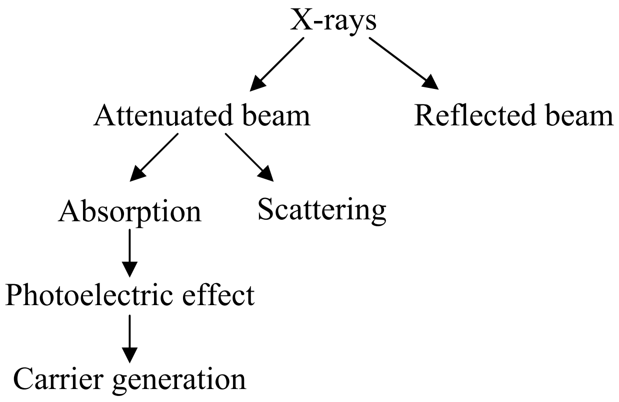

Figure 3.3 Schematic representations of x-ray attenuation, energy absorption, and carrier generation.

Thus, it becomes obvious that the linear attenuation coefficient of a material cannot be used to calculate the amount of energy that an x-ray beam deposits in that material. In order to calculate the energy deposited by the beam, we need the *energy absorption coefficient* denoted by α_{ab}. Whereas the linear attenuation coefficient is a measure of the fraction of photons that will interact with a given thickness of material, the energy absorption coefficient is a measure of how much energy is absorbed by the attenuator through these photons that interact with it. The energy absorption coefficient is related to the linear attenuation coefficient through [31],

$$\alpha_{ab} = \alpha(\overline{E}_{ab} / E_{ph}), \tag{3.7}$$

where α_{ab} is the linear absorption coefficient, E_{ph} is the photon energy and $\overline{E}_{ab}$ is the average energy absorbed from each photon. The absorbed energy profile can be expressed as (from Eq. 3.5)

$$E_{ab}(x) = \overline{E}_{ab} N_0 \alpha e^{-\alpha x}$$

$$\therefore \quad E_{ab}(x) = \alpha_{ab} E_{ph} N_0 e^{-\alpha x}. \tag{3.8}$$

Here $E_{ab}(x)$ is the absorbed energy per unit thickness of the photoconductor. In order to calculate the energy absorption profile, we need to calculate the incident photons (N_0) from the incident radiation. If Φ is the photon fluence of the incident radiation, i.e., the number of photons per unit area per unit Roentgen, then the total number of incident photons on a detector area A is

$$N_0 = \Phi A X . \tag{3.9}$$

Here X is the amount of exposure in Roentgen. The photon fluence can be easily calculated from the definition of one Roentgen and the mass energy absorption coefficient $(\alpha_{en}/\rho)_{\mathrm{air}}$ of air via Ref. 31.

$$\Phi = \frac{5.45\times10^{16}}{E_{ph}\left(\alpha_{en}/\rho\right)_{\mathrm{air}}} \tag{3.10}$$

where E_{ph} is the energy of the photon (considering monoenergetic beam), $\alpha_{en,\mathrm{air}}$ is the energy absorption coefficient of air, ρ_{air} is the density of air and $(\alpha_{en}/\rho)_{\mathrm{air}}$ is called the mass energy absorption coefficient of air which also depends on the photon energy E_{ph}. From Eqs. 3.8 to 3.10, the absorbed energy profile can be evaluated from an exposure X via the mass energy absorption coefficient of air,

$$E_{ab}(x) = \frac{5.45\times10^{16}}{\left(\alpha_{en}/\rho\right)_{\mathrm{air}}} A X \alpha_{ab} e^{-\alpha x} \tag{3.11}$$

3.1.2 EHP Generation and Ionization Energy ($W_{\pm}$)

The incident x-ray energy is absorbed by the photoconductor and generates EHPs. The generation of EHPs by an incident energetic particle such as an x-ray photon first involves the generation of an energetic primary electron by ionizing an inner core shell, e.g., the K-shell. As this energetic projectile photoelectron travels in the solid, it causes ionization along its track and hence the creation of many EHPs. Total collectable generated EHPs from absorbed energy of ΔE_{ab} is $\Delta E_{ab}/W_{\pm}$. Therefore, $W_{\pm}$, the amount of energy required to create a single EHP must be as low as possible in order to maximize the amount of detectable charges ΔQ ($= e\Delta E_{ab}/W_{\pm}$) produced by the incident radiation. Thus, any candidate material for an x-ray photoconductor in direct conversion x-ray imaging must have an excellent x-ray photoconductivity (low $W_{\pm}$). The generated carrier profile can be written as

$$c(x) = \frac{E_{ab}(x)}{W_{\pm}} = \frac{5.45\times10^{16}}{W_{\pm}\left(\alpha_{en}/\rho\right)_{\text{air}}} AX\alpha_{ab}e^{-\alpha x} \qquad 3.12$$

where $c(x)$ is the number of generated carriers (electron or hole) per unit thickness of the photoconductor at a thickness x measured from the radiation receiving surface of the photoconductor.

For most semiconductor materials, $W_{\pm}$ has been shown to depend on the bandgap energy E_g via Klein's rule [32] $W_{\pm} \approx 2.8E_g + E_{phonon}$. The phonon energy term E_{phonon} is expected to be small (<0.1 eV) so that typically $W_{\pm}$ is close to $2.8E_g$. Figure 3.4 shows the correlation between $W_{\pm}$ and E_g, the solid line represents a $W_{\pm} \approx 2.8E_g$ behaviour.

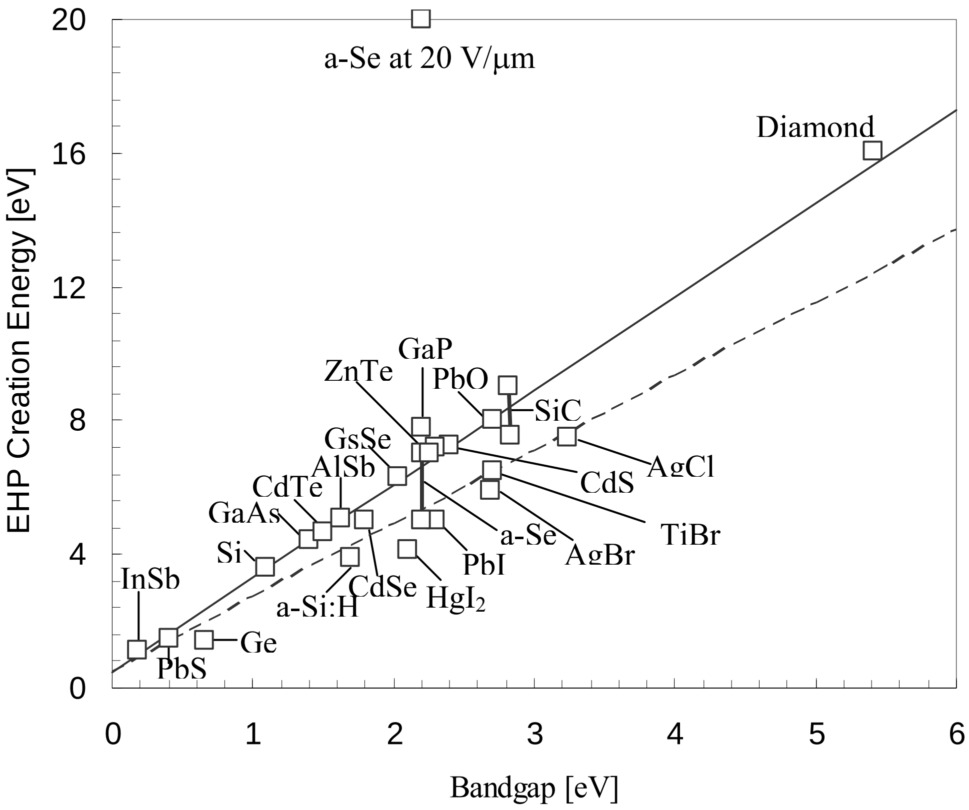

Figure 3.4 EHP creation energy vs bandgap energy E_g for various materials [8].

Many semiconductors follow the Klein's rule, but there are also a number of materials such as a-Si:H, PbI_2 and AgCl that have $W_{\pm}$ values substantially less than that predicted by Klein's rule. Since polycrystalline and amorphous materials are inherently disordered, according to Que and Rowlands [34], the EHP creation energy in these materials follows $W_{\pm} \approx 2.2E_g + E_{phonon}$. This is illustrated as the dashed line of figure 3.4. It should be noted that there are some materials, such as stabilized a-Se, that exhibit electric field dependent $W_{\pm}$. Figure 3.5 shows the field dependent $W_{\pm}$ of a-Se for monoenergetic x-rays of different photon energies [35]. The lowest or saturated $W_{\pm}$, denoted as $W_{\pm}^{sat}$, can be obtained at the highest field. Therefore, for a-Se with $E_g \approx 2.2$ eV, application of Que and Rowlands theory would lead to $W_{\pm}^{sat} \approx 5.3$ eV. By extra plotting the field dependent $W_{\pm}$ to high field, the estimated value of $W_{\pm}^{sat}$ seems to be 6-10 eV. In addition, the apparent $W_{\pm}$ has been observed to decrease with the photon energy as apparent in figure 3.5. But the dependence of $W_{\pm}$ on photon energy is much weaker than on the electric field.

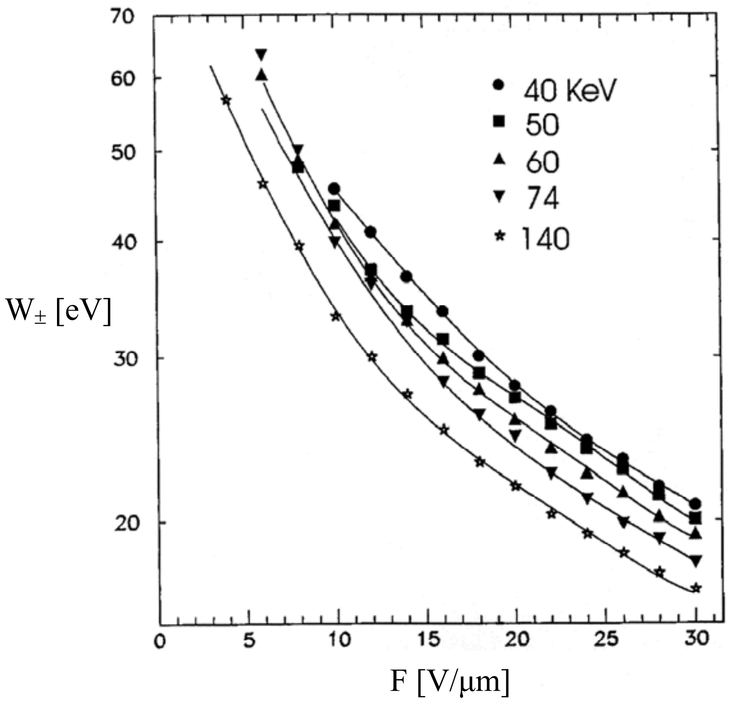

Figure 3.5 EHP creation energy of a-Se as a function of electric field for various x-ray photon energies [34].

The field dependence of $W_{\pm}$ in a-Se may arise from the recombination mechanism operating for the EHPs generated by the primary electron. The Monte Carlo simulation of field dependent $W_{\pm}$ in a-Se considering the initial ion recombination has been modeled by Lachaine et al.[36]. The primary electron generates many EHPs, but only a fraction of those EHPs will be collected. Losses of EHPs occur due to the recombination and trapping processes. But in the case of a high quality photoconductor, carrier loss due to trapping is negligible. Then the recombination losses can be attributed to three sources: bulk or *bimolecular* recombination between drifting holes and electrons, g*eminate* recombination, and c*olumnar* recombination.

In bulk recombination, the recombination rate is proportional to the product of hole and electron concentrations, so that the collected charge would exhibit a square root dependence on the x-ray intensity. However, experiments showed that collected charge increases linearly with the intensity of the x-rays, which rules out this type of recombination.

Geminate recombination occurs between the generated twin electrons and holes. The simultaneously generated electron and hole face a strong mutual Coulombic force and may recombine. The number of EHPs that escape geminate recombination is governed by the Onsager model [37]. This type of recombination is accepted for the interaction of visible photons with a-Se, so it is natural to also apply the same recombination mechanism in the x-ray regime.

Columnar recombination involves the recombination of non-geminate electrons and holes within the columnar track of a primary electron, i.e. bimolecular recombination within a track. Since x-ray photons generate thousands of EHPs, the geminate recombination mechanism is not applicable to initial ion recombination in the x-ray regime; rather columnar recombination, first derived by Jaffe [39], is responsible for the recombination process as proposed by Hirsch and Jagankhani [38]. Experiments carried out on a-Se over the diagnostic energy range tend to support the columnar recombination model.

There is no unique model for the field dependent $W_\pm$ in a-Se. Based on experimental data, it is concluded that $W_\pm$ in a-Se has a strong dependence on the electric field and a weak dependence on photon energy. $W_\pm$ at a given x-ray energy follows an empirical relationship that has a field dependence as follows

$$W_\pm \approx W_\pm^{\mathrm{sat}} + \frac{B}{F^n} \tag{3.13}$$

where B is a constant that depends on the photon energy and n is typically 0.7 - 1 [19]. By fitting the experimental data [35] and Monte Carlo modeled $W_\pm$ [36], the following relationship of $W_\pm$ with electric field F and photon energy E_{ph} is obtained which has been used throughout the calculation for electric field and energy dependent $W_\pm$.

$$W_\pm = \left(6 + \frac{15\times10^6}{F^{0.8}}\right)\times\left(0.72 + 0.56\times\exp(-E_{ph}/62700)\right) \tag{3.14}$$

where F is the electric field in V/m and E_{ph} is the photon energy in eV. The above equation is an empirical expression that describes the data in figure 3.5. The accuracy of Eq. 3.14 representing the reported W-F-E_{ph} data is shown in figure 3.6.

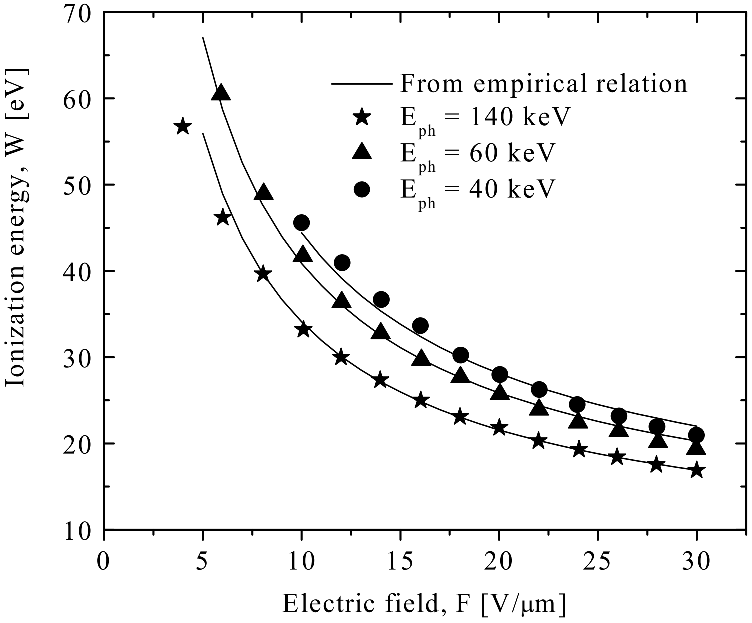

Figure 3.6 Comparison of the ionization energy, $W_\pm$ between the experimental data and the calculated values using the relation as given by equation 3.13. The experimental data has been extracted from figure 5 of Ref. 34.

3.1.3 Normalized Sensitivity

Usually the sensitivity of a photoconductor is expressed in terms of the normalized sensitivity. The normalized sensitivity (*s*) is defined as the ratio of the actual sensitivity (*S*) to the maximum possible sensitivity (S_0). The maximum sensitivity of a detector would arise if all of the incident photons were attenuated and all of the liberated carriers were collected. Thus, it assumes that the quantum efficiency is unity. It is also assumes that all the photogenerated carriers are collected. According to Eq. 3.12, the maximum collectable charge Q_0 would be

$$Q_0 = \frac{5.45\times10^{16}\times eAX\alpha_{ab}}{W_{\pm}^{0}(\alpha_{en}/\rho)_{air}}\int_0^{\infty} e^{-\alpha x}dx = \frac{5.45\times10^{16}\times eAX}{W_{\pm}^{0}(\alpha_{en}/\rho)_{air}}\left(\frac{\alpha_{ab}}{\alpha}\right) \qquad 3.15$$

where *e* is the elementary charge of the electron and $W_{\pm}^{0}$ is the EHP creation energy at the uniform applied field F_0 (i.e., *V*/*L*, where *V* denote the applied bias and *L* is the photoconductor thickness). A uniform electric field means that the electric field does not change along the thickness of the photoconductor. So, the normalized sensitivity can be expressed as

$$s = \frac{S}{S_0} = \frac{Q_{coll}}{Q_0}\,. \qquad 3.16$$

Since, the photoconductor thickness is not infinite, not all x-ray photons will be attenuated. The photogenerated charge (Q_{gen}^{0}) at the uniform applied field F_0 within the finite thickness *L* of the photoconductor is

$$Q_{gen}^{0} = \frac{5.45\times10^{16}\times eAX\alpha_{ab}}{W_{\pm}^{0}(\alpha_{en}/\rho)_{air}}\int_0^{L} e^{-\alpha x}dx = \frac{5.45\times10^{16}\times eAX}{W_{\pm}^{0}(\alpha_{en}/\rho)_{air}}\left(\frac{\alpha_{ab}}{\alpha}\right)\times\eta \qquad 3.17$$

where η is the quantum efficiency of the photoconductor and is given by Eq. 3.6. By using Eqs. 3.15 to 3.17, we get

$$s = \frac{Q_{coll}}{Q_{gen}^{0}}\times\eta \qquad 3.18$$

Q_{gen}^{0} depends on the electric field via $W_{\pm}^{0}$. If the applied electric field does not change, then for different exposures, $W_{\pm}^{0}$ is same throughout the thickness of the photoconductor and the generated carriers Q_{gen}^{0} would also be same. Thus, the normalized sensitivity will depend only on the collected charge Q_{coll}. But the electric field may change within the photoconductor due to charges inside the photoconductor. The change in the electric field changes $W_{\pm}$ which modifies the total generated carriers in subsequent exposures. By including the nonuniform electric field effect on the EHP creation energy $W_{\pm}$, the normalized sensitivity expression (Eq. 3.18) can be rearranged as

$$s = \frac{Q_{gen}}{Q_{gen}^{0}} \times \frac{Q_{coll}}{Q_{gen}} \times \eta = \mathrm{PGR} \times \mathrm{CCE} \times \mathrm{QE} \qquad 3.19$$

Here Q_{gen} represents the actual generated charge including nonuniform electric field effects and Q_{gen}^{0} is the generated charge when the applied electric field is uniform, that is $F=F_0$ ($=V/L$). The first term in Eq. 3.19 can be defined as the *photogeneration ratio* (PGR), which is the ratio of the generated charge carriers to the carriers that will be generated if the electric field is uniform throughout the photoconductor. The second term in Eq. 3.19 is known as the *charge collection efficiency* (CCE) defined as the ratio of the collected charge to the generated charge. The third term is the *quantum efficiency* (QE) denoted by η as defined by Eq. 3.6 and is constant for a particular photoconductor material with a particular thickness for a given radiation energy. So, the normalized sensitivity depends on the PGR and CCE. For an ideal photoconductor, PGR and CCE, both should be unity and in this case the normalized sensitivity would be equal to the QE. But in practical photoconductors, CCE is less than unity. The PGR can be greater than or less than unity depending on the electric field distribution inside the photoconductor. Thus, in order to calculate the normalized sensitivity of a photoconductor; we need to calculate the PGR and CCE.

The PGR can be expressed as

$$\mathrm{PGR} = \frac{\mathrm{Q_{gen}}}{\mathrm{Q_{gen}^{0}}} = \frac{\int_0^L \frac{e^{-\alpha x}}{W_{\pm}(x)} dx}{\int_0^L \frac{e^{-\alpha x}}{W_{\pm}^{0}} dx}$$

$$\therefore \qquad \text{PGR} = \frac{\alpha}{\eta}\int_0^L \frac{W_{\pm}^0}{W_{\pm}(x)} e^{-\alpha x} dx \qquad 3.20$$

where $W_{\pm}^0$ is the ionization energy when the applied field is $F = F_0 = V/L$. If electric field is uniform throughout the photoconductor thickness, $W_{\pm}$ will be equal to $W_{\pm}^0$ and, according to Eq. 3.20, the PGR ratio will be unity.

3.2 Induced Current and Collected Charge

According to the Shockley-Ramo theorem [40, 41], if a point charge q is drifting with a velocity $v_d(t)$ by an electric field between two biased electrodes separated by L, the motion of the point charge, q, induces a current in the external circuit given by

$$i(t) = \frac{qv_d(t)}{L}; \quad t < t_{transit} \qquad 3.21$$

The total external current is the sum of all currents of the type in Eq. 3.21 from all the drifting charges between the electrodes. Thus, in the case of an x-ray photoconductor, the current contribution from electrons and holes can be written by

$$i_e(t) = \frac{eN_e\mu_e F}{L} \qquad 3.22a$$

$$i_h(t) = \frac{eN_h\mu_h F}{L} \qquad 3.22b$$

$$i_{ph} = i_e + i_h \qquad 3.22c$$

Here N_e and N_h are the total number of drifting electrons and holes inside the photoconductor, respectively, at time t, F is the applied uniform electric field, and μ is the mobility of the corresponding carrier. The total photocurrent is the summation of electron and hole contributions. This is shown in figure 3.7.

In the presence of a nonuniform electric field, Eqs. 3.22 (a) and (b) can be rewritten as

$$i_e(t) = \frac{e\mu_e}{L}\sum_{j=0}^{N_e} F_j(x_j) \ , \qquad 3.23a$$

$$i_h(t) = \frac{e\mu_h}{L}\sum_{j=0}^{N_h} F_j(x_j) \ , \tag{3.23b}$$

where $F_j(x_j)$ is the field experience by a carrier i at location x_i. Total collected charge is evaluated by integrating the total photocurrent i_{ph}, i.e.,

$$Q_{coll} = \int_0^T i_{ph}dt \ . \tag{3.24}$$

Here T is time period during which carriers are drifting inside the photoconductor. Note that it is assumed that the drift mobility is field independent.

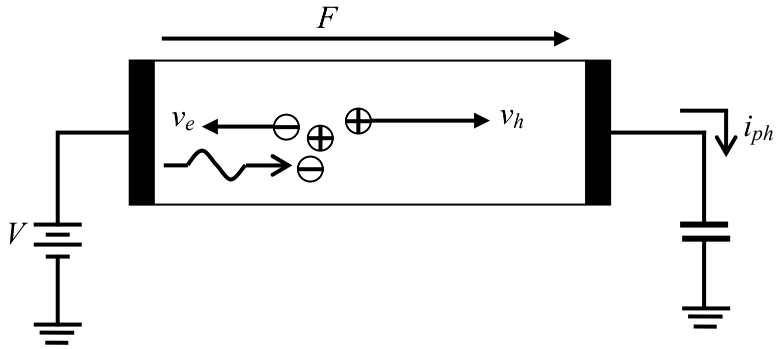

Figure 3.7 Schematic illustrations of carriers drift and current in a positively biased x-ray photoconductor.

3.3 Drift Mobility and Deep Trapping Time

Unlike the abrupt density of states (DOS) of crystalline semiconductors, the DOS in amorphous semiconductors extends into the bandgap giving rise to localized states. These localized states are simply *traps* and control the charge carrier transport in amorphous semiconductors. Depending on the position on the energy scale, the localized states can be *shallow* or *deep*, as shown in figure 3.8. Localized states close to the band edge are known as shallow states. The states deep inside the bandgap are known as deep states as detrapping from these states is negligible.

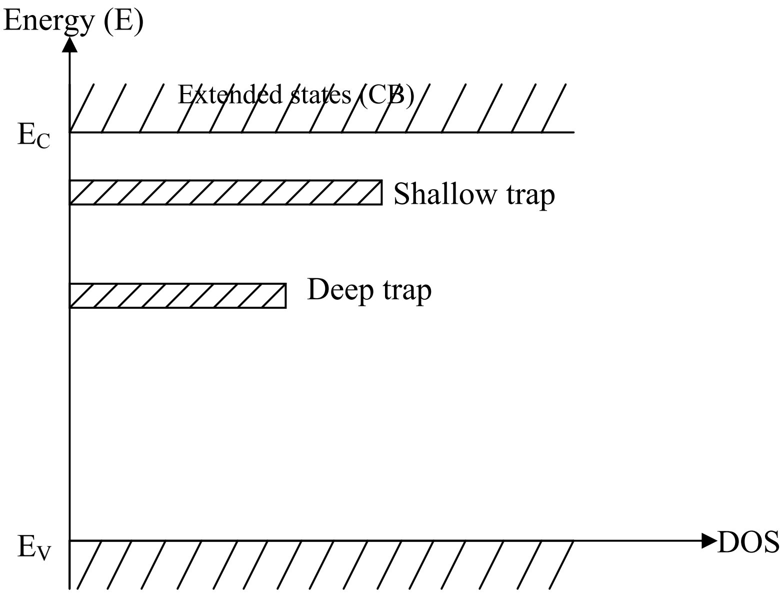

Figure 3.8 Schematic illustration of shallow and deep traps for electrons in amorphous semiconductors.

When carriers are drifting inside the extended states, they can get trapped in localized states; this process is known as carrier *trapping*. Physically, carrier trapping means that the carrier is still present but it has lost its mobility. Each carrier takes a certain time to get trapped. The average of this time is referred to as the carrier trapping time or lifetime. The carrier trapping time depends on the concentration of the trap centers. If the trap concentration is N_t, then the carrier trapping time is given by

$$\tau_t = \frac{1}{C_t N_t} = \frac{1}{C_r v_{th} N_t} \qquad 3.25$$

where C_t is the carrier *capture coefficient* which is the product of the carrier capture cross section (C_r) multiplied by the thermal or mean velocity (v_{th})of the carrier.

If a free carrier is trapped in the localized states, after some time interval, it may be released from the localized states to the extended states and regain its mobility; this process is known as carrier *release*. The time the carrier spends in the localized states or the time the carrier takes to be released from the localized states is called the release time. The release time depends on the energy position of the states where the carrier is trapped. The release time depends on the Boltzmann factor and the phonon frequency ν, i.e.,

$$\tau_r = \frac{1}{\nu}\exp\left(\frac{E_t}{kT}\right) \qquad 3.26$$

here ν is the attempt to escape frequency or *phonon frequency* (typical value is 10^{12} s^{-1}), E_t is the trap depth below the relevant conduction band edge, k is the Boltzmann's constant, and T is the temperature in Kelvin. The process of carrier trapping and release are shown in figure 3.9.

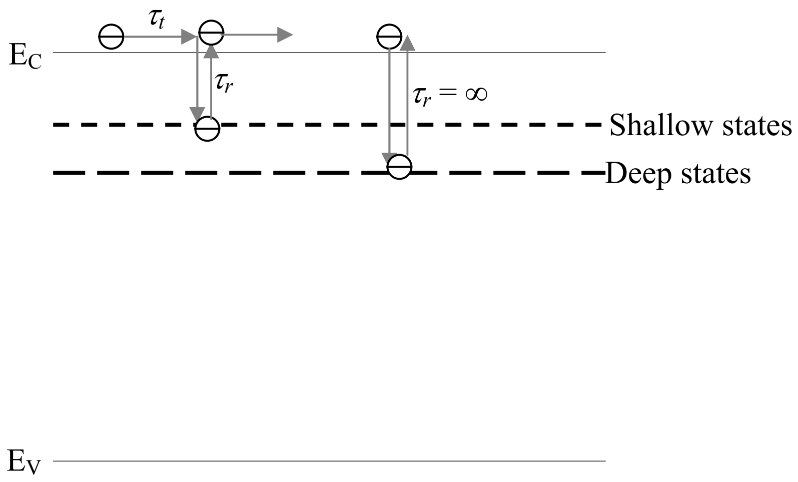

Figure 3.9 Carrier trapping and release in amorphous semiconductors.

A trapped carrier in the shallow states is quickly released to the extended states and immediately starts drifting. Since the number of shallow states is much higher than the number of deep states, a carrier's drift involves frequent trapping and release from the shallow states. Thus, the carrier trapping in shallow states represents a temporary loss of a carrier. Eventually the carrier will reach the opposite electrode. The multiple trapping and release of carriers in the shallow states increases the transit time by effectively reducing the drift mobility, i.e., the carriers are free to conduct only during a fraction of time while they reside above the mobility edge. This reduced mobility is given by

$$\mu_{\text{drift}} = \mu_0 \frac{\tau_t}{\tau_t + \tau_r} \qquad 3.27$$

where μ_0 is the trap-free mobility of the carrier. The release time from deep states is much greater than that from shallow states. So, it can be approximated that carrier trapping in deep states represents the permanent loss of the carrier.

The distribution of shallow and deep states is not discrete but rather follows a distribution of states in the mobility gap. A simplified diagram of the DOS as a function of energy for amorphous selenium is shown in figure 3.10.

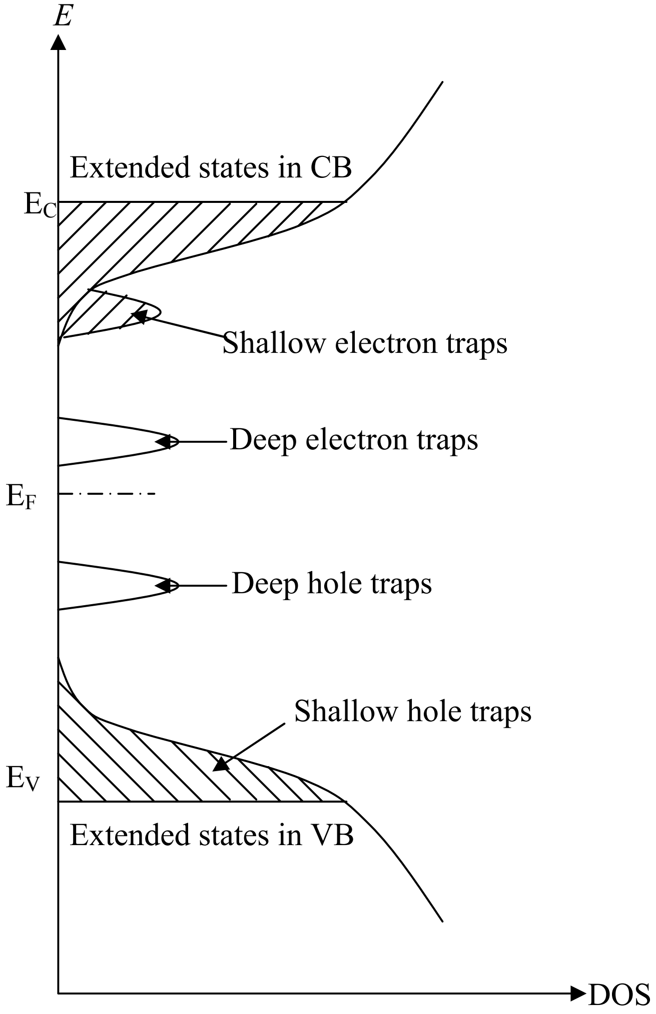

Figure 3.10 A simplified diagram of DOS in amorphous selenium

Consequently, there will be several trapping and release events, which makes the charge carrier transport process complicated. Again, there is much debate about the exact form of the DOS function within a-Se which controls the charge carrier trapping and release. But our objective is to calculate the sensitivity of the photoconductor. Given the complicated process of charge carrier transport and the current controversy on the DOS in a-Se, it is not worthwhile to speculate on the exact physics of charge carrier transport, except to assume that the DOS is such that one can assign a constant *drift mobility* (normally denoted by μ) and a single *deep trapping time* (normally denoted by τ) for both types of carriers. Later subscript e will be used to denote electrons and h will be used to denote holes. These are valid assumptions for the calculation of sensitivity, since shallow trapping and the exact physics of the charge carrier transport process is not required in the calculation of sensitivity, rather shallow trapping can be included in the effective drift mobility. Time-of-flight (TOF) and interrupted field time-of-flight (IFTOF) experiments have also justified these assumptions. TOF experiments show that in the case of a-Se and stabilized a-Se, the electron and hole mobilities are independent of the sample thickness and IFTOF experiments indicate a single deep trapping time to each species of carriers; the drifting carrier concentration falls exponentially as $\exp(-t/\tau)$, where τ is the carrier lifetime.

4. Monte Carlo Modeling

In the previous chapter, the theory of x-ray sensitivity was explained. Monte Carlo modeling of the x-ray sensitivity is presented in this chapter. In Monte Carlo modeling, carrier trapping or recombination is determined from random numbers. So, the generation of uniform random numbers in [0-1] interval is discussed first followed by the calculation of the position of the generated electron hole pairs in the photoconductor. The sensitivity calculation is started with a simple trap limited model. Then, the effects of recombination, trap fill, nonuniform electric field, x-ray induced trap generation, and detrapping of trapped carrier as discussed in the objectives of this work are included one by one.

4.1 Random Number Generation

A random sequence is a vague notion in which each term is unpredictable and whose digits pass a certain number of traditional statistical tests. All random number generators are based on the theory that has a finite set R and a function, f: $R \rightarrow R'$ which takes elements of R into other elements of R'. For a given initial value (which is called the *seed*) $r \in R$, the generated sequence is

$$r, f(r), f^2(r), f^3(r), \ldots,$$

where $f^2(r)$ means $f(f(r))$, $f^3(r)$ means $f(f(f(r)))$ and so on.

In this work, uniform random numbers are generated using the *subtract with borrow* generator. Instead of using a single integer value, a set of 32 floating point numbers ***r*** in the interval [0-1] are used as the set of seed values. The generation of i^{th} floating point number in the sequence involves a "subtract with borrow" step, where one number in the set of seeds is replaced by the difference of two others, i.e.,

$$r_i = r_{i+20} - r_{i+5} - b \tag{4.1}$$

The three indices i, i+20 and i+5 are reduced residue of 32. The quantity b is determined from the previous step. If the computed r_i is positive, b is set for zero for the next step. But if the computed r_i is negative, it is made positive by adding 1.0 and b is set to a small positive value of 2^{-53}. The 32 floating point numbers are generated from a single initial seed (z_0) by the *multiplicative congruential* method, as

$$z_{k+1} = a z_k \bmod m \tag{4.2}$$

$$r_k = z_k / m \tag{4.3}$$

where a is 16807, m is $(2^{31}-1)$, and k varies from 1 to 32. Here ***z*** is an integer random number vector and ***r*** is floating point random number vector. In order to make the initial seed (z_0) different for each run of the computer program, the time function of the computer is used as the initial seed value. A histogram of generated 10^6 random numbers is shown in figure 4.1.

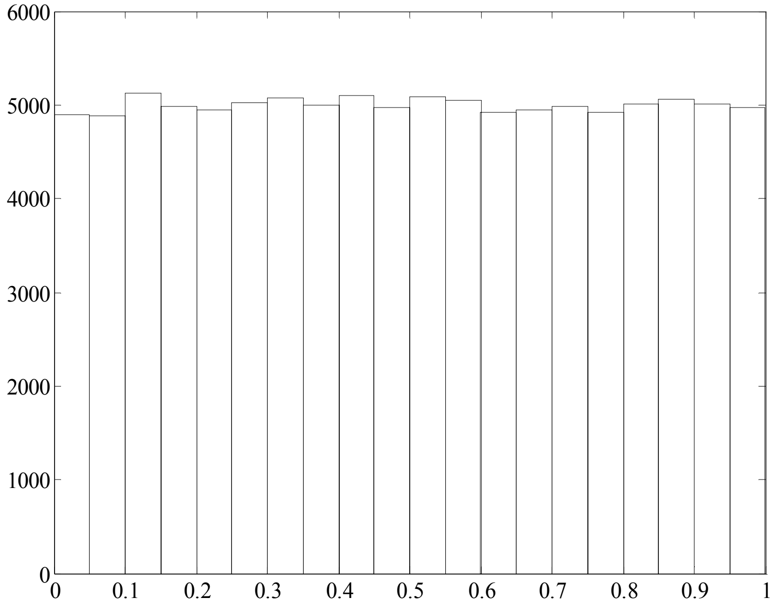

Figure 4.1 A histogram of generated random numbers as discussed in section 4.1

It is shown in the histogram that each bin contains almost 5000 numbers which means that the generated numbers are uniformly distributed between 0 and 1. A brief description of different random number generators is given in appendix A.

4.2 Initial Position of Generated EHPs

The creation of electron hole pairs (EHPs) by an incident x-ray photon first involves the generation of an energetic primary electron by ionizing an inner core shell, as this energetic photoelectron travels in the solids, it causes ionization along its track and hence the creation of many EHPs. As discussed earlier, the generated carrier profile is exponential and is given by Eq. 3.11. Although the overall carrier generation profile is exponential, statistically the x-ray absorption and thus carrier generation process is random. Total generated carriers in the diagnostic exposure range are in the order of 10^{15}. In Monte Carlo calculations, the individual history of each carrier is recorded. For computer simulation, it is not possible to record the individual history of 10^{15} carriers. But the same effect can be manifested with a smaller number of carriers. We assume N number of generated carriers. For higher values of N, the calculation time will be longer. In this work N is in the order of 10^5 to 10^6. Figure 4.2 shows the calculation of the sensitivity using $N = 10^3$ and $N = 10^5$. It is observed from figure 4.2 that when N is 10^3, the fluctuation of the sensitivity around the mean value is greater for different calculations but when N is 10^5; the fluctuation around the mean value is negligible. Thus if the value of N is taken to be 10^5, this value of N is sufficient to produce the accurate result.

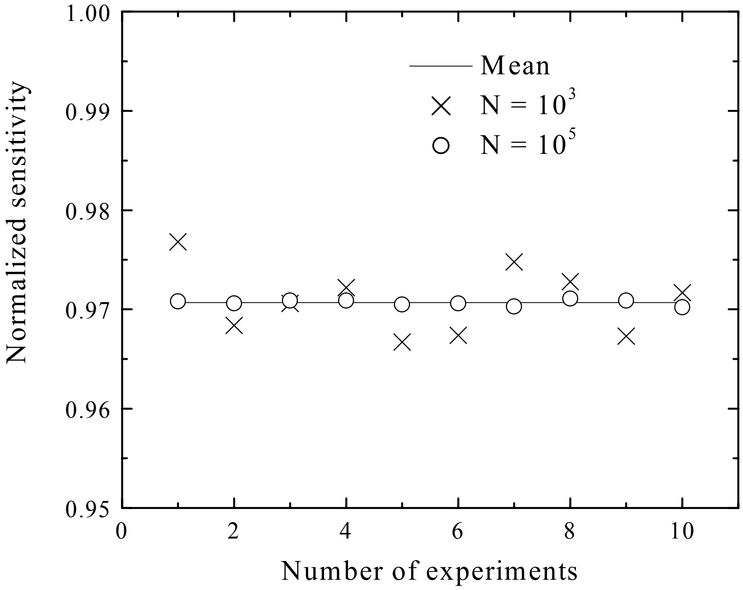

Figure 4.2 Sensitivity calculations with different values of *N*.

4.2.1 Uniform Electric field

For a uniform electric field throughout the photoconductor thickness, $W_{\pm}$ is constant. From Eq. 3.12, the generated carrier profile can be written as

$$c(x) = C_0 e^{-\alpha x} \qquad 4.4$$

Here C_0 is a constant. The *probability density function* (PDF) for the generated carriers at a position *x* in the photoconductor is the ratio of total generated carriers from position 0 (radiation receiving surface) to *x*, to the total number of generated carriers inside the photoconductor (over the whole photoconductor length *L*) as shown in figure 4.3.

$$\text{PDF} = \frac{\int_0^x C_0 e^{-\alpha x} dx}{\int_0^L C_0 e^{-\alpha x} dx}$$

$$\therefore \quad r(1 - e^{-\alpha L}) = 1 - e^{-\alpha x}$$

or $$x = -\frac{1}{\alpha} \ln\left(1 - r \times (1 - e^{-\alpha L})\right). \qquad 4.5$$

Here r is the uniform random number in the interval of [0-1]. Thus, for N number of carriers, the initial position can be calculated by using N uniform random numbers.

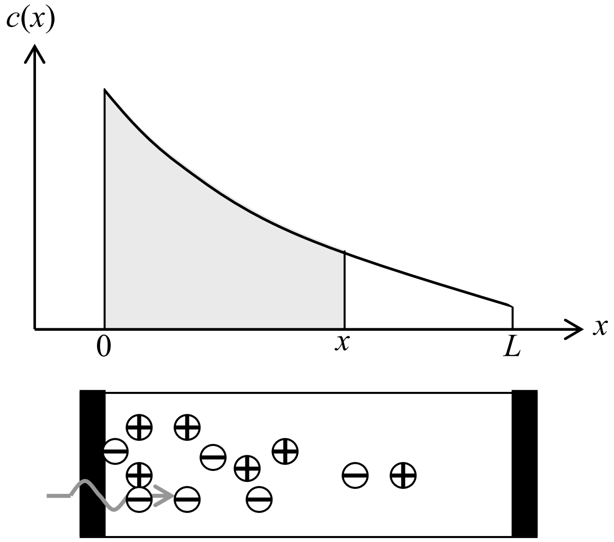

Figure 4.3 Schematic illustrations showing the calculation of the probability density function.

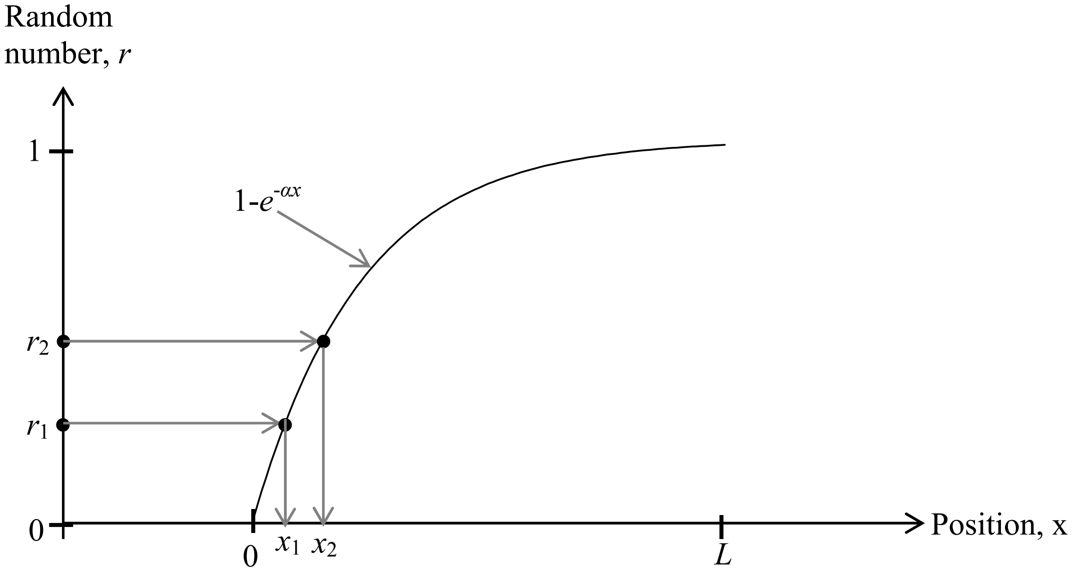

Figure 4.4 Graphical interpretations showing the calculation of the initial position of the generated carriers.

Graphical interpretation of the method used to calculate the initial position was shown in figure 4.4. For any random number r_1 the position of the generated carrier is x_1. For another carrier, the random number is r_2 and the corresponding position is x_2 and so on.

4.2.2 Nonuniform Electric field

For a nonuniform electric field, the calculation of the initial position is slightly complicated. Here, $W_\pm$ is a function of position in the photoconductor thickness via the electric field which now depends on x. Based on the $W_\pm$ versus x profile in the photoconductor, the generated carrier profile can be written as

$$c(x) = \frac{C_1}{W_\pm(x)} e^{-\alpha x} \qquad 4.6$$

Here C_1 is a constant. Hence, the PDF can be written as

$$\text{PDF} = \frac{\int_0^x \frac{1}{W_\pm(x)} e^{-\alpha x} dx}{\int_0^L \frac{1}{W_\pm(x)} e^{-\alpha x} dx}$$

$$\therefore \qquad r\int_0^L \frac{1}{W_\pm(x)} e^{-\alpha x} dx = \int_0^x \frac{1}{W_\pm(x)} e^{-\alpha x} dx \qquad 4.7$$

Equation 4.7 is numerically solved in order to get the initial position x.

4.3 Trap Limited Model

The trap limited model was based on the following assumptions: (i) that the electric field remains uniform throughout the photoconductor thickness over the period of exposure, (ii) that the diffusion of carriers is negligible compared to their drift, (iii) that bimolecular recombination (i.e. carrier recombination between two oppositely drifting carriers) is negligible, (iv) that the x-ray radiation is monoenergetic, and (iv) that the loss of the carriers is only due to deep carrier trapping and the carrier lifetime is characterized by a single trapping time, denoted by τ. At first, the time interval T during which the carriers are drifting inside the photoconductor is divided into some equal small time intervals Δt as shown in figure 4.5.

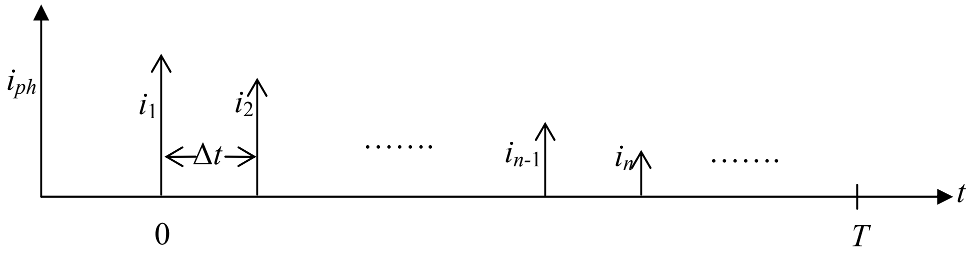

Figure 4.5 Current as a function of time in the x-ray photoconductor.

Our objective is to calculate the current in each time step. Integration of this current will give us the collected charge. The calculation procedure starts with the calculation of the initial position of the x-ray generated carriers. The number of carriers that are generated is calculated by using equation 3.17. The number of generated carriers is of the order of 10^{15} in the clinical exposure range. With the limitation of computer memory and for faster calculations, the calculation proceeds with N carriers, where N is in the order of 10^5 to 10^6. The initial position vectors for N drifting electrons and holes are denoted by $\mathbf{x}_{ie}$ and $\mathbf{x}_{ih}$ respectively. If the carrier deep trapping time is given by τ, then within a time interval time Δt, the trapping probability of the carrier is

$$P_t = 1 - e^{-\frac{\Delta t}{\tau}} . \qquad 4.8$$

If Δt is infinity, the trapping probability of the carrier is unity and when $\Delta t \ll \tau$, the trapping probability is $\Delta t/\tau$.

The bias applied to a photoconductor can be either positive or negative depending on the bias polarity of the top electrode or the radiation receiving electrode. A positive bias implies a positive voltage applied to the radiation receiving electrode. Figure 4.6 shows a positively biased detector, where electrons move towards the left or radiation receiving electrode and holes move towards the right electrode as shown in figure 4.6 with a velocity of μF. Here μ (μ_e for electrons and μ_h for holes) is the drift mobility of the carrier and F is the applied field.

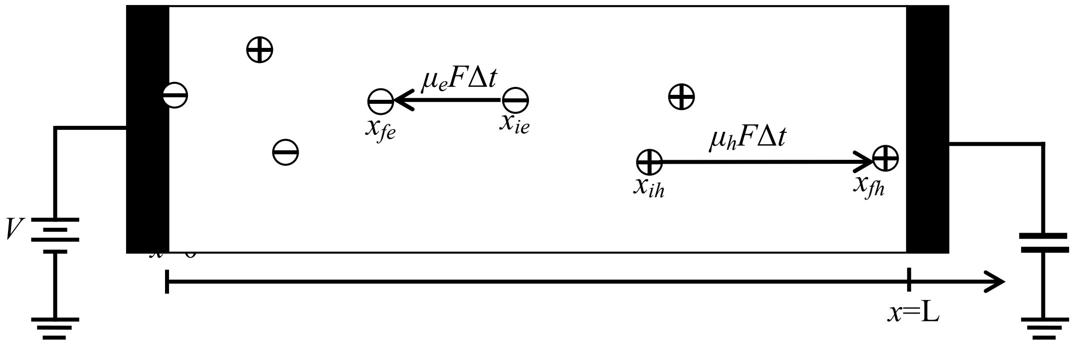

Figure 4.6 Schematic illustration showing the initial position, x_i and final position, x_f for one time step Δt in a positively biased detector.

At time, t=0, all carriers contribute to the current and the current is calculated by equation 3.21. During the next time interval Δt, some carriers will become trapped. The numbers of carriers that get trapped are determined from uniform random numbers. For each carrier, one random number is generated and this number is compared with P_t (equation 4.8). If the random number is less than P_t, it means the carrier is trapped. Once a carrier gets trapped, it is deleted from the history, that is, it is no longer in a transport band. Carriers that survive trapping will move to a new position after the time interval Δt. For holes, the new position vector is $\mathbf{x_{fh}} = x_{ih} + \Delta t\mu_h F$ and for electrons, the new position vector $\mathbf{x_{fe}} = x_{ie} - \Delta t\mu_e F$ as shown in figure 4.6. After time interval Δt, some carriers will leave the photoconductor. The number of carriers that leave the photoconductor are determined from their position x_f. For electrons, the position vector $\mathbf{x_{fe}}$ is compared with 0. Any element in the position vector $\mathbf{x_{fe}}$ less than 0 means that the electron has reached the top (left) electrode. Similarly for holes, any element in the position vector $\mathbf{x_{fh}}$ greater than L means that the hole has reached the bottom electrode. The carriers that leave the photoconductor are also deleted from the history. The position vector $\mathbf{x_f}$ of the present step becomes the initial position vector $\mathbf{x_i}$ for the next step. The remaining carriers inside the photoconductor contribute to the current in the next step. This procedure continues as long as the carriers are drifting inside the photoconductor.

Once the photocurrent (i_{ph}) is calculated as a function of time, the charge collection efficiency (CCE) is calculated as

$$\text{CCE} = \frac{Q_{\text{coll}}}{Q_{\text{gen}}} = \frac{\int_0^T i_{ph}\,dt}{eN}. \qquad 4.9$$

The normalized sensitivity is calculated by the product of CCE and QE, as given by equation 3.18.

4.4 Recombination between Drifting Carriers

X-ray absorption in a photoconductor generates exponentially distributed EHPs inside the photoconductor. The generated electrons and holes drift in opposite directions due to the applied electric field. During this drift, electrons and holes cross each other and may recombine. This type of recombination is known as bimolecular recombination. The recombination rate is proportional to the product of the electron and hole concentrations. So the collected charge would exhibit a square root dependence on the radiated x-ray intensity. Although in most analysis, bimolecular recombination effects are neglected, bimolecular recombination has adverse effects on the charge collection efficiency at higher x-ray fluences.

If R is the bimolecular recombination rate then,

$$R = C_r np, \qquad 4.10$$

where C_r is the recombination coefficient. For a-Se based photoconductors, the recombination process is governed by the *Langevin recombination* mechanism and the recombination coefficient, C_r is close to the Langevin recombination coefficient, C_L

[42]. The Langevin recombination coefficient between drifting electrons and holes is given by

$$C_L = \frac{e(\mu_e + \mu_h)}{\varepsilon_0 \varepsilon_r}. \qquad 4.11$$

where ε_0 is the absolute permittivity and ε_r is the relative permittivity of the photoconductor material. For a-Se photoconductor, ε_r is 6.7.

During the time interval Δt, both species of carriers drift towards their respective electrode by a distance of $\Delta t \times \mu F$ (μ_e for electrons and μ_h for holes). One type of carrier can encounter an opposite carrier within a distance of $\Delta t \times \mu_e F + \Delta t \times \mu_h F$ or $\Delta t \times (\mu_e + \mu_h) F$. As shown in figure 4.7, for a drifting electron N_{1e}, it encounters holes during time interval Δt between x_{1e} and x_{2e}, where x_{1e} is the initial position of the electron and $x_{2e} = x_{1e} - \Delta t \times (\mu_e + \mu_h) F$.

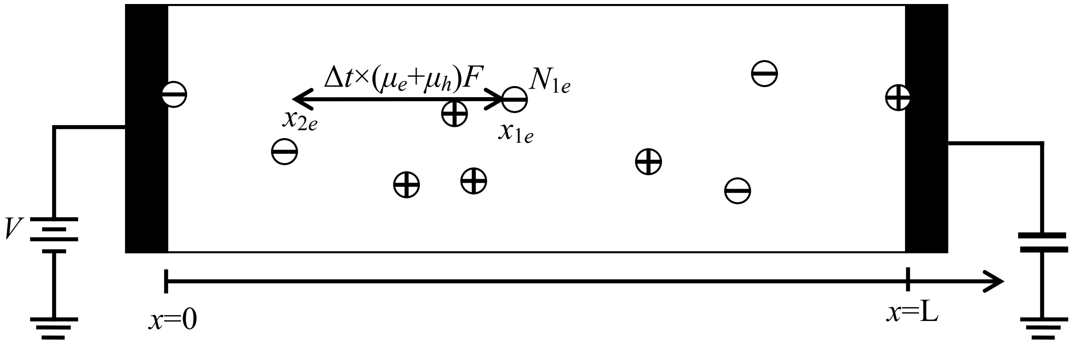

Figure 4.7 Schematic illustration showing positions x_1 and x_2 for bimolecular recombination within time interval Δt.

The probability that a drifting electron N_{1e} will recombine with an oppositely drifting hole within the time interval Δt is

$$P_{re} = 1 - e^{-C_L p \Delta t}. \qquad 4.12$$

Here p is the hole concentration between x_{1e} and x_{2e}. A generated random number in the interval [0-1] less than P_{re} means that the drifting electron recombines with one of the holes, which is also selected randomly between x_{1e} and x_{2e}. If the electron recombines with a hole, both the electron and hole are deleted from the history. Otherwise the electron survives recombination and move to a new position of $x_{1e} - \Delta t \times \mu_e F$. This procedure is carried out for all of the drifting electrons. After a time interval Δt, the new position of the survived holes will be $x_{ih} + \Delta t \times \mu_e F$, where $\boldsymbol{x_{ih}}$ is the initial position vector of the drifting holes. Current and sensitivity calculation are similar, as discussed in section 4.3.

4.5 Recombination between Drifting and Trapped Carriers

A trapped carrier in the photoconductor due to previous exposures acts as a capture center for oppositely charged drifting carriers. This leads to recombination between drifting carriers and trapped carriers [43, 44]. The recombination rate is proportional to the product of the drifting carrier concentration and the oppositely charged trapped carrier concentration. According to Kasap et al. [43], this recombination process also follows Langevin recombination. So, for one species of drifting carriers, the recombination rate is be given by

$$R = C_L c_t^{'} c . \tag{4.13}$$

Here c is the drifting carrier concentration, $c_t^{'}$ is the oppositely charged trapped carrier concentration, and C_L is the Langevin recombination coefficient. If c is the drifting electron concentration then $c_t^{'}$ is the trapped hole concentration and vice versa. Since the drift mobility of electrons and holes are different, Langevin recombination coefficients are not the same for both electrons and holes. For drifting electrons and holes, the Langevin recombination coefficients are C_{Le} and C_{Lh} and respective values are,

$$C_{Le} = \frac{e\mu_e}{\varepsilon_0 \varepsilon_r} \tag{4.14a}$$

$$C_{Lh} = \frac{e\mu_h}{\varepsilon_0 \varepsilon_r} \tag{4.14b}$$

It has been reported that the detrapping times for deep trapped holes and electrons in a-Se are of the order of minutes and several hours respectively [44, 45] which is much longer than the exposure time, or the inter-frame time, or the transit time of the carriers. So the trapped carriers are accumulating inside the photoconductor and trapped carrier concentrations become relatively large after a few exposures. The recombination cross section or Langevin recombination coefficient is higher than the trapping cross section. Because of larger trapped carrier concentration and higher recombination coefficient, the phenomenon of recombination between drifting and trapped carriers can not be neglected in our model. Hence, the carrier transport mechanism is governed by both carrier trapping and recombination assuming that the bimolecular recombination as discussed in section 4.4 is negligible. The carrier trapping probability is given by equation 4.8 and the carrier recombination probability within the time interval Δt is given by

$$P_r = 1 - e^{-C_L c_t^{'} \Delta t}. \qquad 4.15$$

Here $c_t^{'}$ is the oppositely charged trapped carrier concentration between x_1 and x_2. The initial position of the drifting carrier is x_1 and x_2 would be the final position after a time interval Δt. For drifting electrons, $c_t^{'}$ is the trapped hole concentration and C_L is C_{Le} as defined by equation 4.14a. In a positively biased photoconductor, x_1 and x_2 for both drifting electrons and holes are shown in figure 4.8.

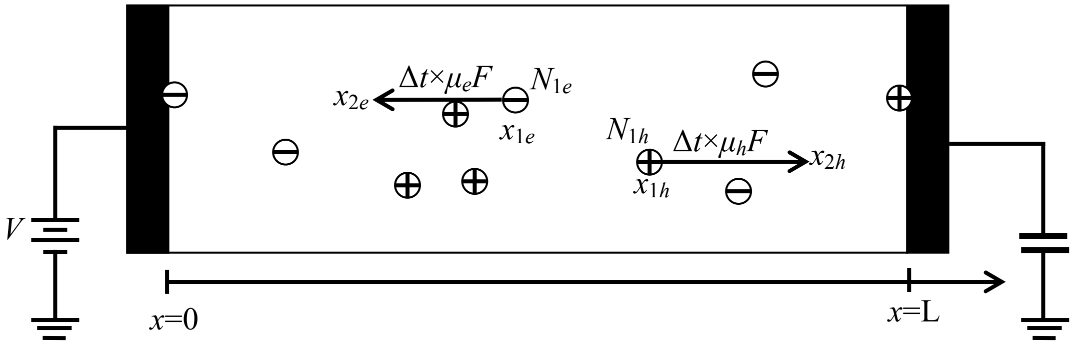

Figure 4.8 Schematic illustration showing positions x_1 and x_2 for carrier trapping and recombination within time interval Δt in a positively biased detector.

Total probability (P) is the summation of the trapping probability (P_t) and the recombination probability (P_r). Thus, for drifting electrons and holes, the total probabilities are

$$P_e = P_{te} + P_{re} = \left(1 - e^{-\frac{\Delta t}{\tau_e}}\right) + \left(1 - e^{-C_{Le} p_t \Delta t}\right) \tag{4.16a}$$

$$P_h = P_{th} + P_{rh} = \left(1 - e^{-\frac{\Delta t}{\tau_h}}\right) + \left(1 - e^{-C_{Lh} n_t \Delta t}\right) \tag{4.16b}$$

The possible destiny of a drifting carrier at position x_1 after a time interval Δt is that it may either be lost between x_1 and x_2 or it can survive and move to position x_2. This is determined from a random number. A generated random number less than the total probability P indicates that the carrier is lost between x_1 and x_2. The carrier can be lost by either trapping or recombination. A second random number is employed to determine how the carrier is lost. A generated random number less than the ratio of trapping probability to total probability (P_t/P) means that the carrier is lost due to trapping; otherwise the carrier is lost due to recombination. If the carrier is lost due to trapping, the position of the carrier is stored as a trapped carrier. If the carrier is lost due to recombination, it must recombine with one of the trapped carriers (opposite polarity) between x_1 and x_2 which is selected randomly and deleted from the history. This procedure is carried out over the entire drifting carriers (both electrons and holes). The number of carriers that leave the photoconductor in each time interval is determined from their position x_2 as described in section 4.3. The remaining calculations of the photocurrent and the sensitivity are similar to the calculations discussed in section 4.3. The block diagram representation of this method is shown in figure 4.9.

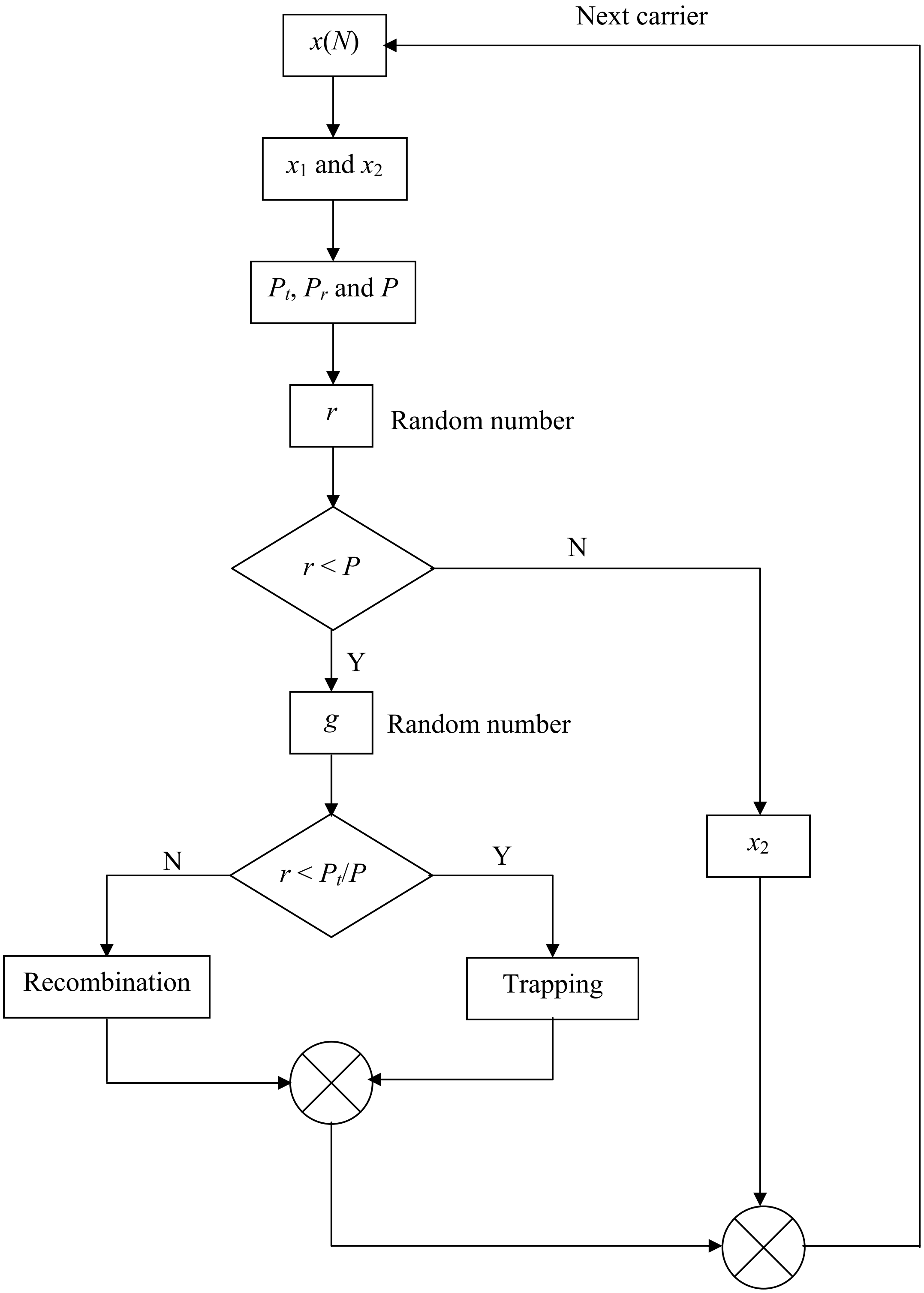

Figure 4.9 Block diagram representation determining carrier trapping and recombination.

4.6 Trap Filling Effects

Carrier trapping time, τ, is defined as the average time the drifting carriers survive before getting trapped in the sea of trap centers. The trapping time is given by

$$\tau = \frac{1}{C_t N_t}. \qquad 4.17$$

where C_t is the capture coefficient and N_t is the deep trap center concentration. Both C_t and N_t depend on the photoconductor material, doping contents, and preparation techniques. As mentioned previously, after a few exposures, the trapped carrier concentration becomes relatively large. As a result, available numbers of deep trap centers to trap next carriers are reduced; the ultimate consequence is the increase of the carrier trapping time. This mechanism is known as the *trap filling effect*. When the trap filling effect is included, the modified carrier trapping time can be given by

$$\tau = \frac{1}{C_t\left(N_t - n_t\right)} = \frac{\tau_0}{1 - n_t / N_t}. \qquad 4.18$$

Here n_t is the trapped carrier concentration and τ_0 is the initial carrier trapping time as defined by equation 4.17. The initial carrier trapping time τ_0, is uniform throughout the photoconductor thickness but the modified carrier trapping time is nonunifrom throughout the photoconductor thickness via n_t as schematically shown in figure 4.10. Deep trap concentration N_t is approximately uniform throughout the photoconductor thickness but the trapped carrier concentration n_t is a function of the photoconductor thickness. Carrier trapping time is inversely proportional to the difference between N_t and n_t. As shown in figure 4.10, at position x=0, both n_t and N_t are same (all traps have been filled), so τ is infinity. This means that no carriers will be trapped at this position, but at position x=L, n_t is zero, hence τ is equal to τ_0.

Taking into account the trap filling effect, the calculation procedure is similar to that discussed in section 4.5, except that instead of using a constant τ, the carrier trapping time, τ for each carrier is calculated using equation 4.18.

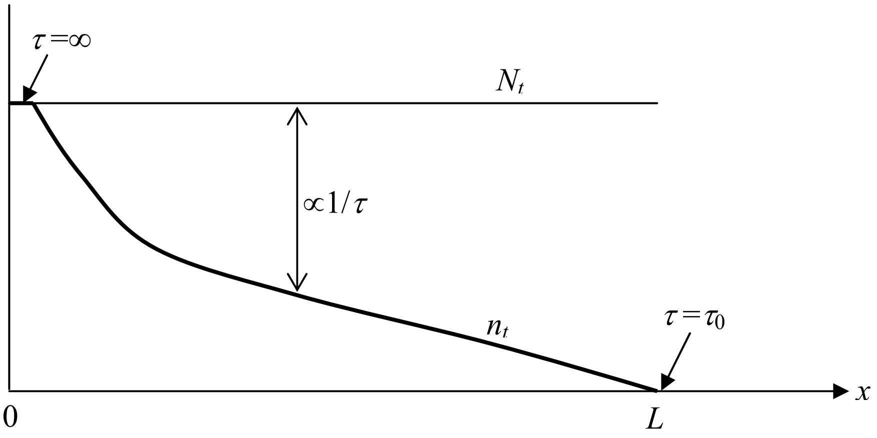

Figure 4.10 Schematic illustration of trap filling effect.

4.7 Nonuniform Electric Field Effects

So far, we have considered only a uniform electric field throughout the photoconductor thickness. We assumed that the trapped charges do not significantly alter the applied field. But in reality, the drifting and trapped carriers inside the photoconductor change the electric field distribution. The electric field distribution inside the photoconductor is calculated by solving Poisson's equation

$$\frac{dF}{dx} = \frac{\rho(x)}{\varepsilon_0 \varepsilon_r}. \qquad 4.19$$

where ε_r is the relative permittivity of the photoconductor material, ε_0 is the permittivity of free space, and $\rho(x)$ is the net charge density inside the photoconductor. The latter is given by

$$\rho(x) = e(p - n + p_t - n_t). \qquad 4.20$$

where p and n are the drifting hole and electron concentrations; p_t and n_t are the trapped hole and electron concentrations. The drifting carrier concentrations are negligible compared to the trapped carrier concentrations, so equation 4.20 can be reduced to

$$\rho(x) = e(p_t - n_t). \qquad 4.21$$

The trapped carrier concentrations p_t and n_t are calculated from the position of the trapped carriers inside the photoconductor.

The boundary condition used to solve equation 4.19 is

$$\int_0^L F dx = V \qquad 4.22$$

where V is the applied bias, for a negatively biased photoconductor V is replaced by $-V$.

Nonuniform applied electric fields have the following effects:

- Nonuniform electric field distribution changes the EHP generation profile (equation 3.12) via $W_{\pm}$. The effect of a nonuniform electric field on the generated carrier positions has already been discussed in section 4.2.2.
- The carrier drifting velocity (μF) is controlled by the applied electric field. Instead of using a constant velocity for each carrier, the carrier velocity is calculated from the electric field the carrier experiences at its position. With the inclusion of a nonuniform electric field effect, the photocurrent is calculated by using equation 3.23.
- The electric field distribution inside the photoconductor plays an important role in the generation of EHPs. Total number of generated carriers depends on the electric field via $W_{\pm}$. Depending on the electric field distribution, the total generated carriers for any exposure may be higher or less than the total number of generated carriers in a uniform electric field. The effect of nonuniform electric field on the generation of EHPs is calculated by the photogeneration ratio (PGR) as discussed in section 3.1.3.

The normalized sensitivity that includes the nonuniform electric field effect is calculated by using equation 3.19. The electric field distribution inside the photoconductor is calculated first. The electric field distribution is used to calculate $W_{\pm}$ (equation 3.14). $W_{\pm}$ leads to the calculation of the initial positions of the generated carriers (equation 4.7) and PGR (equation 3.20). CCE is calculated according to the procedure discussed in section 4.5. Finally normalized sensitivity is calculated by using equation 3.19 i.e. by the product of PGR, CCE, and QE.

4.8 X-ray Induced Effects

The sensitivity reduction or ghosting mechanism arising from the effects of recombination between trapped and drifting carriers, trap fill, and nonuniform electric fields have been recently discussed by Kabir, Yunus, and Kasap [46]. They have found that the change in the electric field distribution inside the photoconductor is significant and the reduction of sensitivity is relatively sharp. After a few exposures, the sensitivity reduction tends to saturate. But the experimental data [17] does not reveal any saturation in the sensitivity reduction.

It has been reported in the literature [45, 47, 48] that light can induce deep trap centers in amorphous chalcogenides. Experimental evidence shows that the enhanced deep trapping depends on the photoconductor material, the irradiation energy, and the total exposure. Deep trapping of both carriers can be increased by an order of magnitudes. But light irradiation has no corresponding effects on the drift mobility of either species of carrier. So there should be no doubt that x-rays can also induce deep trapping inside the a-Se photoconductor and consequently modify the carrier lifetime. The modified carrier lifetime, including x-ray induced deep trap center generation, is given by (from equation 4.18)

$$\tau = \frac{\tau_0}{1 + (N_{Xt} - n_t)/N_t}, \qquad 4.23$$

where N_{Xt} is the concentration of the x-ray induced deep trap centers. The x-ray induced trap center concentration depends on the amount of exposure.

The exact mechanism of photoinduced deep trap center generation has not yet been resolved but it is found that the effect is manifested over a wide range of exposures. Instead of taking a linear relationship of the x-ray induced effect with exposure, the x-ray induced deep trap center generation kinetics is taken to be a first order rate equation so that

$$N_{Xt} = N_{X0}(1 - e^{-X/a}) \qquad 4.24$$

where N_{X0} is the saturation value of the x-ray induced deep trap center concentration, “*a*” is an irradiation energy dependent constant, and X is the amount of exposure. Here N_{X0} depends on the photoconductor material and the x-ray energy. For large values of “*a*”, x-ray induced deep trap center concentration N_{Xt} is proportional to the exposure X over a wide range of exposures.

The sensitivity calculation procedure is similar to that discussed previously except the carrier trapping time for each carrier is calculated by using equation 4.23.

4.9 Detrapping of Trapped Carrier

As mentioned earlier, the average release time of trapped electrons is much longer than the average release time of trapped holes. The reported release times are of the order of minutes and several hours for trapped holes and electrons, respectively. The rest time between successive exposures is of the order of minutes. This means that the rest time between successive exposures is comparable to the average release time of trapped holes. Therefore, an appreciable amount of trapped holes are expected to be released between successive exposures. Since the average release time of trapped electrons is in the order of several hours, there would be no release of trapped electrons between successive exposures.

If the dark rest time between two successive exposures is T_{rest}, the remaining trapped hole concentration p_t for the next exposure can be found from

$$p_t = p_{t0} \times e^{-\frac{T_{rest}}{\tau_{rel}}} \qquad 4.25$$

Here p_{t0} is the trapped hole concentration prior to the rest time and τ_{rel} is the average release time of trapped holes. The sensitivity calculation including detrapping of trapped holes is similar to that discussed in the previous section, except the trapped hole concentration is replaced by equation 4.25 at the beginning of each exposure.

5. Results and Discussion

The Monte Carlo simulation results of the sensitivity for an a-Se photoconductor based detectors are presented in this chapter. The model can also be applied to other photoconductor materials. The simulation results are compared with previous analytical/numerical results and also with experimental data.

Both electron and hole transport mechanisms in stabilized a-Se have been widely studied previously which were discussed in section 2.2.1. The hole and electron drift mobilities in a-Se are assumed to be constant, and the respective values are 0.12 cm^2/V-s and 0.003 cm^2/V-s. These values are used in the calculations in this work. The charge carrier lifetimes may vary substantially among different samples. Typical ranges of the reported lifetimes are between 10-500 μs for holes and 100-1000 μs for electrons. The x-ray attenuation and absorption coefficients for the different materials are obtained from Ref. [49].

5.1 Results for Trap Limited Model

The simulation results based on the theory developed in section 4.3 (i.e., trap limited sensitivity) are presented in this section. Figures 5.1 (a) and (b) show the normalized sensitivity as a function of the photoconductor thickness for mammographic applications. For mammographic applications, the x-ray spectrum is 30 kV_p, which corresponds to mean photon energy of 20 keV. In our calculations, we approximated this x-ray spectrum with a monoenergetic beam of 20 keV.

The applied bias is taken as 10 V/μm, which could be either positive or negative. The positive or negative bias indicates that the radiation receiving electrode is biased positively or negatively. Figure 5.1 (a) shows the simulation results for a positively biased photoconductor with two (high and low) levels of carrier trapping and figure 5.1 (b) shows the simulation results for a negatively biased photoconductor. For high levels of carrier trapping, the hole lifetime is taken as 10 μs and electron lifetime is taken as 100 μs. For low levels of carrier trapping, the corresponding values of hole and electron lifetimes are 50 μs and 1000 μs respectively.

The normalized sensitivity has a critical dependence on the photoconductor thickness. Initially, the sensitivity increases with the photoconductor thickness but after reaching a maximum value, the x-ray sensitivity starts to decrease. Here, the normalized sensitivity is the product of the charge collection efficiency (CCE) and the quantum efficiency (QE) as given by equation 3.18. For a thin photoconductor, the CCE is close to unity as carrier trapping is less in a thin photoconductor but a large amount of incident radiation is obviously not absorbed; that is, the QE is less than unity. The QE increases with the photoconductor thickness and hence the sensitivity increases with the thickness. But for thickness greater than the optimal photoconductor thickness, where QE is close to unity, the sensitivity starts to decrease due to carrier trapping. With increasing photoconductor thickness, more carriers get trapped; as a result, the CCE decreases and consequently the sensitivity starts to decrease with increasing thickness. The sensitivity versus thickness in figure 5.1 implies that the sensitivity is controlled by the QE in a thin photoconductor and in a thick photoconductor it is controlled by the CCE. Therefore, there is an optimum photoconductor length that compromises between higher absorption and less trapping. From figure 5.1, it can be concluded that the optimum thickness of an a-Se photoconductor for mammographic applications is close to 200 μm where the QE is around 0.99. Again, at higher carrier trapping levels, more carriers get trapped and hence the sensitivity is lower than that of lower carrier trapping levels.

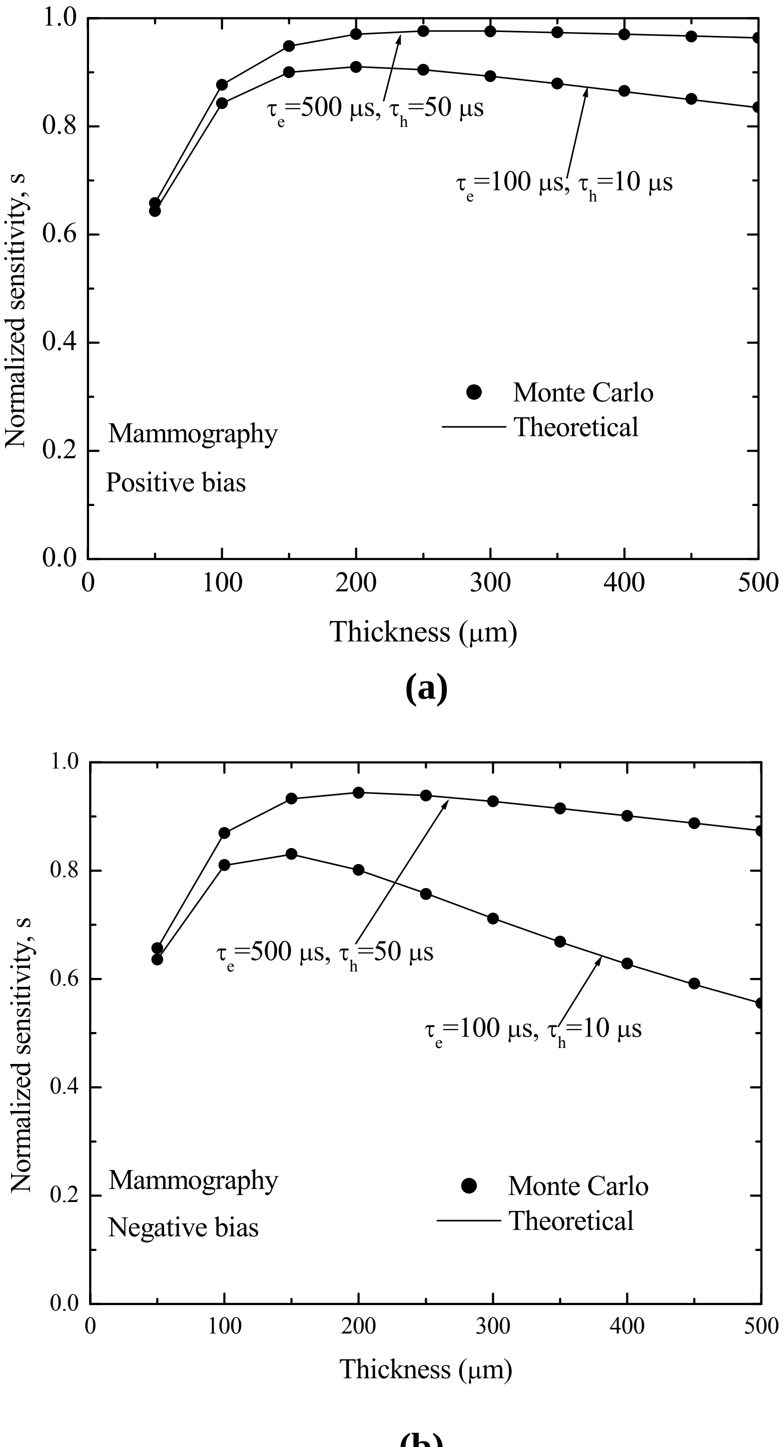

Figure 5.1 The normalized sensitivity of mammographic detectors as a function of photoconductor thickness. (a) Positively biased detectors and (b) negatively biased detectors.

Our simulation results show excellent agreement with the analytical model reported in Ref. [20]**.** The solid lines indicate the theoretical results and the solid circles are the results from our Monte Carlo simulation.

The normalized sensitivity of chest radiographic detectors as a function of the photoconductor thickness is shown in figure 5.2. The solid line shows the simulation results for a positively biased detector and the dashed line show the simulation results for a negatively biased detector. For chest radiographic applications, the x-ray spectrum is 120 kV_p which corresponds to mean photon energy of 60 keV. The carrier lifetimes are 500 μs and 50 μs for electrons and holes, respectively. The applied electric field is 10 V/μm. Again, the normalized sensitivity has a critical dependence on the photoconductor thickness. Initially, the sensitivity increases with the photoconductor thickness due to an increase in QE. But for thicknesses greater than the optimal photoconductor thickness, the x-ray sensitivity starts to decrease due to the decrease of the CCE.

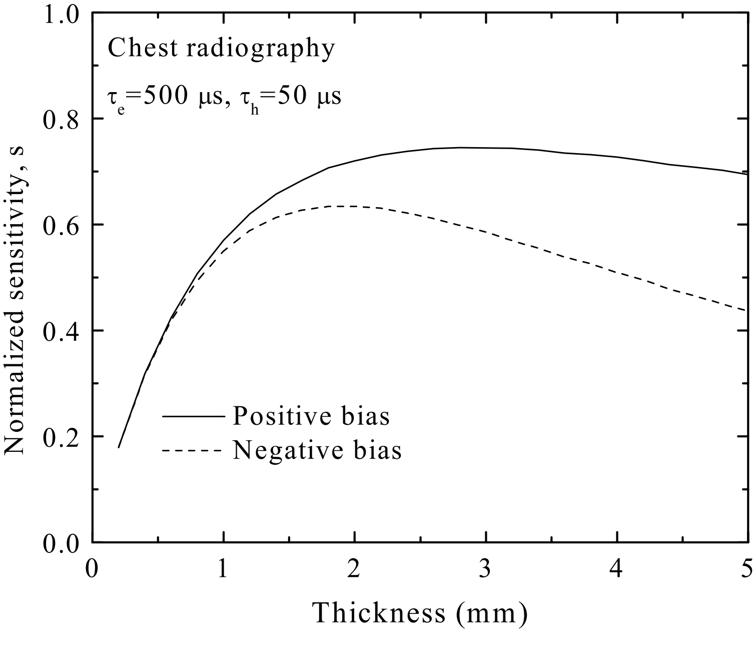

Figure 5.2 The normalized sensitivity of chest radiographic detectors as a function of photoconductor thickness for both positive and negative biasing.

For chest radiographic detectors, the optimal thickness for an a-Se photoconductor is seen to be around 1500 μm where the QE is 0.78. Thus, at optimum operating condition, QE is close to unity for mammographic detectors but for chest radiographic detectors, QE is close to 0.78. Lower value of QE in chest radiographic detectors indicates that the CCE decreases significantly due to carrier trapping in chest radiographic detectors with increasing photoconductor thickness. This means that the compromise between the QE and the CCE is more pronounced in chest radiographic detectors.

Although, from figures 5.1 and 5.2, one senses that the x-ray sensitivity in a positively biased detector is higher than that of a negatively biased detector, in reality it depends on the $\mu\tau$ product of the carriers for a particular photoconductor. For an a-Se photoconductor, the mobility μ is constant for both electrons and holes but the carrier trapping time τ varies widely from sample to sample. Figure 5.3 (a) shows the normalized sensitivity as a function of the $\mu\tau$ product of electrons ($\mu_e\tau_e$) for both positive and negative biasing. Figure 5.3 (b) shows the normalized sensitivity as a function of $\mu\tau$ product of holes ($\mu_h\tau_h$) for both positive and negative biasing. The photoconductor thickness was taken to be 200 μm for mammographic applications and the applied electric field was 10 V/μm.

It is shown in figure 5.3 (a) that the sensitivity is almost constant with $\mu_e\tau_e$ for a positively biased detector but for a negatively biased detector, the sensitivity increases with $\mu_e\tau_e$ and at one stage the sensitivity of a negatively biased detector is higher than that of a positively biased detector. Same scenario also appears in figure 5.3 (b). The sensitivity of a negatively biased detector is almost constant with $\mu_h\tau_h$ but the sensitivity of a positively biased detector increases with $\mu_h\tau_h$ and becomes higher than that of a negatively biased detector. So, it is apparent from figures 5.3, that in a positively biased detector, the sensitivity primarily depends on the mobility lifetime product of holes ($\mu_h\tau_h$); while in a negatively biased detector, the sensitivity mostly depends on the mobility lifetime product of electrons ($\mu_e\tau_e$).

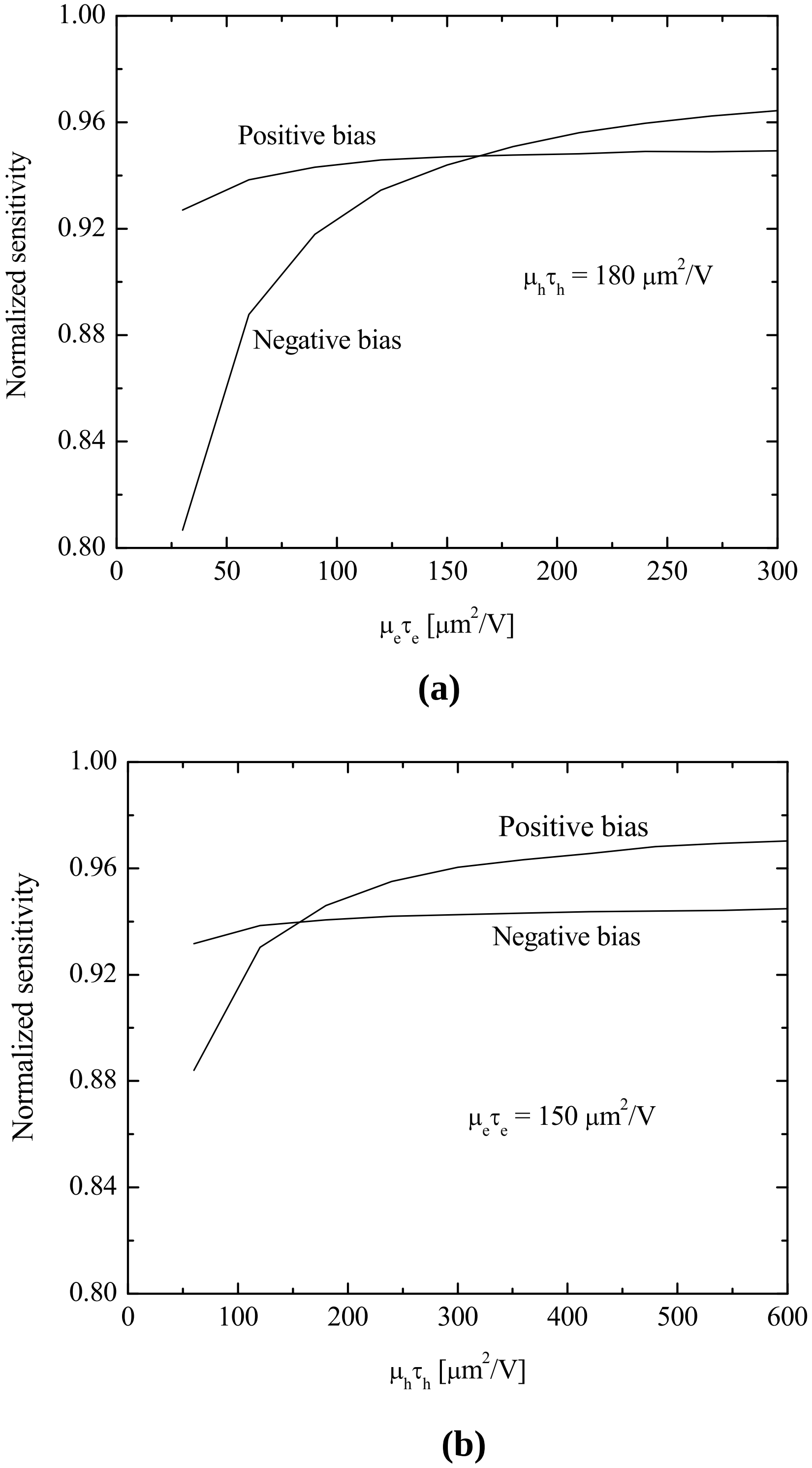

Figure 5.3 The normalized sensitivity versus mobility lifetime product for both positive and negative biasing. Mobility lifetime product of electrons (a) and holes (b).

The number of carriers that will be trapped during transport depends on the mobility lifetime product ($\mu\tau$), the length of the detector (L) that carriers drift, and the applied electric field (F). For a constant applied electric field, the greater the value of the $\mu\tau$ product, the fewer carriers will be trapped. Due to exponential absorption, most electron hole pairs (EHPs) are generated near the radiation receiving electrode or top electrode. Carriers drifting towards the bottom electrode have to drift a longer distance and have a higher probability of getting trapped than those drifting towards the top electrode. It implies that the carriers drifting towards the bottom electrode control the sensitivity of the photoconductor.

For a positively biased detector, holes drift towards the bottom electrode and electrons drift towards the top electrode and vice versa for a negatively biased detector. Hence the hole transport governs the sensitivity of a positively biased detector while electron transport governs the sensitivity of a negatively biased detector. It can be concluded that the biasing preference of a photoconductor should depend on the $\mu\tau$ product of the carriers. If a photoconductor has a higher $\mu\tau$ product of holes than that of electrons, positive biasing will give a better sensitivity. Similarly, the sensitivity will be better for a negatively biased detector if the photoconductor has a better $\mu\tau$ product of electrons than that of holes.

5.2 Results for Bimolecular Recombination

Bimolecular recombination (i.e., recombination between oppositely charged drifting carriers) is proportional to the product of the drifting electron and hole concentrations. The drifting carrier concentrations depend on the exposure rate. Figure 5.4 shows the charge collection efficiency (CCE) of an a-Se photoconductor as a function of the exposure rate considering only bimolecular recombination. The detector is considered for mammographic applications with a photoconductor thickness of 200 μm, an applied electric field of 10 V/μm, and x-ray energy of 20 keV. The crosses represent the simulation results for a positively biased detector while the open circles are the simulation results for a negatively biased detector. From figure 5.4, it is observed that CCE is unity for an exposure rate up to 100 R/s and drops sharply for exposure rates above 1000 R/s and approaches to zero at higher exposure rates.

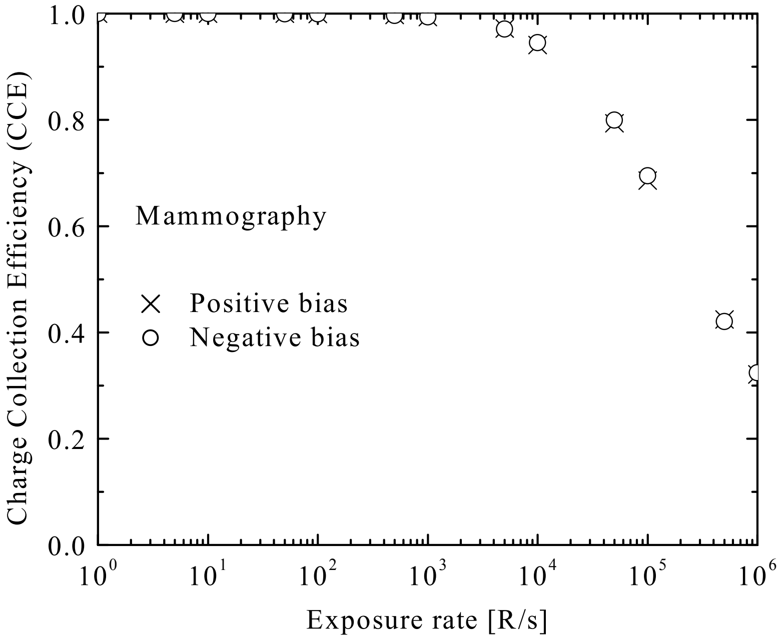

Figure 5.4 The charge collection efficiency of mammographic detectors as a function of exposure rate. Bimolecular recombination is considered only.

The normal exposure rate is of the order of 0.1 R/s, but figure 5.4 shows that bimolecular recombination is effective for exposure rates above 100 R/s, which is a thousand times greater than typical exposure rates used in clinical applications. Therefore, it can be concluded that bimolecular recombination is insignificant at low exposure rates but it has a severe effect on the CCE at high exposure rates (over 100 R/s). Again, from figure 5.4, it is observed that for a uniform electric field, bimolecular recombination is independent of the bias polarity as two curves (crosses and open circles) overlap each other. Since bimolecular recombination depends on the concentration of both types of carrier, hence the overall loss is the same in either bias condition. Thus, charge collection efficiency is independent of bias polarity.

The effect of bimolecular recombination on CCE for mammographic and chest radiographic detectors as a function of the total carrier generation rate is shown in figure 5.5. The detector thickness and the x-ray energy are 200 μm and 20 keV, respectively, for mammographic applications. The detector thickness and the x-ray energy are 1000 μm and 60 keV respectively for chest radiographic applications. Thus, the normalized absorption depths ($1/\alpha L$), Δ are 0.23 and 0.98 for mammographic and chest radiographic detectors, respectively. In both cases, the applied electric field is 10 V/μm. From figure 5.5, it is clear that the bimolecular recombination effect is more pronounced in chest radiographic detectors. Chest radiographic detectors are thicker than mammographic detectors; hence, the carrier transit time in a chest radiographic detector is longer than that it is in a mammographic detector. Due to the longer transit time, carriers get sufficient time to recombine in a chest radiographic detector. The bimolecular recombination effect is more pronounced in chest radiographic detectors, and thus, the CCE is less in these detectors.

The effect of bimolecular recombination on the CCE for different electric fields is shown in figure 5.6. Again, the detector that is considered is for a mammographic application.

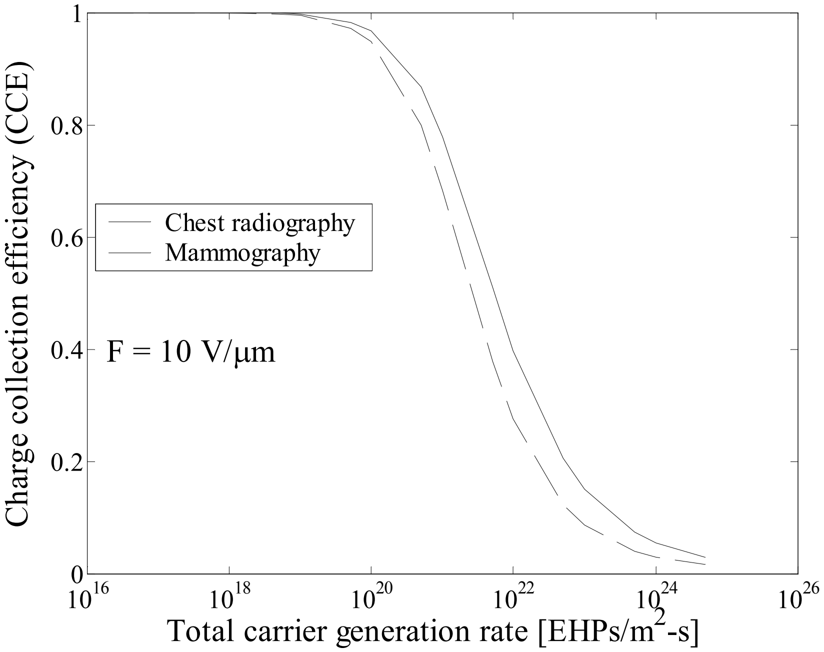

Figure 5.5 The charge collection efficiency as a function of total carrier generation rate for mammographic and chest radiographic detectors.

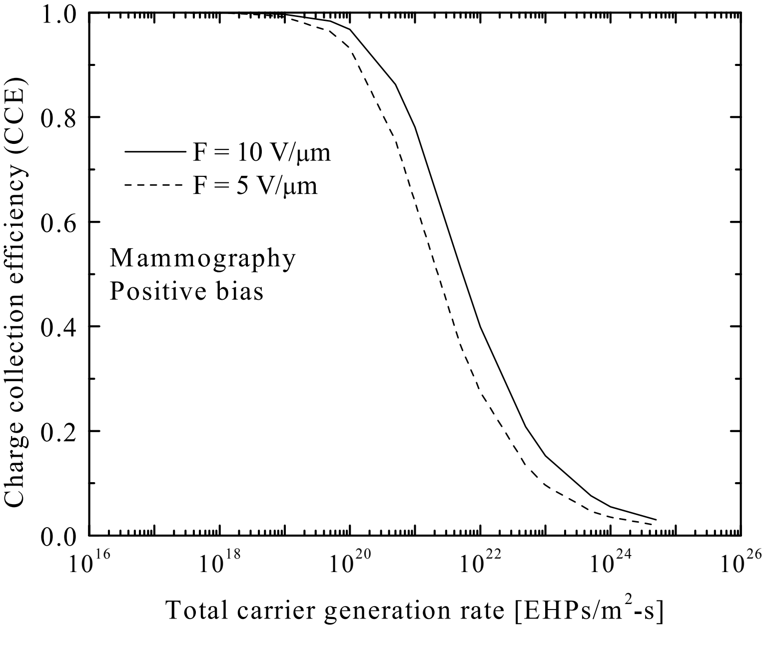

Figure 5.6 The charge collection efficiency as a function of total carrier generation rate for different electric fields.

The solid line indicates the simulation results for an applied electric field of 10 V/μm and the dashed line indicates the simulation results for an applied electric field of 5 V/μm. At a lower electric fields, the carrier drift velocity is low and hence the carriers stay a longer time inside the photoconductor. This implies that the carriers get more time to recombine. Thus, the bimolecular recombination effect is more pronounced, and hence the CCE is less at lower fields.

5.3 Results for Ghosting

Ghosting refers to the residual image left over on the photoconductor due to previous exposures. Change of sensitivity is a measure of ghosting. In this section, Monte Carlo simulation results of ghosting will be presented and discussed.

5.3.1 Effect of Recombination

Recombination of drifting carriers with trapped carriers of the previous exposure is considered to be the leading source of ghosting. Figures 5.7 and 5.8 show the normalized sensitivity as a function of the cumulative exposure for different medical applications and biasing conditions. Figure 5.7 (a) is for a positively biased mammographic detector and figure 5.7 (b) is for a negatively biased mammographic detector. Figure 5.8 (a) is for a positively biased chest radiographic detector and figure 5.8 (b) is for a negatively biased chest radiographic detector. For all cases, the applied electric field is 10 V/μm, which is the standard applied field for an a-Se photoconductor. The normalized x-ray sensitivity decreases with increasing cumulative exposure and eventually reaches a saturation level. The sensitivity reduction, or ghosting, occurs due to the loss of drifting carriers recombining with oppositely charged trapped carriers. This type of recombination depends on the trapped carrier concentration.

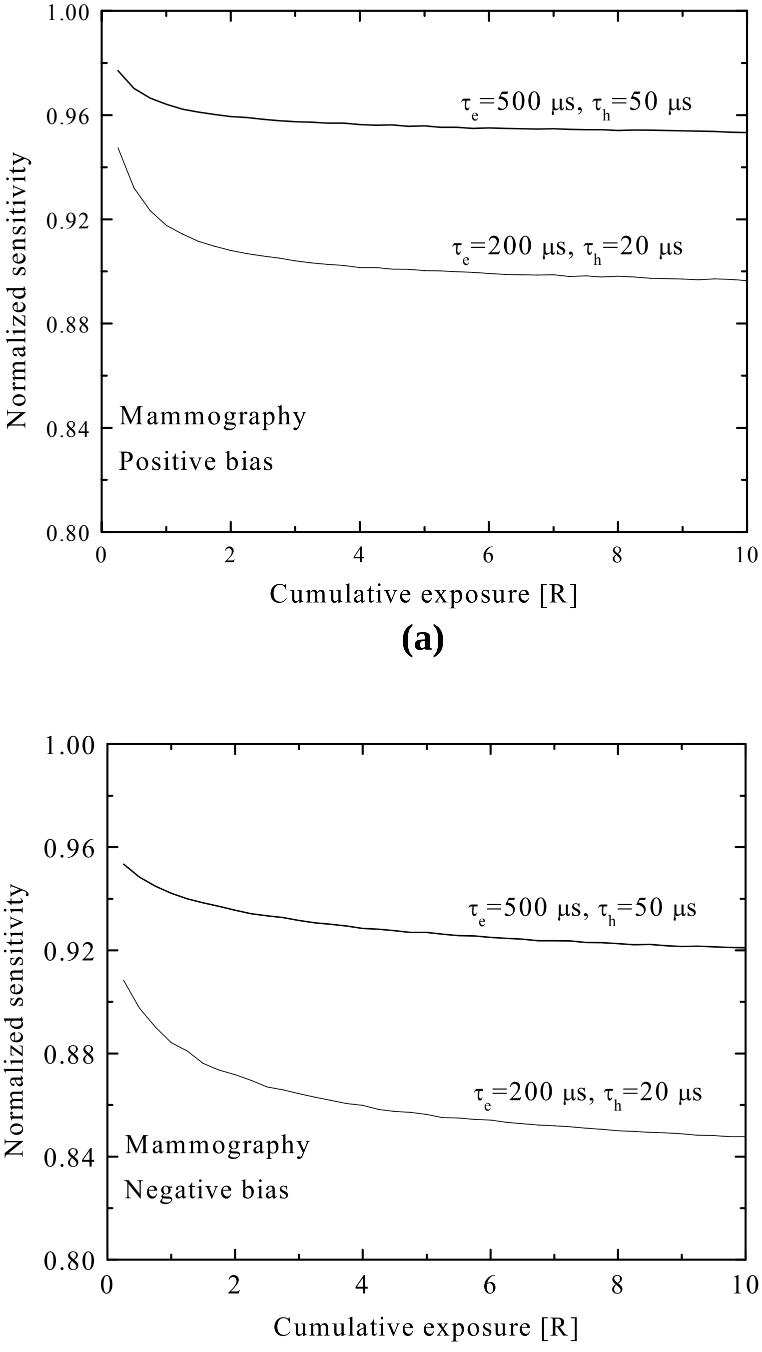

Figure 5.7 The normalized sensitivity versus cumulative x-ray exposure for mammographic applications. (a) Positively biased detectors and (b) negatively biased detectors.

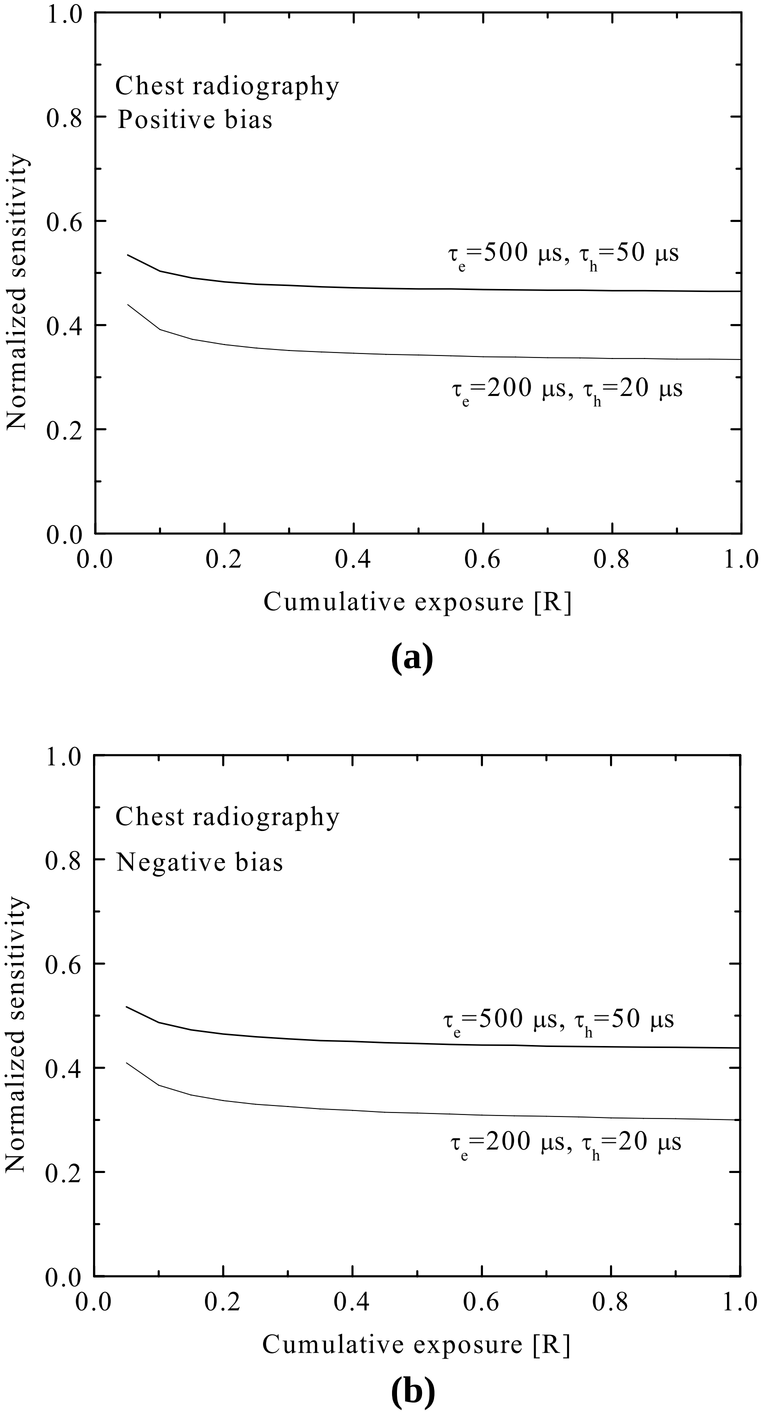

(a)

(b)

Figure 5.8 The normalized sensitivity versus cumulative x-ray exposure for chest radiographic applications. (a) Positively biased detectors and (b) negatively biased detectors.

Although carrier trapping is independent of exposure, the trapped carrier concentration does not increase linearly with exposure. The greater the trapped carrier concentration, the greater the loss of trapped carriers recombine with drifting carriers. Therefore, the trapped carrier concentration reaches a steady state level due to the balance between two processes: the rate at which new carriers are being trapped and the rate at which trapped carriers are lost due to recombination. It should be emphasized that the electric field is taken to be uniform and the trap filling effect is neglected. The electron hole pair creation energy, $W_{\pm}$, is taken as uniform across the sample. Once the trapped carrier concentration reaches a steady state level, the loss of drifting carriers recombining with trapped carriers saturates, and hence, the sensitivity reduction also saturates, which is observed in figures 5.7 and 5.8.

In order to examine the effects of biasing or carrier trapping level on ghosting, the *relative* sensitivity instead of *normalized* sensitivity is calculated as a function of the cumulative x-ray exposure, as shown in figures 5.9 and 5.10 for the cases in figures 5.7 and 5.8, respectively. Relative sensitivity is defined as the ratio of the sensitivity of a subsequent exposure to the sensitivity of the first exposure. As expected, the sensitivity reduction is greater at high trapping levels ($\tau_e = 200$ μs, $\tau_h = 20$ μs) than at low trapping levels ($\tau_e = 500$ μs, $\tau_h = 50$ μs). At high trapping levels more carriers are trapped. The recombination effect is more pronounced and the sensitivity reduction is greater at high trapping levels. The effect of biasing on ghosting is seen to depend on the $\mu\tau$ product of the carriers. From figures 5.9 and 5.10, it is seen that the sensitivity reduction is greater in the negatively biased detector. In this calculation, the mobility lifetime products of the electrons are 1.5×10^{-6} cm^2/V and 0.6×10^{-6} cm^2/V for low level of trapping and high level of trapping respectively. The respective values of the mobility lifetime products of holes are 6×10^{-6} cm^2/V and 2.4×10^{-6}. This means that the mobility lifetime product of electrons is taken to be four times less than that of holes. As discussed previously, electrons primarily get trapped in a negatively biased detector and holes primarily get trapped in a positively biased detector. So, more electrons get trapped in a negatively biased detector than that of holes in a positively biased detector, the recombination effect is more pronounced and hence the sensitivity reduction is higher in a negatively

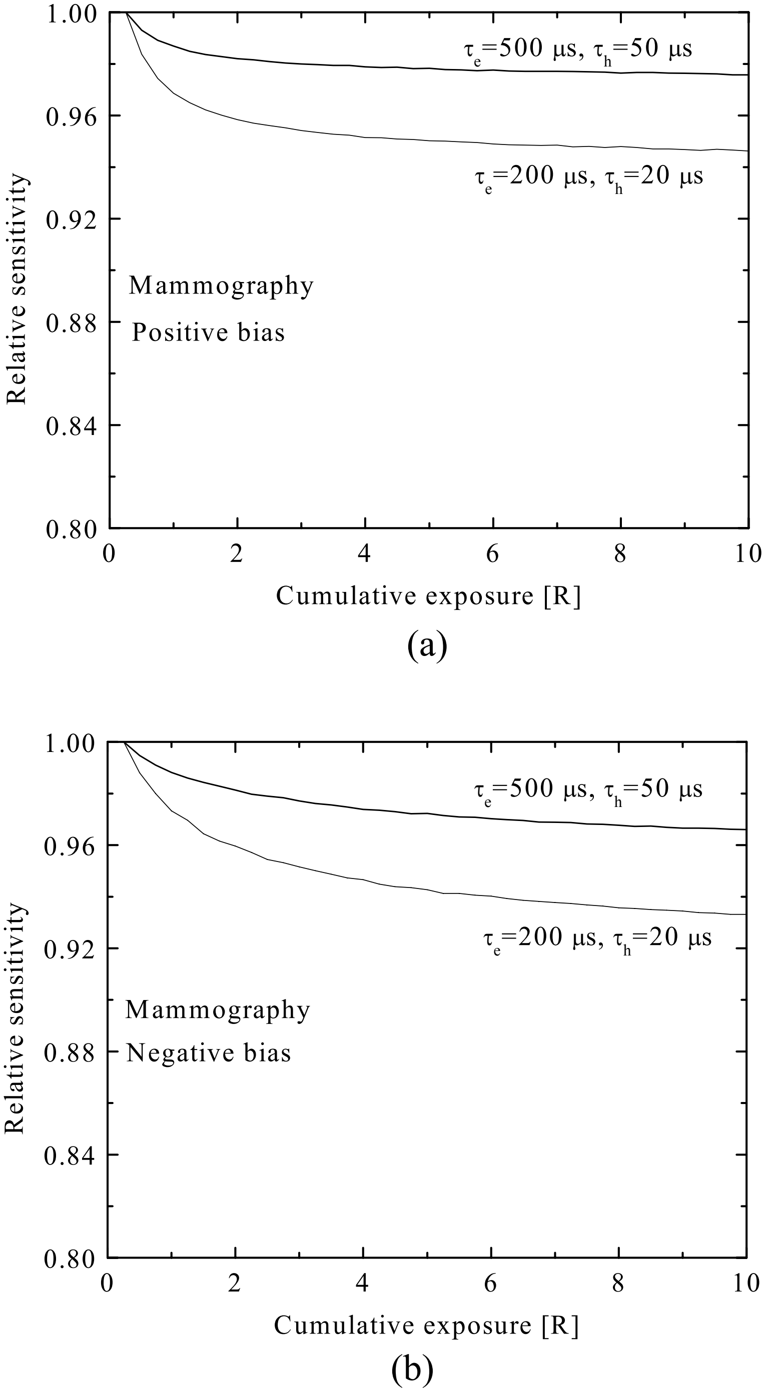

Figure 5.9 The relative sensitivity versus cumulative x-ray exposure for mammographic applications. (a) Positively biased detectors and (b) negatively biased detectors.

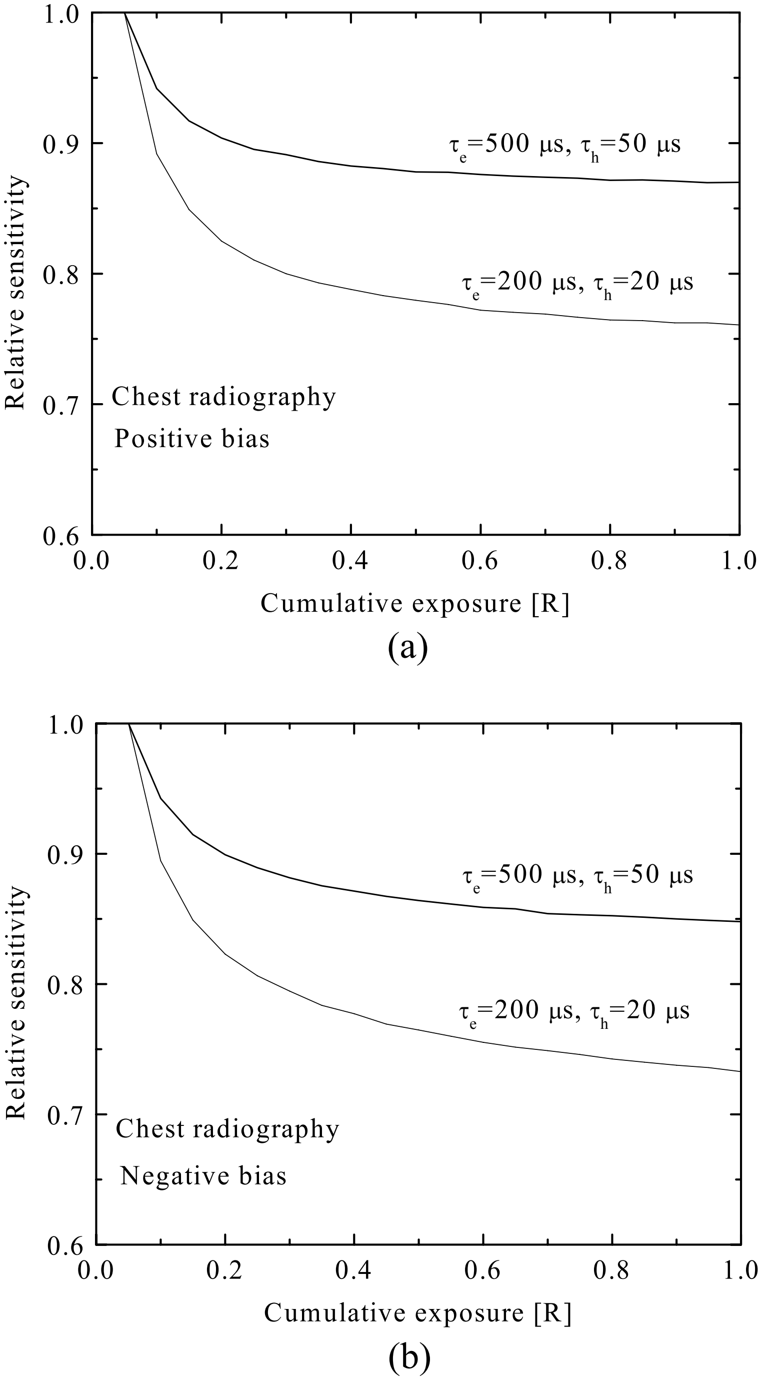

Figure 5.10 The relative sensitivity versus cumulative x-ray exposure for chest radiographic applications. (a) Positively biased detectors and (b) negatively biased detectors.

biased detector. Therefore, the ghosting depends on biasing via the mobility lifetime product of the carriers. If the mobility lifetime product of holes is greater than that of electrons, ghosting will be less pronounced in the positive biased detector. Ghosting will be less pronounced in a negatively biased detector if the mobility lifetime product of electrons is greater than that of holes.

Again, ghosting is more pronounced in chest radiographic detectors than in mammographic detectors even at a lower level of cumulative exposure. Chest radiographic detectors are much thicker than mammographic detectors. For thicker detectors, carrier transit times are longer. This longer transit time has the following effects: (i) carrier trapping is higher and hence the trapped carrier concentration is greater (ii) carriers get sufficient time for recombination. Both these factors help to increase the recombination rate simultaneously in chest radiographic detectors. Hence the sensitivity reduction is sharp and sudden in chest radiographic detectors.

5.3.2 Trap Filling Effects

Figures 5.11 (a) and (b) show the trapped carrier (both electrons and holes) concentrations after one roentgen exposure, for both positively and negatively biased detectors, respectively. The detector is considered for mammographic applications. The carrier lifetimes are 500 μs for electrons and 50 μs for holes. From figures 5.11, it is observed that the trapped carrier concentration is nonuniform across the photoconductor thickness and that the trapped carrier concentrations are of the order of 10^{13} /cm^3. For a positively biased detector, the trapped hole concentration is less near the radiation receiving (or the top electrode) and gradually increases towards the bottom electrode, while the trapped electron concentration is highest near the top electrode and less towards the bottom electrode. Most EHPs are generated near the top electrode. For a positively biased detector, electrons move towards the top electrode and holes move towards the bottom electrode. Therefore, fewer electrons are trapped near the bottom electrode.

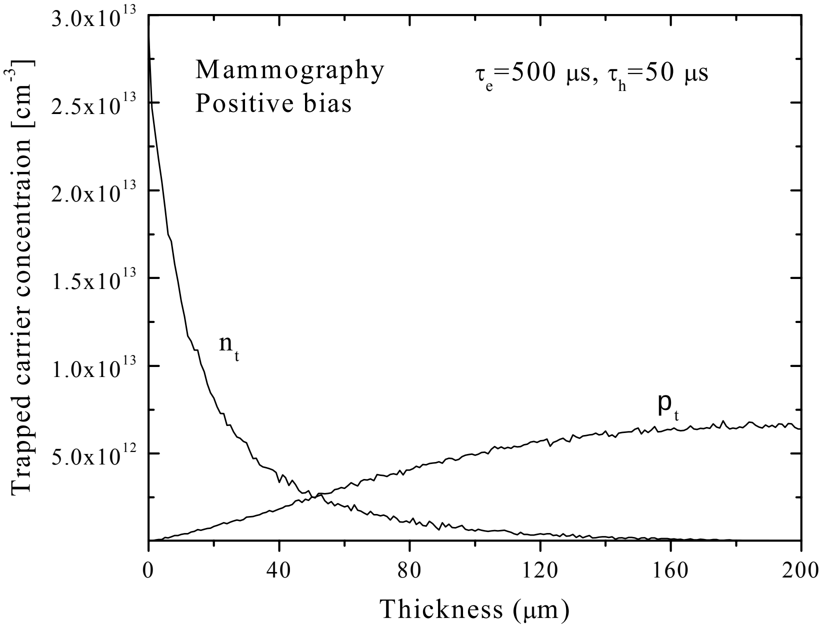

(a)

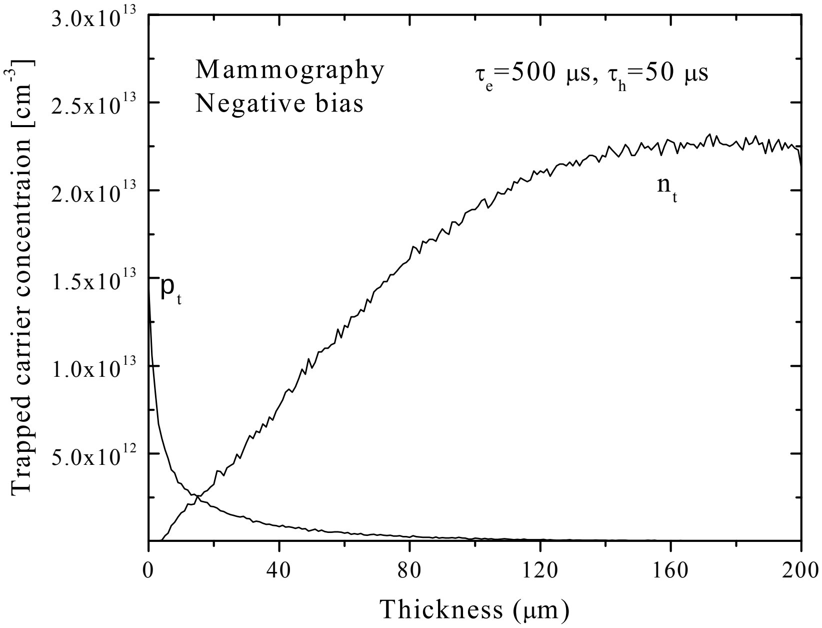

(b)

Figure 5.11 Trapped carrier concentrations inside the photoconductor after one R exposure for mammographic applications. (a) Positively biased detectors and (b) negatively biased detectors.

Since holes drift towards the bottom electrode, hole trapping occurs throughout the photoconductor. The trapped holes near the top electrode recombine with the drifting electrons. Therefore, the trapped hole concentration is less near the top electrode and higher near the bottom electrode. The same explanation is applicable to a negatively biased detector. Although the exact deep trap center concentration in a-Se is not well established, the reported deep trap center concentration is of the order of 10^{13} /cm^3, i.e., trapped carrier concentrations are comparable with deep trap center concentrations. Hence, trap filling effects cannot be neglected and must play an important role in the calculation of x-ray sensitivity.

Trap filling effects on ghosting are shown in figures 5.12 (a) and (b) for a positively and negatively biased mammographic detector, respectively. The solid line shows the results from considering the trap filling effects while the dashed lines show the results without considering such effects. It is observed that when trap filling effects are taken into account, the ghosting is reduced.

Trap filling effects increase the carrier lifetime, and consequently, fewer carriers get trapped in successive exposures. Trap filling effects tend to increase the sensitivity, while the recombination effects tend to decrease the sensitivity. Depending on the trapped carrier concentration and the deep trap center concentration, the overall effect can be either positive or negative. As observed in figures 5.12, the overall effect is negative. But trap filling effects are more evident in a negatively biased detector. Since the mobility lifetime product of electrons is lower, more carriers (especially electrons) get trapped in negatively biased detectors, and hence the trap filling effects are more prominent in negatively biased detectors. Again, trap filling effects are found to depend on the deep trap center concentration, N_t. Two levels of deep trap center concentrations 5×10^{13}/cm^3 and 2×10^{13}/cm^3 are considered in the calculations. As is observed from figures 5.12, when deep trap center concentrations are taken to be small, the effects of trap filling are more pronounced.

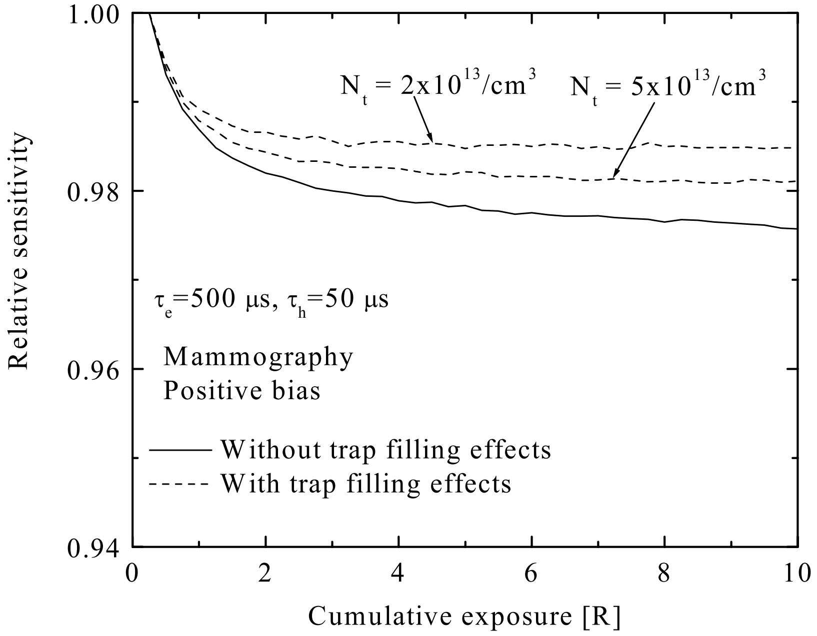

(a)

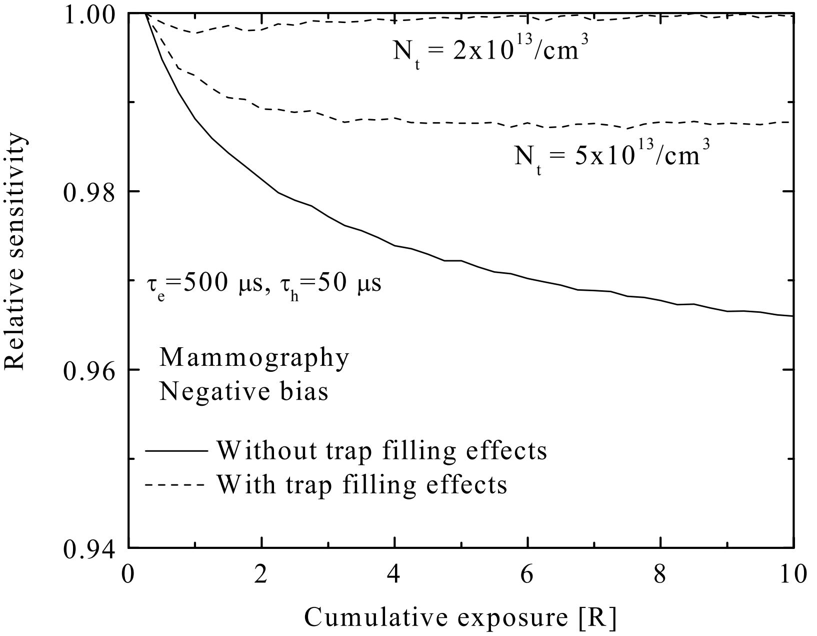

(b)

Figure 5.12 Trap filling effects on the relative sensitivity for mammographic applications. (a) Positively biased detectors and (b) negatively biased detectors.

5.3.3 Nonuniform Electric Field Effects

As shown in figures 5.11, the trapped carrier concentrations are of the order of 10^{13} /cm^3 and the distribution of trapped holes and electrons are not uniform inside the photoconductor. These large amounts of nonuniformly distributed trapped carriers alters the electric field distribution inside the photoconductor, changing the EHP creation energy $W_{\pm}$, and hence modifying the carrier generation in subsequent exposures. The effects of a nonuniform electric field on the sensitivity are shown in figures 5.13 and 5.14 for mammographic and chest radiographic detectors respectively under positive and negative biasing conditions.

Carrier lifetimes are 500 μs for electrons and 100 μs for holes (i.e. the $\mu\tau$ product of the holes taken is 8 times higher than that of the electrons). Deep trap center concentrations were taken to be 5×10^{13} /cm^3 for both the electrons and the holes. The solid lines are the simulation results considering the effects of a nonuniform electric field while the dashed lines are the simulation results considering a uniform electric field. Nonuniform electric field effects have been found to depend on biasing conditions and the type of medical application.

Nonuniform electric field effects are not same for both positive and negative biasing conditions. It is observed that for both mammographic and chest radiographic detectors with negative biasing, ghosting increases when nonuniform electric field effects are considered. The effect of nonuniform electric field effects are opposite in positively biased mammographic and chest radiographic detectors. While nonuniform electric field effects increase ghosting in positively biased mammographic detectors, the effects have been found to decrease ghosting in positively biased chest radiographic detectors. Again the effects are more pronounced in the negatively biased mammographic detectors. For example, as apparent from figure 5.13 (b), the change in ghosting due to a nonuniform electric field is 18% in the negatively biased mammographic detectors.

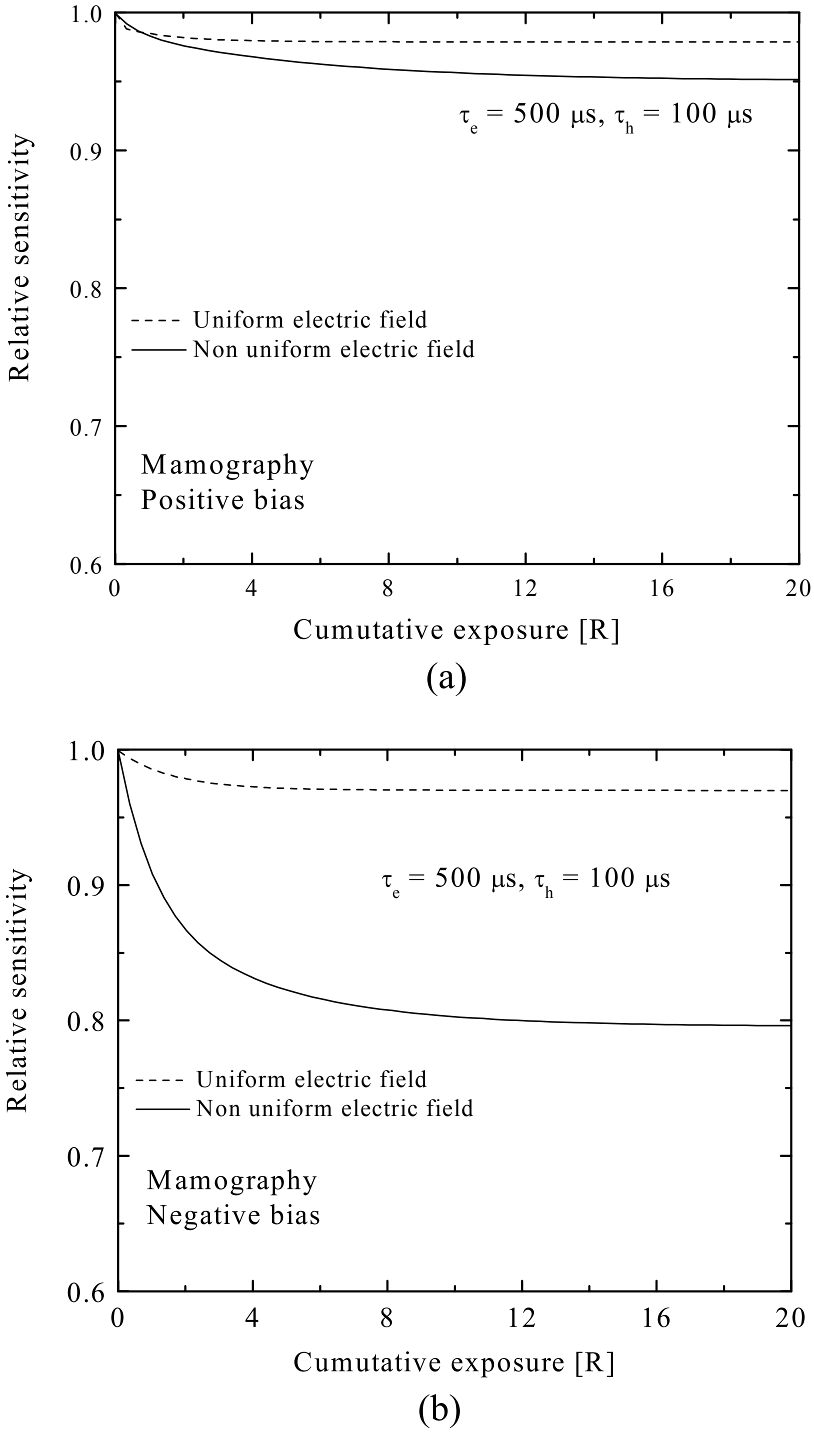

Figure 5.13 Nonuniform electric field effects on the relative sensitivity for mammographic applications. (a) Positively biased detectors and (b) negatively biased detectors.

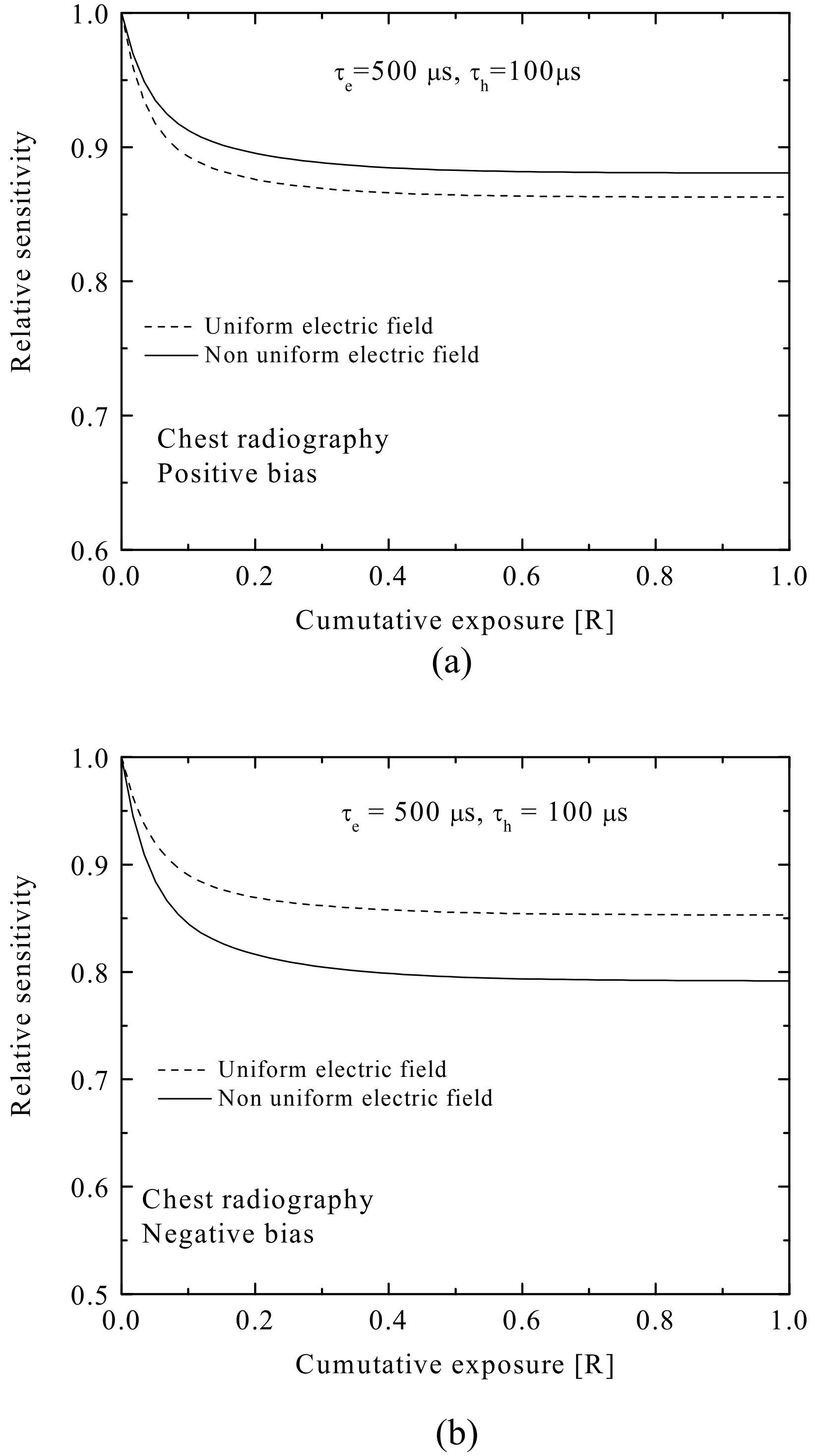

Figure 5.14 Nonuniform electric field effects on the relative sensitivity for chest radiographic applications. (a) Positively biased detectors and (b) negatively biased detectors.

In order to explain the bias and application dependent ghosting, we need to look at the electric field distribution inside the photoconductor. Figures 5.15 and 5.16 show the electric field distribution inside the photoconductor for the cases mentioned above. The electric field is normalized to the applied field and the photoconductor thickness is normalized to the photoconductor length. The electric field in every case, except for the positively biased chest radiographic detector, decreases at the radiation receiving electrode and increases at the bottom electrode. Since most x-ray photons are absorbed near the radiation receiving electrode, lower electric field at that side means a higher value of $W_{\pm}$ and thus less EHPs are expected to be generated (i.e., PGR is less than unity). Less PGR enhances ghosting in these cases. In the case of a positively biased chest radiographic detector, the electric field significantly increases at the radiation receiving electrode and decreases at the other side. The higher electric field at the radiation receiving electrode means more EHPs are generated and thus the PGR is now greater than unity. A greater carrier generation leads to lower ghosting in the positively biased chest radiographic detector. Different electric field distributions in different cases arise due to different trapped carrier (electrons and holes) distributions inside the photoconductor (the trapped carrier distributions were shown in figure 5.11 for a positively and negatively biased mammographic detector).

The contribution of the charge collection efficiency (CCE) and the photogeneration ratio (PGR) on the sensitivity are shown in figures 5.17 and 5.18 for the cases as mentioned above. As discussed above, in a positively biased mammographic detector, initially the PGR slightly goes above unity but finally it is less than unity. Both CCE and PGR have almost the same contribution to the relative sensitivity, as shown in figure 5.17 (a). But the effect of the electric field on the carrier generation in subsequent exposures is significant in the negatively biased mammographic detector as shown in the figure 5.17(b). Here the PGR decreases by almost 18% for a cumulative exposure of 20 R due to the huge change in the electric field distribution at the radiation receiving end as shown in figure 5.15 (b). As a result of this high reduction of PGR, the relative sensitivity decreases severely in the negatively biased mammographic detector. But the contribution of CCE to the relative sensitivity is around 3%.

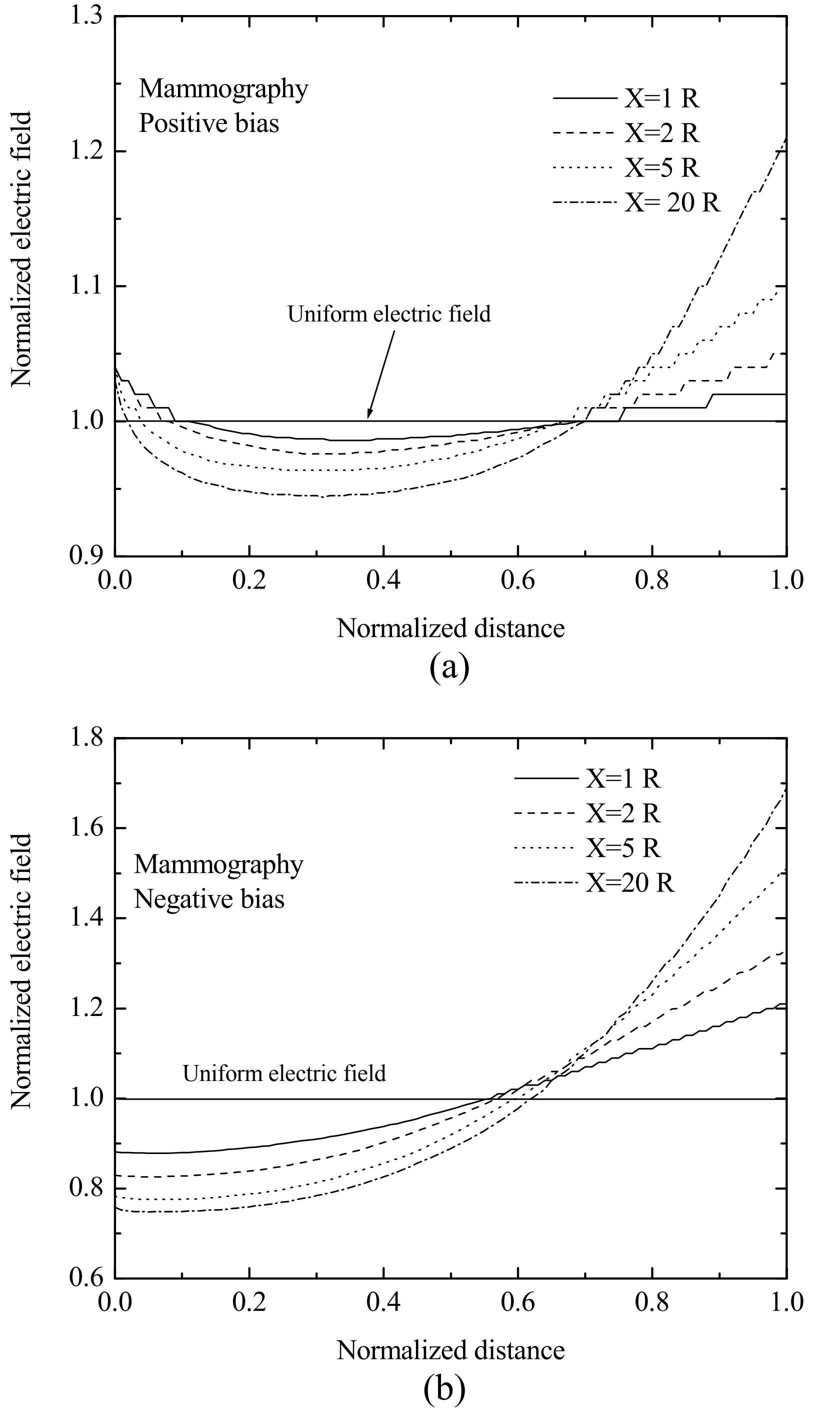

Figure 5.15 The normalized electric field versus normalized distance from radiation receiving electrodes after different x-ray exposures for mammographic applications. (a) Positively biased detectors and (b) negatively biased detectors.

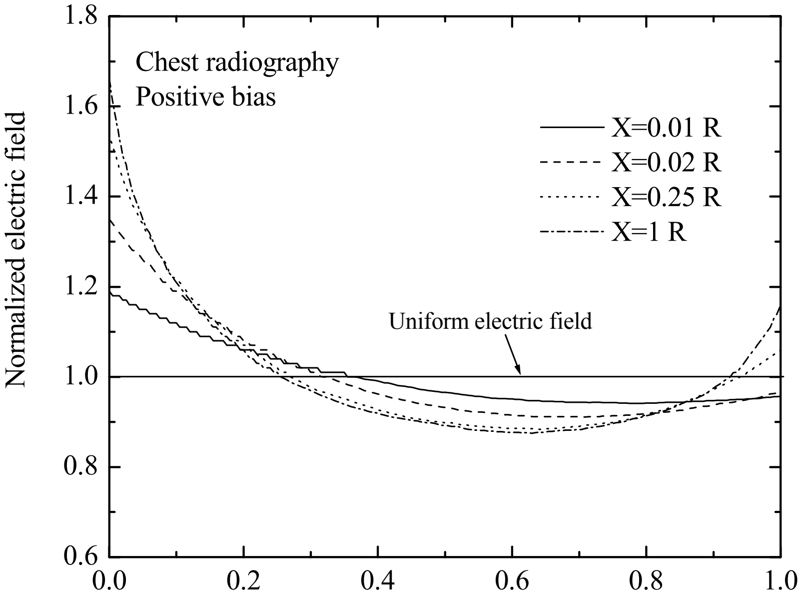

Normalized distance

(a)

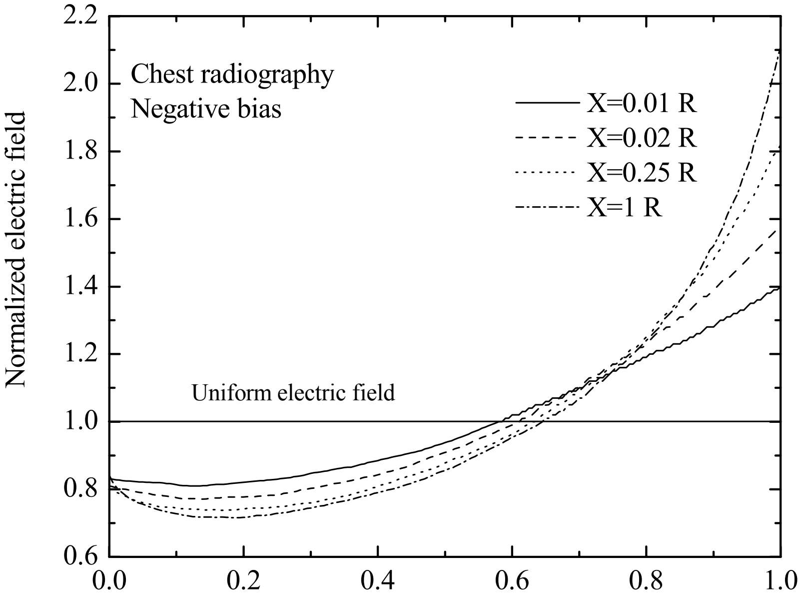

Normalized distance

(b)

Figure 5.16 The normalized electric field versus normalized distance from radiation receiving electrodes after different x-ray exposures for chest radiographic applications. (a) Positively biased detectors and (b) negatively biased detectors.

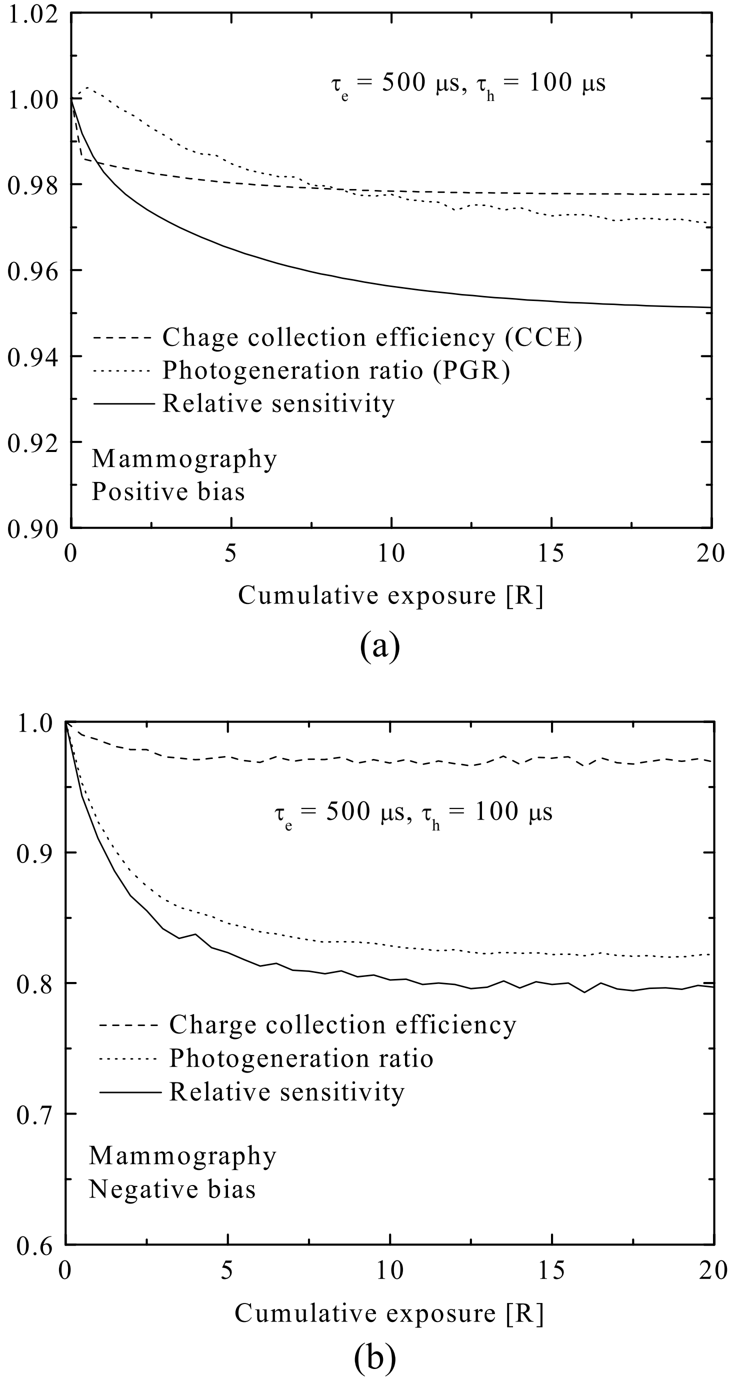

Figure 5.17 Charge collection efficiency (CCE), photogeneration ratio (PGR), and relative sensitivity versus cumulative x-ray exposure for mammographic applications. (a) Positively biased detectors and (b) negatively biased detectors.

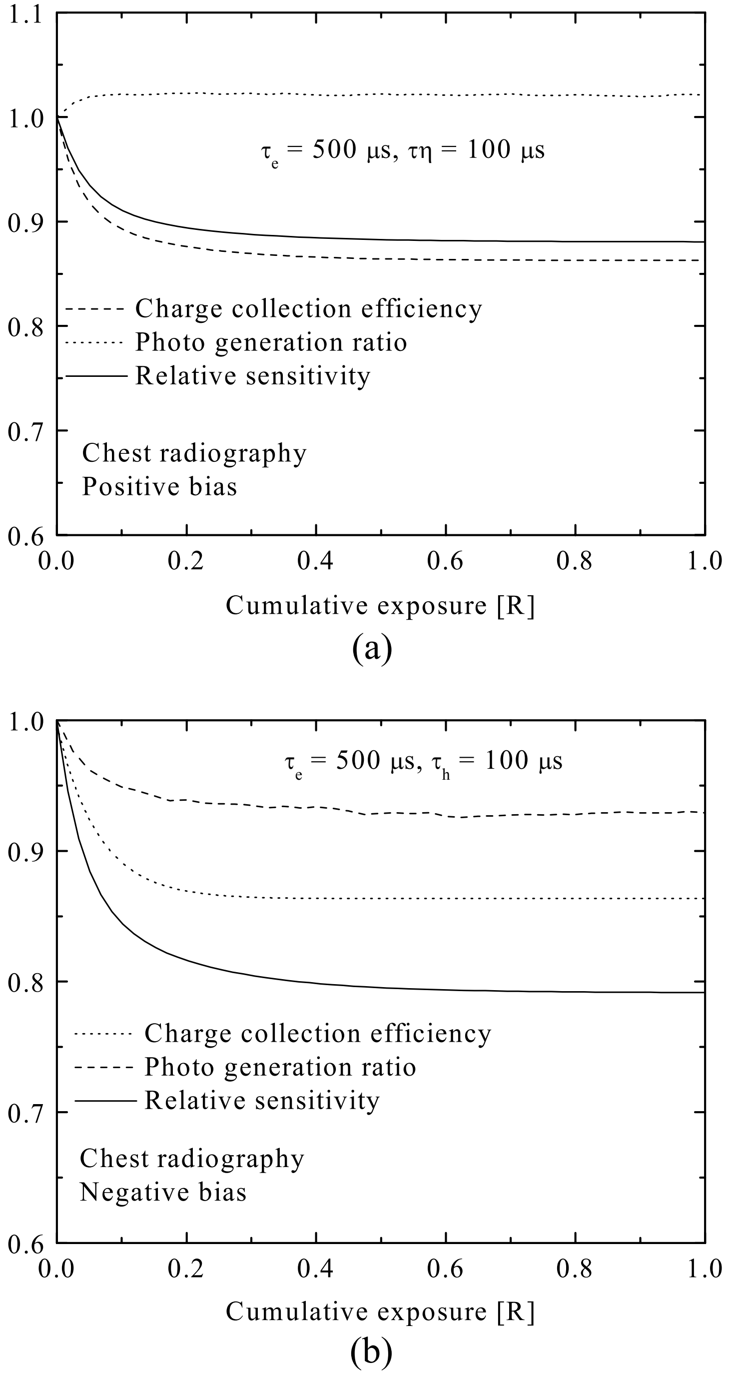

(a)

(b)

Figure 5.18 Charge collection efficiency (CCE), photogeneration ratio (PGR), and relative sensitivity versus cumulative x-ray exposure for chest radiographic applications. (a) Positively biased detectors and (b) negatively biased detectors.

For a positively biased chest radiographic detector, the PGR is greater than unity, as shown in figure 5.18 (a). This is due to the higher electric field distribution at the radiation receiving electrode, as discussed above. The contribution of CCE to the relative sensitivity is mainly dominant in chest radiographic detectors. For chest radiographic detectors, CCE decreases by almost 7-10 % for a cumulative exposure of 1 R. But the PGR is greater than unity in a positively biased chest radiographic detector and decreases by almost 14 % in a negatively biased chest radiographic detector.

It can be concluded that the effect of PGR is more prominent in negatively biased detectors (mammographic or chest radiographic) and CCE decreases significantly in chest radiographic detectors.

The saturation of ghosting discussed in section 5.3.1 applies here as well. Trapped carrier concentrations saturate as a result of the balance between several processes: the rate at which carriers are trapped, the rate at which trapped carriers are lost due to recombination, and trap filling effects. Once the trapped carrier concentration reaches a saturation level, the electric field does not change very much and hence there is no further reduction in the sensitivity neither from the CCE point of view nor from the PGR point of view. Our Monte Carlo simulation results show a good agreement with the numerical results, as shown in figure 5.19. The solid line is the numerical calculation while the solid circles represent our Monte Carlo results. The procedure for calculating ghosting numerically has been given in Ref. [46]. Although figure 5.19 shows the Monte Carlo simulation results and the numerical results only for a positively biased mammographic detector, for others cases, Monte Carlo simulations also show a good agreement with the numerical results, as mentioned in Ref. [46].

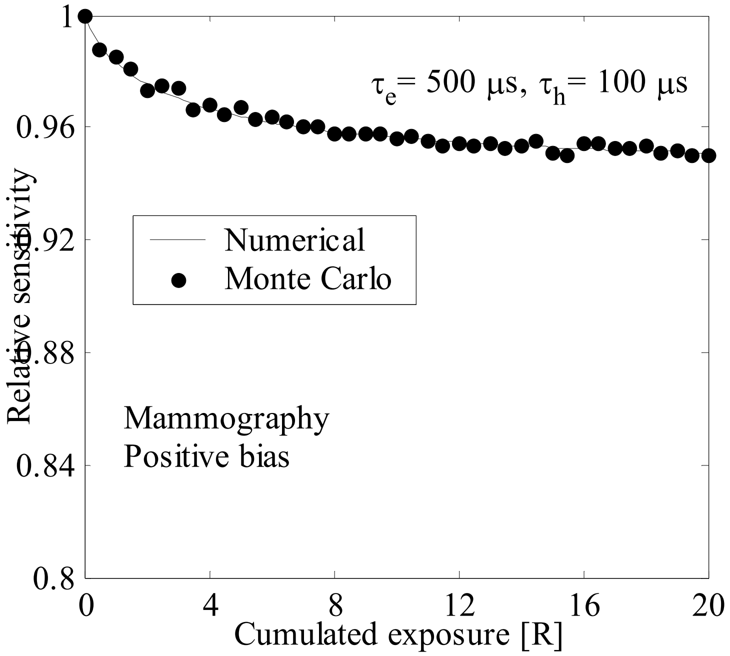

Figure 5.19 The relative sensitivity as a function of cumulative x-ray exposure for a positively biased mammographic detector.

5.3.4 Effects of X-ray induced Trap Generation

The effects of x-ray induced deep trap center generation are shown in figures 5.20 and 5.21 for mammographic and chest radiographic detectors, respectively, under positive and negative biasing conditions. The nature and amount of deep trap centers that are generated due to x-ray radiation have not yet been resolved. In our calculations, we have considered different levels of x-ray induced deep trap center generation. Again, the x-ray induced trap generation parameter, N_{X0}, (equation 4.22) depends on the photoconductor material and the irradiated energy. For mammographic applications with an average photon energy of 20 keV, two levels of N_{X0} have been assumed, 10×10^{13} /cm^3 and 20×10^{13} /cm^3, while for chest radiographic applications with an

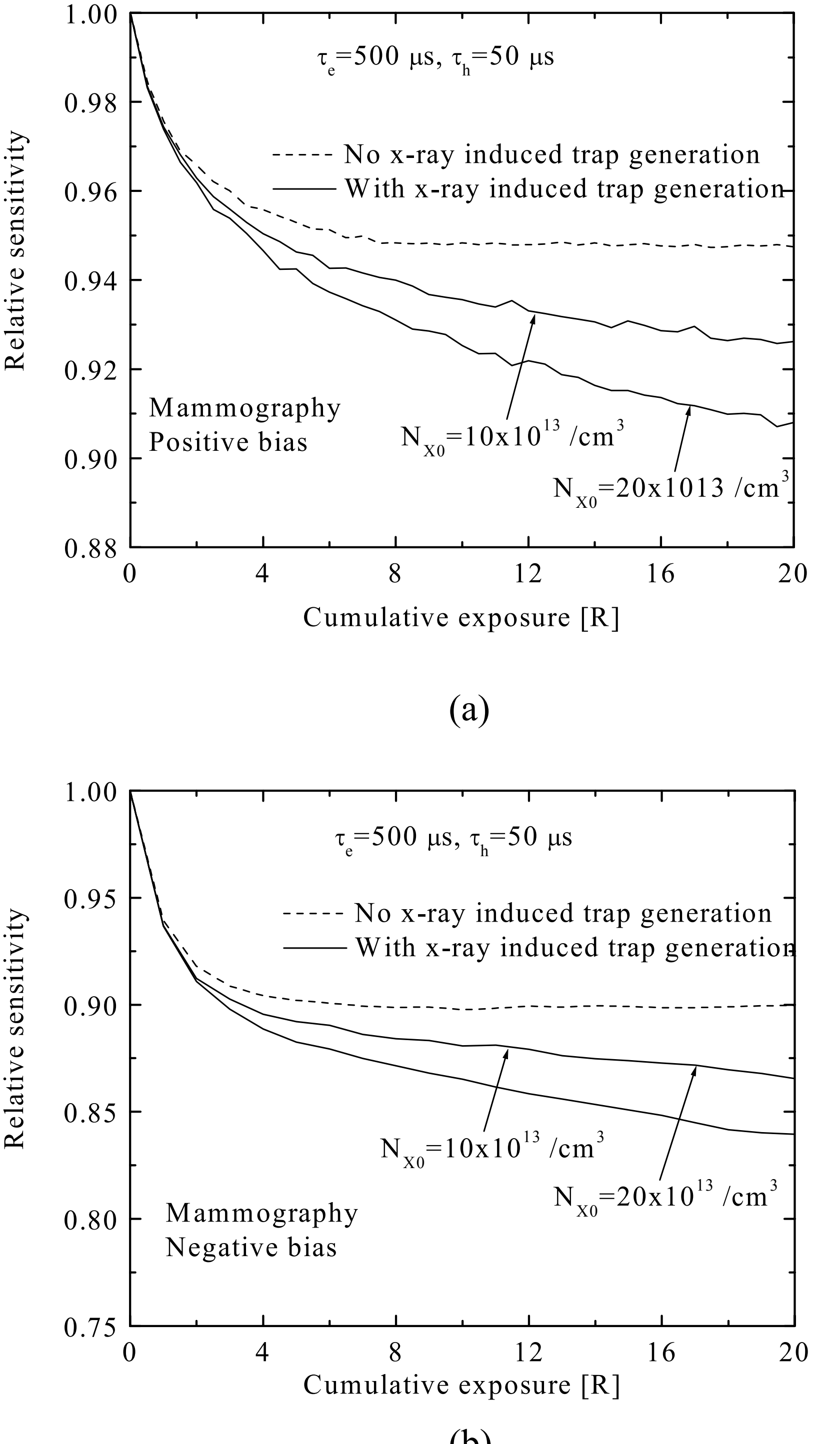

Figure 5.20 Effects of the x-ray induced deep trap center generation on the relative sensitivity for mammographic applications. (a) Positively biased detectors and (b) negatively biased detectors.

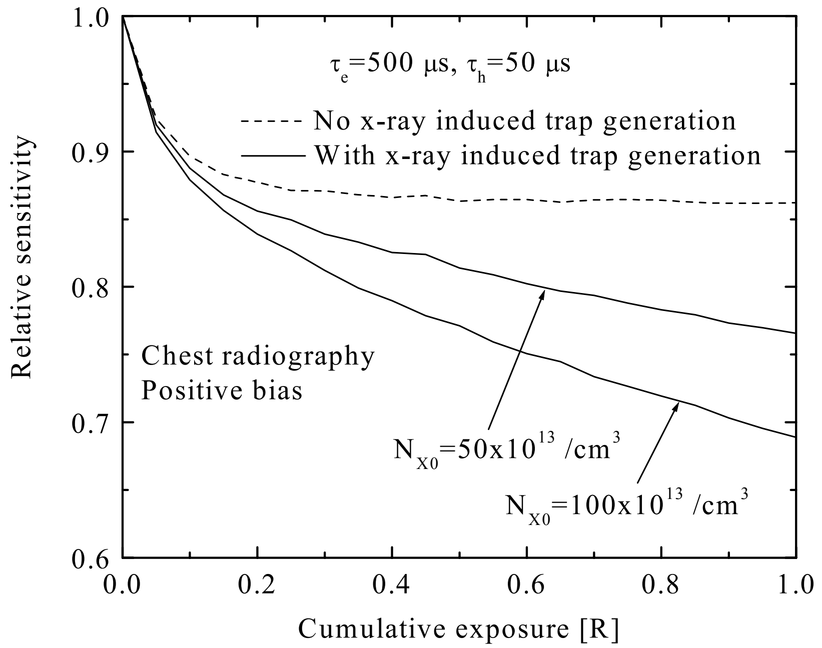

(a)

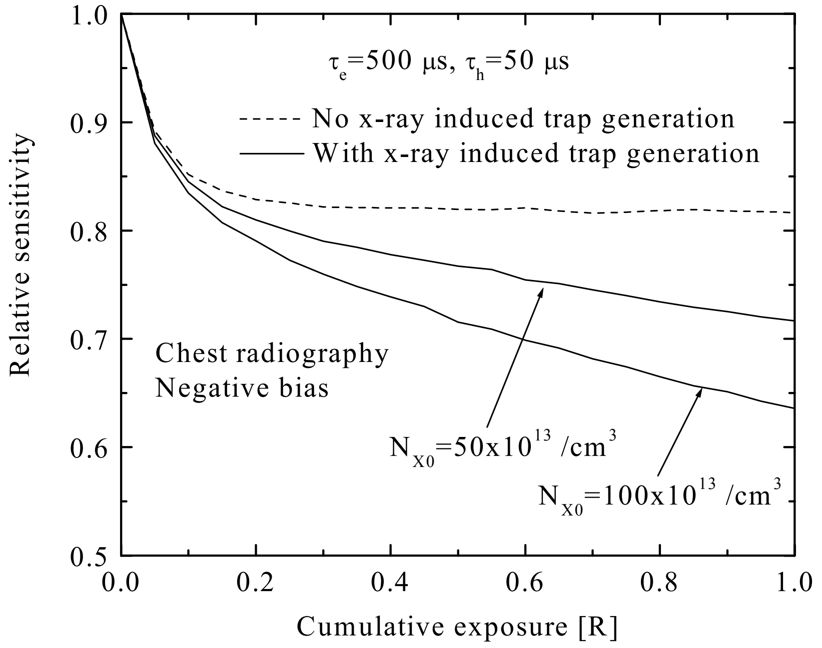

(b)

Figure 5.21 Effects of the x-ray induced deep trap center generation on the relative sensitivity for chest radiographic applications. (a) Positively biased detectors and (b) negatively biased detectors.

average photon energy of 60 keV, two levels of N_{X0} are assumed, which are 50×10^{13} /cm^3 and 100×10^{13} /cm^3. The value of the constant "*a*" (equation 4.24) is taken 20 R and with this value of "*a*", the x-ray induced deep trap center generation is almost linear with exposure for the range of exposures we have considered in our calculation. The solid lines show the simulation results considering the effects of x-ray induced deep trap center generation while the dashed line shows the results without considering such effects. It is found that when the effects of x-ray induced deep trap center generation are taken into consideration, ghosting tends to continue to increase with exposure. This means that the simulation results show no saturation of ghosting.

In the presence of new deep trap center generation, carrier trapping increases with exposure. The increase in the trap carrier concentration increases recombination. The new deep trap center generation decreases trap filling effects. All of these factors assist to increase ghosting with cumulative exposure. A nonuniform electric field has the same effect as discussed previously. Again, as expected, ghosting increases with a higher x-ray induced deep trap center generation. For mammographic applications, when the new deep trap center concentration has increased from 10×10^{13} /cm^3 to 20×10^{13} /cm^3, ghosting increases by about 2-3% for a cumulative exposure of 20 R. But the change of ghosting is almost the same for both positive and negative biasing conditions. The same scenario also appears in chest radiographic applications. For chest radiographic applications, when the x-ray induced deep trap center generation has increased from 50×10^{13} /cm^3 to 100×10^{13} /cm^3, ghosting increases by 7% for a cumulative exposure of 1R. In chest radiographic applications, the x-ray induced deep trapping is assumed to be greater due to the high x-ray photon energy; hence the change in ghosting is higher but the effects are almost same for both positive and negative biasing conditions. This means that bias is of little importance for ghosting and that it is due to x-ray induced trap generation.

5.3.5 Effects of Trapped hole Detrapping

The effect of trapped hole detrapping is shown in figures 5.22 (a) and (b) for a positively and negatively biased mammographic detector, respectively. The characteristic detrapping time of a trapped hole is taken to be five minutes and the rest time between successive exposures is taken to be one minute, with each exposure corresponding to 0.5 R. Although the detrapping time is assumed to be 5 minutes, the reported detrapping time of deep trapped holes varies between 10 s and 5 minutes. It is found that in the presence of trapped hole detrapping, ghosting decreases in the positively biased detector but ghosting is almost unaffected in the negatively biased detector.

As discussed earlier, hole trapping is more significant in a positively biased detector. During the rest time, a fraction of the trapped holes are released. Therefore, for the next exposure, the trapped hole concentration decreases, leading to a reduction of recombination between the trapped holes and drifting electrons. Consequently, ghosting decreases when we consider the detrapping of holes. But in the case of a negatively biased detector, electron trapping is important and hole trapping is unimportant. The amount of trapped holes that are being detrapped in the rest time is negligible. Since electron detrapping is negligible, the trapped carrier concentrations remain unaffected in the next exposure. Hence, there is no change of ghosting in a negatively biased detector when the detrapping of those carriers is considered.

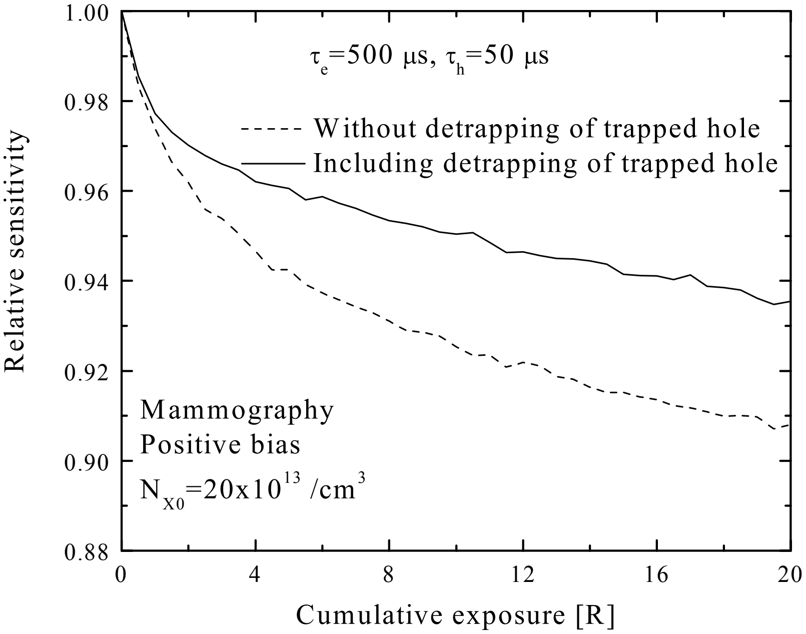

(a)

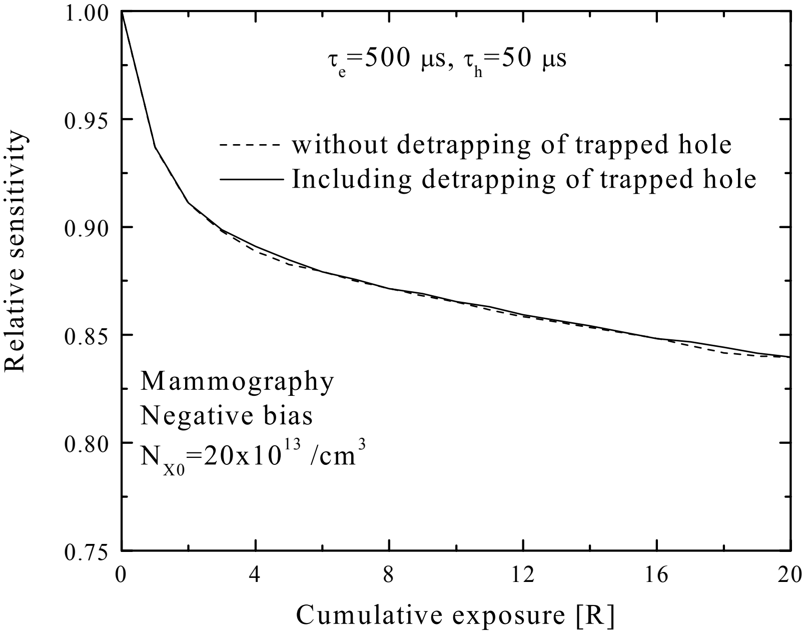

(b)

Figure 5.22 Effect of trapped hole detrapping on the relative sensitivity mammographic applications. (a) Positively biased detectors and (b) negatively biased detector.

5.4 Comparison with Experimental Data

The simulation results of the model discussed above are compared with the experimental results reported by Steciw et al. [17]. The latter work used an x-ray spectrum with 75 kV_p which corresponds to a mean photon energy of about 40 keV. This is the photon energy used in the calculation of ghosting. The effective attenuation coefficient is 2.5 mm Al and length of the photoconductor L is 239 μm as given in Ref. [17]. Figures 5.23 (a) and (b) show the relative sensitivity as a function of exposure for positively biased detector with an applied field of 2.9 V/μm and 1.7 V/μm. The solid line represents the simulation results considering all the effects discussed above and the circles indicate the experimental results (the experimental data has been extracted from figure7 of Ref. 17).

Electron and hole ranges ($\mu\tau$) were taken to be 1.95×10^{-6} cm^2/V and 5.4×10^{-6} cm^2/V, respectively, i.e. the electron lifetime is 650 μs and the hole lifetime is 45 μs. These values of electron and hole ranges are consistent with the published data [8]. N_{X0} for x-ray generated electron and hole deep traps are assumed to be 13×10^{13} $/cm^3$ and 6×10^{13} $/cm^3$ respectively (i.e., x-ray induced deep trap center generation for holes is higher than for electrons) and constant "*a*" is taken to be 40 R for both electron and hole new traps.

The unequal x-ray induced effects for electron and hole trapping have been reported by Schiebel et al. [44]. The simulation results show that after an initial sharp decrease, the sensitivity decreases slowly with exposure. The sudden decrease of the sensitivity is due to the high recombination rate between drifting carriers and oppositely charged trapped carriers. But the experimental data reveal that sensitivity decreases gradually with exposure i.e., the model does not match quantitatively with the experimental results.

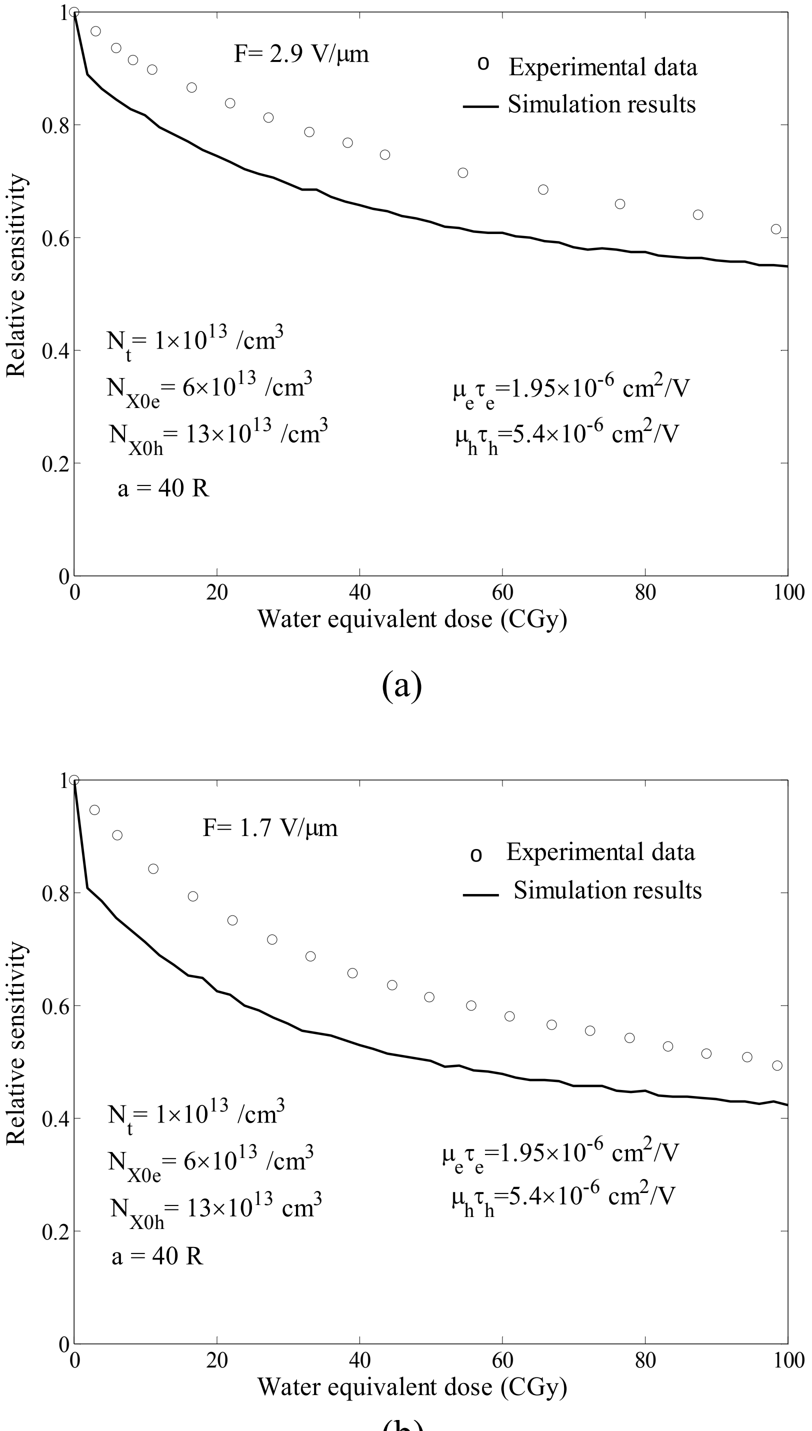

Figure 5.23 The relative sensitivity as a function of cumulative water equivalent dose. (a) Applied electric field is 2.9 V/μm and (b) applied electric field is 1.7 V/μm. The experimental data has been extracted from figure 7 of Ref. 17.

5.5 Modification of Recombination Coefficient

We modified the above model described in previously by allowing only a certain fraction *f* of trapped carriers to act as recombination centers for oppositely charged drifting carriers. For all practical purposes, this assumption is equivalent to assuming that there are two types of deep traps for each species of carriers: (I) neutral when empty and becomes charged when a carrier is trapped; (II) charged when empty and neutral when a carrier is trapped. Obviously the latter would participate in the recombination process. Again instead of recombining with a drifting hole, a trapped electron may recombine with a trapped hole, that is, belong to type C recombination as discussed in section 1.5. Although it is possible to reformulate the trapping and recombination kinetics with two distinct species of traps, and hence double the number of trapping parameters, and include the recombination between trapped electrons and trapped holes, it is much easier, and more productive, to simply assign a factor *f* to describe what portion of trapped carriers are involved in the recombination with oppositely charged drifting carriers. This effect can be included in our model replacing $C_t^{'}$ in equation 4.15 by $f \times C_t^{'}$, where *f* lies between 0 and 1. Now the recombination rate is $fC_L c_t^{'} c$ (equation 4.13). Stated differently, we are assigning an *effective recombination coefficient* fC_L, where C_L is the Langevin recombination coefficient, to describe the recombination of drifting carriers with trapped carriers in a-Se. It is well known that the a-Se structure has valence alternation pair (Se_3^+ and Se_1^-) type defects and must also have seemingly "neutral" traps that can generate a xerographic residual voltage [50]. Further the irradiation can generate defects in a-Se and the defects can also interconvert [47, 48]. Given the complicated nature of defects in the structure, and the current controversy on the density of states in a-Se, we do not speculate on the physics and chemistry of the deep trap centers, except to assume two types of deep centers as discussed above. A brief description of the defect centers in a-Se is discussed in appendix B. The simulation results considering all the effects mentioned above are shown Fig 5.24. In the calculations as shown in figure 5.24, we have found *f* =0.15 to be the best value for the model to fit the experimental data. As observed from the figure

5.24, there is a good agreement between the experimental data and the simulation results. It is apparent that x-ray exposure reduces the carrier life time and a fraction of the trapped carriers recombine with the free drifting carriers, which leads to ghosting.

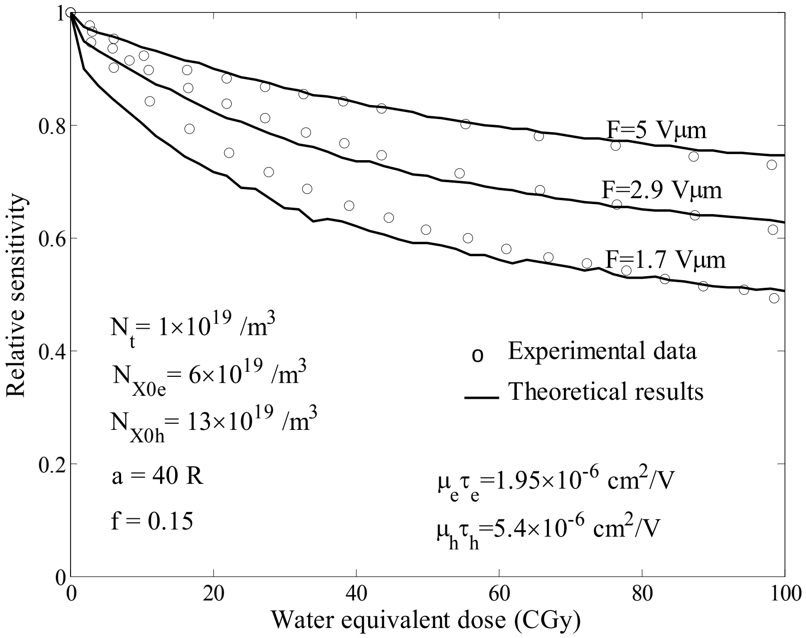

Figure 5.24 The relative sensitivity as a function of cumulative water equivalent dose. The experimental data has been extracted from figure 7 of Ref. 17.

The Monte Carlo model in this work has been further fitted with the experimental data supplied by the Anrad Corporation. Experiments were carried out on a typical a-Se detector for three different applied fields. The closed symbols in figure 5.25 show the measured relative sensitivity as a function of cumulative exposure for a negatively biased detector. The solid circles are for an applied field of 10 V/ μm, the solid squares are for an applied field of 6 V/ μm and the solid triangles are for an applied field of 3 V/ μm. The solid lines indicate the Monte Carlo simulation results considering the effective recombination coefficient *f* to be unity. The average photon energy taken is 55 keV for an applied 80 kV$_p$ x-ray spectrum. The measured $\mu\tau$ products for the carriers in this sample were 3.5×10^{-6} cm^2/V and 5.4×10^{-6} cm^2/V for electrons and holes, respectively.

With these values of $\mu\tau$ products for the electrons and holes, the values of mobility and carrier lifetime are 3.5×10^{-3} cm^2/V-s and 1000 μs for electrons, and the values of mobility and carrier lifetime are 12×10^{-2} cm^2/V-s and 47.5 μs for holes, respectively. Since the carrier lifetime is high, the assumed value for the initial deep trap center, N_t is 1×10^{12} /cm^3, for both electrons and holes. The photoconductor length is 1000 μm. The characteristic hole detrapping time is assumed to be 100 s. Each exposure is 6.5 mR and the rest time between exposures is 2 minutes. In the Monte Carlo simulation, we assumed the same x-ray induced trap generation parameters for different applied electric fields. The x-ray induced trap generation parameter, N_{X0}, for electrons and holes, are assumed to be 2.5×10^{12} /cm^3 and 7×10^{12} /cm^3, respectively (i.e., x-ray induced deep trap center generation for holes is higher than for electrons) and the constant "*a*" is 0.2 R for both electron and hole new traps. The simulation results seem in very good agreement with the experimental results.

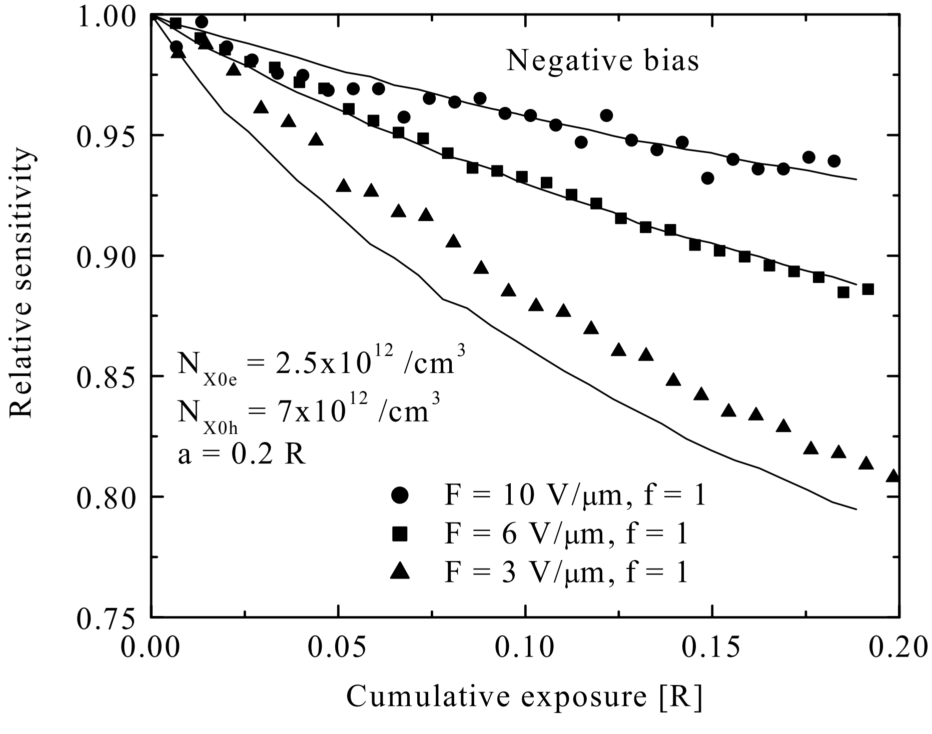

Figure 5.25 The relative sensitivity versus cumulative exposure for a negative biased a-Se detector with different applied electric fields. The experimental data has been supplied by the Anrad Corporation.

It is observed from figure 5.25 that the simulation results agree well with the experimental results for the applied fields of 10 V/μm and 6 V/μm but for the applied fields of 3 V/μm, the simulation results overestimated the experimental data. Although the overestimation of relative sensitivity at 3 V/μm is not significant it is still too large to ignore. We have tried to fit the experimental results with different x-ray induced effects. Figure 5.26 shows the simulation results with a different x-ray induced trap generation parameters. All the parameters, except N_{X0}, are the same as mentioned above. Here the x-ray induced trap generation parameter, N_{X0}, is assumed to be 2×10^{12} /cm^3 for electrons and 6×10^{12} /cm^3 for holes and the constant "*a*" is 0.2 R (same as the previous value). With these values for the x-ray induced trap generation parameters, it is observed that the simulation results fitted closely with experimental data at applied fields of 3 V/μm, but the simulation results underestimated the experimental results at applied fields of 10 V/μm and 6 V/μm.

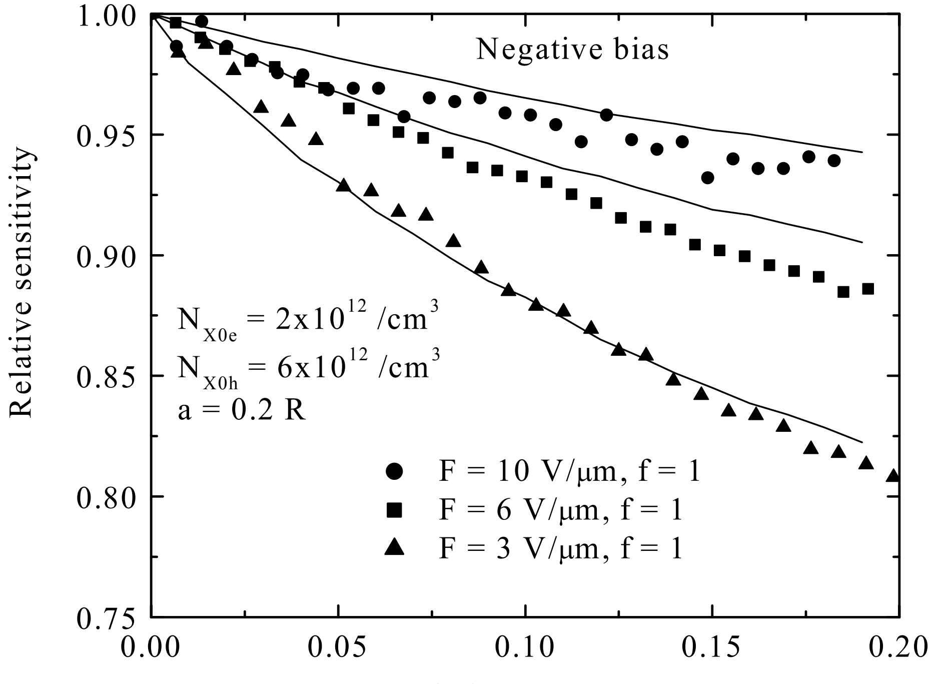

Figure 5.26 The relative sensitivity versus cumulative exposure for a negative biased a-Se detector with different applied electric fields. The experimental data has been supplied by the Anrad Corporation.

All the experimental results at different applied fields can not be fitted with the same x-ray induced deep trap center generation parameters within this model. We have therefore decided to include a modified recombination coefficient to fit the experimental results. The simulation results including a modified recombination coefficient are shown in figure 5.27. The electron trap center concentration is assumed to be 1.5×10^{12} /cm^3. Since selenium is alloyed with arsenic in stabilized a-Se, and the introduction of arsenic introduces hole traps, the assumed value for the hole trap center concentration is 3×10^{12} /cm^3. The x-ray induced trap centers are "twins" (traps for electrons and holes are pairs), so the assumed value of the x-ray induced trap generation parameters are same for both electron and hole new traps. The parameter, N_{X0}, is assumed to be 9×10^{12} /cm^3 and the constant "*a*" is assumed to be 0.4 R for both electrons and holes.

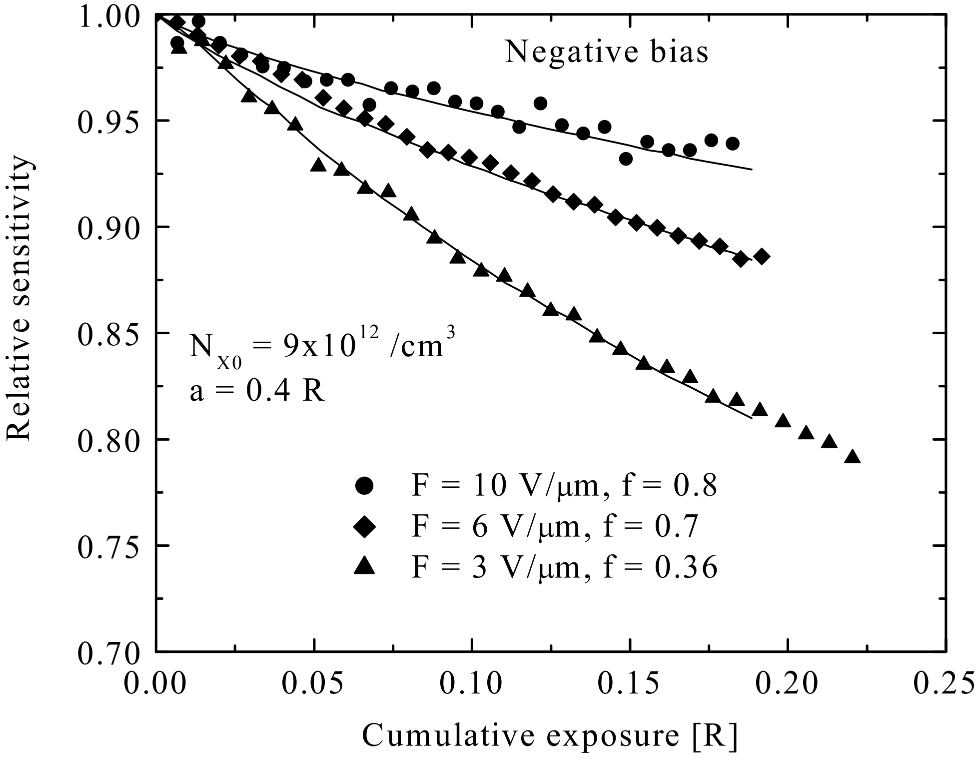

Figure 5.27 The relative sensitivity versus cumulative exposure for a negatively biased a-Se detector with different applied electric fields, including an effective recombination coefficient. The experimental data has been supplied by the Anrad Corporation.

The effective recombination coefficient *f*, is 0.8 at the applied field of 10 V/µm, 0.7 at the applied field of 6 V/µm, and 0.36 at the applied field of 3 V/µm. All other parameters are the same as mentioned in figure 5.25. At higher fields, the value of "*f*" is close to unity and at lower fields the value of "*f*" is less. One possible explanation is that at lower fields, more carriers are trapped, the recombination between trapped electrons and trapped holes becomes significant, and less trapped carriers are available for recombination with the drifting carriers. Hence, *f* is less at lower fields. However, it is very difficult to justify a significant recombination between trapped electrons and trapped holes. The simulation results seem to be in excellent agreement with the experimental results at all fields.

When we apply our model to a positively biased detector we obtain the results shown in figure 5.28. The same x-ray spectrum used in the negatively biased detector is also used for the positively biased detector, but the experiments are performed in a different sample. Since the same x-ray spectrum is used, the x-ray induced trap generation parameters are assumed to be same as mentioned previously. This means that the parameter N_{X0} is 9×10^{12} /cm^3 and the constant "*a*" is 0.4 R for both electrons and holes. The measured $\mu\tau$ products of the carriers in this particular sample are 2.2×10^{-6} cm^2/V and 3.5×10^{-6} cm^2/V for electrons and holes, respectively. With these values of $\mu\tau$ products for electrons and holes, the values of mobility and carrier lifetime are 3.5×10^{-3} cm^2/V-s and 629 µs for electrons, and the values of mobility and carrier lifetime are 12×10^{-2} cm^2/V-s and 29 µs for holes, respectively. Since the carrier lifetime in this case is almost double compared to the negatively biased detector, the deep trap center concentrations are assumed to be 3×10^{12} /cm^3 and 6×10^{12} /cm^3 for electrons and holes, respectively. In this case, the photoconductor length is 498 µm, each exposure is 20 mR and the rest time between two exposures is 2 minutes. The applied electric fields are 6 V/µm and 3 V/µm. The closed symbols are the experimental results and the solid lines are the Monte Carlo simulation results. The simulation results show an excellent agreement with the experimental results. The effective recombination coefficient *f* is 0.35 at the applied field of 6 V/µm, and 0.22 at the applied field of 3 V/µm.

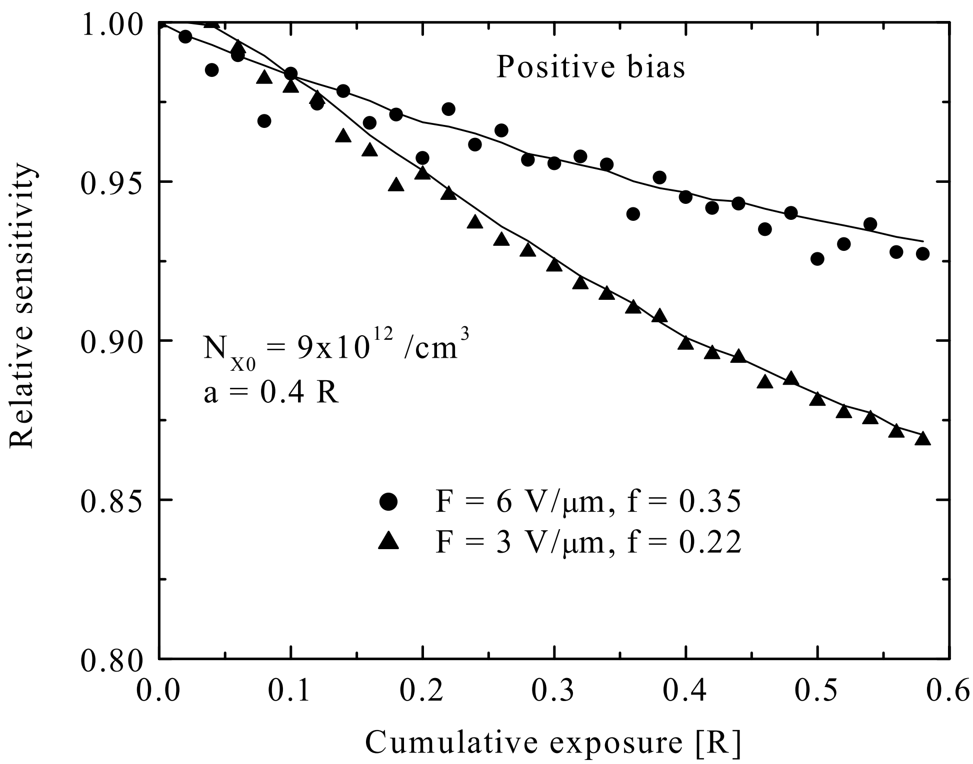

Figure 5.28 The relative sensitivity versus cumulative exposure for a positively biased a-Se detector with different applied electric fields including an effective recombination coefficient. The experimental data has been supplied by the Anrad Corporation.

We can easily examine the contribution of CCE and PGR to the relative sensitivity. We have considered only the applied electric field of 3 V/µm. Figure 5.29 shows the CCE and figure 5.30 shows the PGR for both positive and negative biasing at the applied field of 3 V/µm. From figure 5.29, it is observed that the CCE decreases gradually with cumulative exposure, but the reduction is more pronounced in a negatively biased detector. Although the carrier mobility lifetime product in the positively biased detector is lower than that of the negatively biased detector, the reduction of the CCE is more pronounced in the negatively biased detector. This is because carrier trapping is more significant in negatively biased detectors, and hence the recombination effect is more pronounced. Thus, the reduction of CCE is greater in negatively biased detectors.

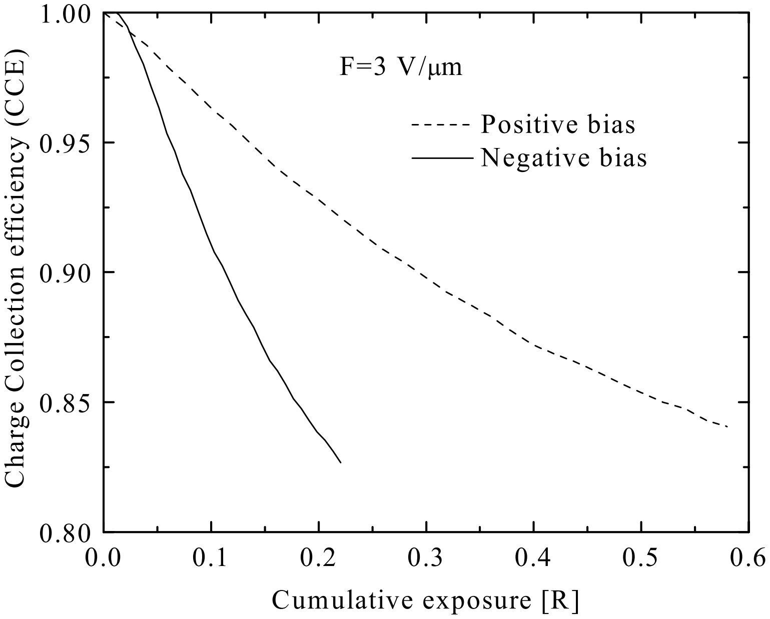

Figure 5.29 The charge collection efficiency versus cumulative exposure for both positive and negative biasing conditions. The applied electric field is 3 V/μm.

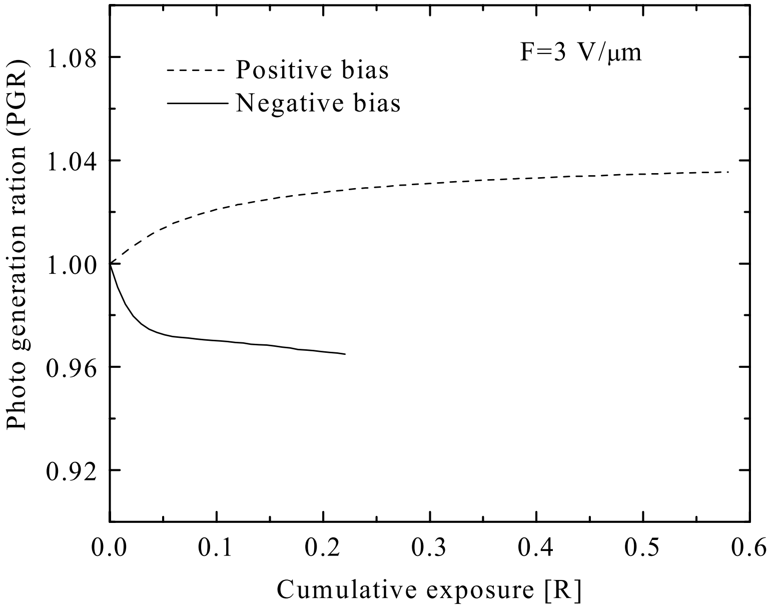

Figure 5.30 The photogeneration ratio versus cumulative exposure for both positive and negative biasing conditions. The applied electric field is 3 V/μm.

Another factor in favour of a higher reduction in the CCE in the negatively biased detector is that the photoconductor thickness used in the negatively biased detector is 1000 μm while the photoconductor thickness used in the positively biased detector is 498 μm. In the larger detector, the carrier trapping and hence recombination effects are more pronounced in the negatively biased detector. In a positively biased detector, the CCE decreases by 8 % for a cumulative exposure of 0.2 R, while for the same amount of cumulative exposure, the CCE decreases by almost 17 % in the negatively biased detector.

The effect of PGR is opposite in the positively and negatively biased detectors. The PGR is greater than unity in the positively biased detector but less than unity in the negatively biased detector. The PGR greater than unity in the positively biased detector or less than unity in the negatively biased detector is explained in figure 5.18 (a) and (b). In the negatively biased detector, the electric field distribution near the radiation receiving electrode where most EHPs are generated is low. Lower electric field at the radiation receiving side means a higher value of $W_{\pm}$ and less EHPs are generated. Thus, the PGR is less than unity in the negatively biased detector. In the case of the positively biased detector, the electric field distribution at the radiation receiving electrode is high, which ensures more EHP generation. Thus, the PGR is greater than unity in the positively detector. Finally it can be concluded that ghosting in a negatively biased detector occurs due to the reduction of both the CCE and the PGR, while ghosting in a positively biased detector occurs due to the reduction of CCE.

6. Conclusions and Recommendations

Ghosting mechanisms in x-ray photoconductors have been studied. The summary of this work and recommendations for future study are presented in this section.

6.1 Summary

Ghosting is the change of the x-ray sensitivity, or gain, of the detector as a result of previous exposures to radiation. In this work, ghosting mechanisms were modeled using a Monte Carlo simulation technique. We have calculated ghosting for chest radiographic and mammographic detectors under different biasing and operating conditions. The following effects are taken into account:

(i) Recombination between trapped and oppositely charged drifting carriers,
(ii) Trap filling effects,
(iii) Nonuniform electric field,
(iv) Detrapping of trapped holes, and
(v) The x-ray induced trap generation.

Our Monte Carlo simulation results are compared with experimental results and show good agreement.

Although previous explanations of ghosting are based on the recombination between trapped and oppositely charged drifting carriers, our calculations show that not only the recombination but also the x-ray induced trap generation is responsible for ghosting in x-ray photoconductor based detectors. The perturbation of the electric field also plays an important role in ghosting. The effects of trap filling are also non-trivial. Our calculations show that not all the trapped carriers take part in recombination, rather only a fraction of the trapped carriers act as recombination centers. A possible explanation for only a fraction of trapped carriers acting recombination centers has been put forward.

The amount of ghosting depends on biasing via the mobility lifetime product of the charge carriers. For positively biased detectors, ghosting is less if the mobility lifetime product of holes is higher than that of electrons and vice versa for negatively biased detectors. For an a-Se photoconductor, since the mobility lifetime product of holes is greater than that of electrons, ghosting is higher for negatively biased a-Se detectors. The sensitivity of a-Se photoconductor based detectors is higher and ghosting is less in positively biased detectors, thus from both points of view (higher sensitivity and less ghosting) positive biasing is preferred over negative biasing. Again, ghosting is higher in chest radiographic detectors than mammographic detectors. Chest radiographic detectors are much thicker than mammographic detectors. As a result, carrier trapping and recombination are more pronounced in chest radiographic detectors.

In conclusion, it can be seen that the reported ghosting (reduction in the sensitivity upon repeated exposure) in stabilized a-Se based x-ray detectors can be explained by deep carrier trapping, recombination of drifting carriers with oppositely charged trapped carriers, generation of new deep trap centers with exposure, and the modification of the internal field by trapped carriers (bulk space charge). All these effects are significant in the calculation of ghosting. Any approximation in the absence of x-ray induced deep trap center generation or a uniform electric field leads to a very large discrepancy between the calculated ghosting and the experimental data.

We only considered a-Se based x-ray image detectors because of the availability of ghosting data on this x-ray image detector. It would be useful to apply the above model to other x-ray photoconductors such as HgI_2 but there seems to be no readily available ghosting data on these detectors, although there is deep trapping in HgI_2.

The effect of bimolecular recombination on the charge collection efficiency is examined. It is found that the bimolecular recombination effect is not significant over typical exposure rates used in radiography. Bimolecular recombination becomes important when the exposure rate is over 100 R/s.

6.2 Suggestions for Future Work

Although this work shows a good agreement with experimental results, but there are still some effects that need to be explored. This work can be further extended by incorporating the following effects:

- We consider two types of recombination, recombination between oppositely charged drifting carries and recombination of trapped carriers with drifting carriers. The first one is negligible. But there can be another type of recombination, i.e. recombination between trapped carriers as explained earlier. The recombination between two trapped centers can be included for further study.

- As mentioned earlier, there are two types of trap centers in a-Se for each species of carriers: (I) neutral when empty and becomes charged when a carrier is trapped; (II) charged when empty and neutral when a carrier is trapped. Obviously the latter would participate in the recombination process. The neutral defect act as an amphoteric center. It can either trap an electron or a hole. So, it may be possible to reformulate the trapping and recombination kinetics with two distinct species of traps, and hence double the number trapping parameters.

- Although blocking contacts are used in photoconductive x-ray detectors to block carrier injection from the contacts and hence to minimize the dark current, a small amount of dark current flows through the photoconductor. The sources of this dark current are the thermally generated carriers in the sample and injected carriers from the contacts. Although the amount of dark current is insignificant, over the rest time period between successive exposures, the total injected carriers or the thermally generated carriers are not negligible. The injected or thermally generated carriers can neutralize some of the trapped carriers inside the photoconductor. It would be useful to include the effect of the dark current in future studies.

- X-ray photoconductors are pixellated. The electric field distribution of a pixellated detector is different than that from a single detector. It would be useful to explore the small pixel effects on the sensitivity and ghosting in a future study.

7. References

[1] S. R. Ovshinski, "Amorphous semiconductors for microelectronics," Proceedings from SPIE, 627, pp. 1-9, 1986.

[2] R. R. Carlton and A. M. Adler, *Principles of Radiographic Imaging: An art and Science*, 3rd edition.

[3] M. J. Yaffe and J. A. Rowlands, "X-ray detectors for digital radiography," Phys. Med. Biol., vol. 42, pp. 1-39, 1997.

[4] J. A. Rowlands and J. Yorkston, "Flat panel detectors for digital radiography," in *Handbook of Medical Imaging*, edited by J. Beutel, H. L. Kundel, and R. L. Van Metter, Washington, DC: SPIE, 2000, vol. 1, Ch. 4.

[5] K. Suzuki, "Flat panel displays using amorphous and monocrystalline semiconductor devices," in *Amorphous and Microcrystalline Devices: Optoelectronic devices*, edited by J. Kanicki, Boston, MA: Artech House, 1991, Ch. 3.

[6] L. E. Antonuk, J. Boudry, W. Wang, D. McShan, E. J. Morton, J. Yorkston, and R. A. Street, "Demonstration of megavoltage and diagnostic x-ray imaging with hydrogenated amorphous silicon arrays," Med. Phys., vol. 19, pp. 1455-1466, 1992.

[7] I. Fujieda, G. Cho, J. Drewery, T. Gee, T. Jing, S. N. Kaplan, V. Perez-Mendez, and D. Widermuth, "X-ray and charged particle detection with CsI(T1) layer coupled to a-Si:H photodiode layers," IEEE Trans. Nucl. Sci., vol. 38, pp. 255-262, 1991.

[8] S. O. Kasap and J. A. Rowlands, "Direct-conversion flat-panel x-ray image sensors for digital radiography," Proc. IEEE, vol. 90, pp. 591-603, 2002.

[9] T. Oguru, I. Kashima, M. Kanno, T. Higashi, T. Uehara, and B. T. Williams, "Ultra high resolution digital xeroradiography for x-ray microscopic detection," Japanese Med. Image Tech., vol. 7, pp. 279-280, 1989.

[10] http://www.anrad.com/english/page.asp.3.html, Anrad Corporation, 4950 Levy Street, Saint-Laurent, Quebec, Canada.

[11] D. L. Lee, L. K. Cheung, B. G. Rodricks, and G. F. Powel, "Improved imaging performance of a 14 × 17-in Direct Radiography System using a-Se/TFT detector," Proc. SPIE, vol. 3336, pp. 14-23, 1998.

[12] B. Polischuk, H. Tougeot, K. Wong, A. Debrie, E. Poliquin, M. Hansroul, J. P. Martin, T. T. Truong, M. Choquette, L. Laperriere, and Z. Shukri, "Direct conversion detector for digital mammography," Proc. SPIE, vol. 3659, pp. 417-425, 1999.

[13] M. Choquette, H. Rougeot, J. Martin, L. Laperriere, Z. Shukri, and B. Polishchk, "Direct selenium x-ray detector for fluoroscopy, R&F, and radiography," Proc. SPIE, vol. 3977, pp. 128-136, 2000.

[14] M. Choquette, Y. Demers, Z. Shukri, O. Tousignant, K. Aloki, M. Honda, A. Takahashi, and A. Tsukamoto, "Performance of real-time selenium based x-ray detector for fluoroscopy," Proc. SPIE, vol. 4320, pp. 501-508, 2001.

[15] B. Polischuk, S. Savard, B. Loustauneau, M. Hansrul, S. Cadîeus, and A. Vaqué, "Se-based flat-panel detector for screening mammography," Proc. SPIE, vol. 4320, pp. 582-589, 2001.

[16] O. Tousignant, Y. Demers, L. Laperriere, M. Nishiki, S. Nagai, T. Tomisaki, A. Takanashi, and K. Aoki, "Clinical performance of a 14-in. × 14-in. real-time amorphous selenium flat-panel detector," Proc. SPIE, vol. 5030, pp. 71-78, 2003.

[17] S. Steciw, T. Stanescu, S. Rathee, and B. G. Fallone, "Sensitivity reduction in biased amorphous selenium photoconductors," J. Phys. D, vol. 35, pp. 2716-2722, 2002.

[18] W. Zhao, G. DeCrescenzo, and J. A. Rowlands, "Investigation of lag and ghosting in amorphous selenium flat-panel x-ray detectors," Proc. SPIE, vol. 4682, pp. 9-20, 2002.

[19] S. O. Kasap, "X-ray sensitivity of photoconductors: application to stabilize a-Se," J. Phys. D: Appl. Phys., vol. 33, pp. 2853-2865, 2000.

[20] M. Z. Kabir and S. O. Kasap, “Charge collection and absorption-limited sensitivity of x-ray photoconductors: Application to a-Se and HgI_2,” Appl. Phys. Lett., vol. 80, pp. 1664-1666, 2002.

[21] R. A. Street, “Recombination in amorphous semiconductors,” Phys. Rev. B, vol. 17, pp. 3984-3995, 1978.

[22] J. A. Rowland and S. O. Kasap, “Amorphous semiconductors usher in digital x-ray imaging,” Phys. Today, vol. 50, pp. 24-30, 1997.

[23] S. O. Kasap and J. A. Rowlands, “X-ray photoconductor and stabilized a-Se for direct conversion digital flat-panel x-ray image detectors,” J. Mat. Sci.: Mat. Electron., vol. 11, pp. 179-198, 2000.

[24] S. O. Kasap and J. A. Rowlands, “Direct-conversion flat-panel x-ray image detectors,” IEE Proc.-CDS, vol. 149, pp. 85-96, 2002.

[25] S. O. Kasap, “Photoreceptors: the selenium alloys,” in *Handbook of Imaging Materials*, edited by A. S., Diamond (Marcel Dekker, New York, 1991) Ch. 8.

[26] R. A. Street, S. E. Ready, K. Van Schuylenbergh, J. Ho, J. B. Boyec, P. Nylen, K. Shah, L. Melekov, and H. Hermon, “Comparison of PbI_2 and HgI_2 for direct detection active matrix x-ray image sensors,” J. Appl. Phys., vol. 91, pp. 3345-3355, 2002.

[27] S. Tokuda, H. Kishihara, S. Adachi, T. Sato, “Preparation and characterization of polycrystalline CdZnTe films for large-area, high sensitivity X-ray detectors,” J. Mat. Sci.: Mat. Electron. vol. 15, pp. 1-8, 2004.

[28] M. Simon, R. A. Ford, A. R. Franklin, S. P. Grabowski, B. Menser, G. Much, A. Nascetti, M. Overdick, M. J. Powel, D. U. Wiechert, “PbO as direct conversion x-ray detector material,” Proc. SPIE, vol. 5368, pp. 188-199, 2004.

[29] G. Zentai, L. Partain, R. Pavlyuchkova, C. Proano, B. N. Breen, A. Taieb, O. Dagan, M. Schieber, H. Gilboa, and J. Thomas, “Mercuric iodide medical imagers for low exposure radiography and fluoroscopy,” Proc. SPIE, vol. 5368, pp. 200-210, 2004.

[30] G. Zentai, L. Partain, R. Pavlyuchkova, C. Proano, G. Virshup, L. Melekhov, A. Zuck, B. N. Breen, O. Dagam, A. Vilensky, M. Schieber, H. Gilboa, P. Bennet, K. Shah, Y. Dmitiev, J. Thomas, M. Yaffe, and D. Hunter, “Mercuric iodide and lead iodide x-ray detectors for radiographic and fluoroscopic medical imaging,” Proc. SPIE, vol. 5030, pp. 77-91, 2003.

[31] H. E. Johns and J. R. Cunnigham, *The Physics of Radiology*, 4th edition, 1983.

[32] C. A. Klein, "Bandgap dependence and related features of radiation ionization energies in semiconductors," J. Appl. Phys., vol. 39, pp.2029-2038, 1968.

[33] R. C. Alig and S. Bloom, "Electron-hole pair creation energies in semiconductors," Phys. Rev. Lett., vol. 35, no. 22, pp. 1522-1525, 1975.

[34] W. Que and J. A. Rowlands, "X-ray photogeneration in amorphous selenium: Geminate versus columnar recombination," Phys. Rev. B, vol. 51, pp. 10500-10507, 1995.

[35] I. M. Blevis, D. C. Hunt, and J. A. Rowlands, "Measurement of x-ray photogeneration in amorphous selenium," J. Appl. Phys., vol. 85, pp. 7958-7962, 1999.

[36] M. Lachaine and B. G. Fallone, "Monte Carlo simulation of x-ray induced recombination in amorphous selenium," J. Phys. D, vol. 33, pp. 1417-1423, 2000.

[37] L. Onsager, "Initial recombination of ions," Phys. Rev., vol. 54, pp. 554-557, 1938.

[38] J. Hirsch and H. Jahankhani, "The carrier yield in a-Se under electron bombardment," J. Phys.:Condens. Matter, vol. 1, pp. 8789-8798, 1989.

[39] G. Jaffe, "Zur Theorie de Ionisation in Kolonnen," Ann. Der Phys., vol. 42, pp. 303, 1913.

[40] W. Shockley, "Currents to conductors induced by a moving point charge," J. Appl. Phys., vol. 9, pp. 635-636, 1938.

[41] S. Ramo, "Currents induced by electron motion," Proc. I. R. E., pp. 584-585, 1939.

[42] C. Haugen and S. O. Kasap, "Langevin recombination of drifting electrons and holes in stabilized a-Se (Cl doped a-Se: 0-3% As)," Philos. Mag., vol. 71, pp. 91-96, 1995.

[43] S. O. Kasap, Bud Fogal, M. Z. Kabir, and R. E. Johanson, "Recombination of drifting electrons in stabilized a-Se photoconductors: Langevin recombination," Appl. Phys. Lett., vol. 84, pp. 1991-193, 2004.

[44] U. Schiebel, T. Buchkremer, G. Frings, and P. Quadflieg, "Deep trapping and recombination in a-Se:As x-ray sensitive photoreceptors," J. Non-Cryst. Solids, vol. 115, pp. 216-218, 1989.

[45] M. Abkowitz and R. C. Enck, "Photoenhanced metastable deep trapping in amorphous chalcogenides near room temperature," Phys. Rev. B, vol. 27, pp. 7402-7410, 1991.

[46] M. Z. Kabir, M. Yunus, and S. O. Kasap, "Dependence of x-ray sensitivity of direct conversion x-ray detectors on x-ray exposures and exposure history," Proc. SPIE, vol. 5368, pp. 170-176, 2004.

[47] D. K. Biegelsen and R. A. Street, "Photoinduced defects in chalcogenide Glasses," Phys. Rev. Lett., vol. 44, pp. 803-806, 1980.

[48] A. V. Kolobov, H. Oyanagi, K. Tanaka, and Ke. Tanaka, "Structural study of amorphous selenium by in *situ* EXAFS: observation of photoinduced bond alternation," Phys. Rev. B, vol. 55, pp. 726-734, 1997.

[49] http://physics.nist.gov/PhysRefData/XrayMassCoef/cover.html, 1997, J. H. Hubbel and S. M. Seltzer.

[50] M. Kastner, D. Adler, and H. Fritzsche, "Valence alternation model for localized gap states in lone pair semiconductors," Phys. Rev. Lett., vol. 37, pp. 1504-81507, 1976.

Appendix A

Random Number Generators

A random sequence is a vague notion in which each term is unpredictable and whose digits pass a certain number of traditional statistical tests. All random number generators are based on the theory that has a finite set R and a function, $f: R \rightarrow R'$ which takes elements of R into other elements of R'. For a given initial value (which is called *seed*) $r \in R$, the generated sequence is

$$r, f(r), f^2(r), f^3(r), \ldots,$$

where $f^2(r)$ means $f(f(r))$, $f^3(r)$ means $f(f(f(r)))$ and so on. There are five common classes of random number generators. These are (1) *multiplicative congruential* generators, (2) *shift register* generators, (3) *lagged Fibonacci* generators, (4) *add with carry* generators, and (5) *subtract with borrow* generators. A brief description of these generators is given below.

Multiplicative Congruential Generators

The finite set R is generated from an initial seed value r_0. Here $f(r) = (ar + b)\text{mod } m$. Thus the generator uses three integer parameters a, b, and m and a seed value r_0. The generation sequence is $r_{k+1} = (ar_k + b) \text{ mod } m$. As an example, with $a = 13$, $b = 0$, $m = 31$, and $r_0 = 1$, the generation sequence is 1, 13, 14, 27, 10, 6, 16, 22, 7, 29, 5, 3 ………which produces a random integer sequence with values between 0 and (m-1).

These numbers can be scaled by dividing by m to give floating point numbers uniformly distributed in the interval [0-1]. The number sequence repeats at regular interval which is called its *period*. Using multiplicative congruential generators, the maximum period that can be obtained is m. Computer memory allocation for an integer value is 4 bytes (32 bits), which means that the maximum period that can be achieved with this generator is 2^{31}-1.

Shift Register Generators

The finite set R is the set of $1 \times k$ binary vectors, $\mathbf{r} = (b_1, b_2,\ldots, b_k)$ and the function f is a linear transformation, $f(r) = rT$ where T is a $k \times k$ binary matrix and all the elements of T are arithmetic mod of 2. With an initial binary vector $\mathbf{r}$, the generation sequence is $\mathbf{r}$, $\mathbf{r}T$, $\mathbf{r}T^2$, $\mathbf{r}T^3$ and so on. Matrix T is carefully chosen so that the period is long and multiplication by T is reasonably fast in computer implementation.

Lagged Fibonacci Generators

In lagged Fibonacci generators, the random numbers are generated from a set of $1 \times n$ seed vectors $(r_1, r_2, \ldots\ldots\ldots, r_n)$. The generation of i^{th} element in the sequence involves an "arithmetic operation" step, where one number in the set of seeds is replaced by the addition of two other elements of the sequence. If the seed values are $r_1, r_2, \ldots\ldots, r_n$. The generation sequence is

$$r_i = r_{n-l1} + r_{n-l2} \qquad \text{if } r_{n-l1} + r_{n-l2} < m$$

$$r_i = r_{n-l1} + r_{n-l2} - m \qquad \text{if } r_{n-l1} + r_{n-l2} > m$$

Here l_1 and l_2 are chosen arbitrarily between 1 and n. The summation is reduced residues of m, where m is the period of the sequence.

Add with Carry Generators

Add with carry generators is a modified version of lagged Fibonacci generators. But the advantage of add with carry generators is that its period can be made enormous with the limiting memory space of computer. The generation sequence of the i^{th} element is given by

$r_{\mathrm{i}} = r_{n\text{-}l1} + r_{n\text{-}l2} + c$ if $r_{n\text{-}l1} + r_{n\text{-}l2} + c < m$

$r_{\mathrm{i}} = r_{n\text{-}l1} + r_{n\text{-}l2} + c - m$ if $r_{n\text{-}l1} + r_{n\text{-}l2} + c > m$

Here c is the carry bit of previous step which can be either 0 or 1. If $r_{n\text{-}l1} + r_{n\text{-}l2} + c < m$, than c is set to 0 and if $r_{n\text{-}l1} + r_{n\text{-}l2} + c > m$, than c is set to 1.

Subtract with Borrow Generators

Subtract with borrow generators are similar to add with carry generators. Here instead of addition subtraction is used. The generation sequence is

$r_{\mathrm{i}} = r_{n\text{-}l1} - r_{n\text{-}l2} - c$ if $r_{n\text{-}l1} - r_{n\text{-}l2} - c > 0$

$r_{\mathrm{i}} = r_{n\text{-}l1} - r_{n\text{-}l2} - c + m$ if $r_{n\text{-}l1} - r_{n\text{-}l2} - c < m$

Here carry bit c is set to 1 if $r_{n\text{-}l1} - r_{n\text{-}l2} - c < 0$ and c is set to 0 if $r_{n\text{-}l1} - r_{n\text{-}l2} - c > 0$.

Appendix B

Defects in a-Se

The defect centers in a-Se are described as dangling bonds. These defects arise due to the distortion of normal two fold coordination of selenium atom; the dangling bond contains an unpaired electrons. Depending on the occupied electrons in the dangling bond, the defect states can be D^+, D^0, and D^- for zero, one, and two occupied electrons respectively. Figure B.1 pictures the bonding schemes possible in a-Se [50]; the lowest energy bonding state, Se_2^0 (which represents the twofold coordinated structure) is considered as the "normal" structure; the other possible states are considered as defects.

The lowest energy electrically neutral defect is the trigonally coordinated atom, Se_3^0, as shown in figure B.1 (d). The three p-shell electrons enter into bonding states, and the fourth electron enters into an antibonding state. Another common electrically neutral defect is Se_1^0 as in figure B.1 (b). These defects possess three p-shell electrons which reside in nonbonding states, and one electron available for bonding. These neutral defects are denoted by D^0 as mentioned above. Instead of neutral defects D^0, a-Se film contains a large number of thermodynamically derived charged structural defects called *valence alternation pairs* (VAPs), which corresponds to some of the Se atoms being over-or under-coordinated. The under-coordinated defect is Se_1^- as in figure B.1 (c) and the over-coordinated defect is Se_3^+ as in figure B.1 (e). The Se_1^- defect is denoted by D^- and Se_3^+ defect is denoted by D^+ as mentioned above. The pair of charged centers of the type Se_1^- and Se_3^+ are termed as VAP. If the atoms of the pair are in close proximity, they are termed as an *intimate valence alternation pair* (IVAP).

According to Ref. [47, 48], the photo induced or x-ray induced defects are also close pairs of D^+ and D^- centers. D^+ and D^- centers act as a trapping center for drifting electrons and holes respectively. The D^0 center acts as an amphoteric center; it can trap either an electron or a hole.

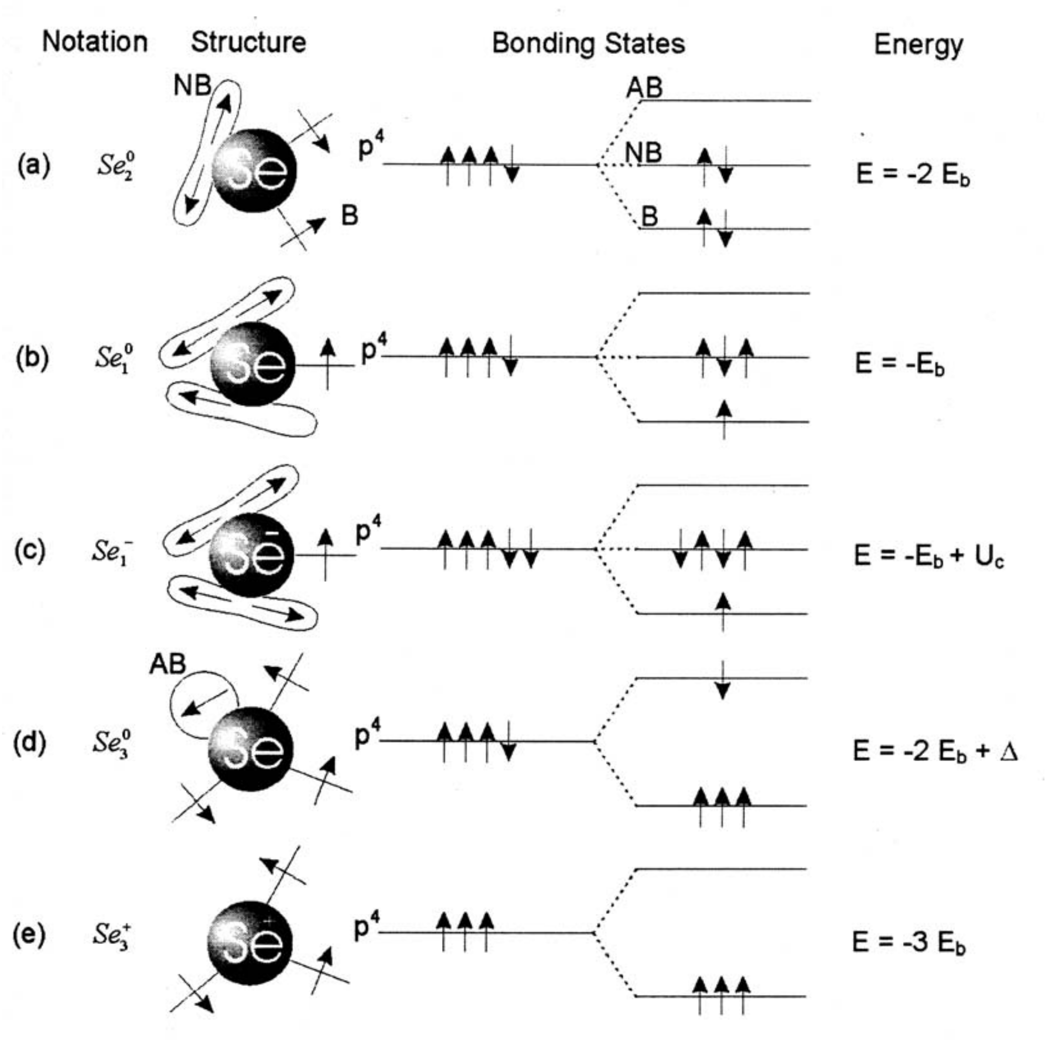

Figure B.1 Structure and energy of simple bonding configuration for selenium atoms. Straight lines represent bonding orbitals, lobes represents lone-pair (nonbonding) orbitals, and circles represent antibonding orbitals. The energy of lone-pair is taken as the zero energy (Ref. 50).

A trapped hole in D^- center can recombine with a conduction band electron; similarly a trapped electron in D^+ center can recombine with a valence band hole. Electrons trapped in D^+ centers form D^0 centers and holes trapped in D^- centers also form D^0 centers. But at steady state condition, experiments carried out on a-Se samples found that there are no electron spin resonance (ESR) signals. The absence of ESR signal is indicative of no unpaired electrons in the structure. But the D^0 (Se_1^0 and Se_3^0) centers have unpaired electrons as shown in figure B.1 (b) and (d). This means that there cannot be a singly bonded neutral selenium atom, Se_1^0, or triply bonded neutral atom, Se_3^0 in equilibrium condition.

It is energetically more favourable to form the pair of over- and under-coordinated atoms than it is to form singly bonded defects, as these singly bonded defects are some what unstable. From the figure B.1, we can see that for a VAP (Se_1^- and Se_3^+), total energy required is $-4E_b+U_c$, while for a pair of singly coordinated neutral defect Se_1^0 and trigonally coordinated neutral defect, Se_3^0, total energy required is $-3E_b+\Delta$. Here $-E_b$ is energy per electron of any bonding orbital, independent of the nature of the bond. Since antibonding orbitals are always pushed up in energy more than bonding orbitals are pushed down, the energy of a anti bonding orbital is $E_b+\Delta$, where $\Delta>0$. Whenever, an additional electron is placed on an atom, there is an increase in energy due to electronic correlation; U_c is the correlation energy to place the electron in a single localized lone pair (LP) orbital. It is assumed that E_b is considerably larger than Δ or U_c. Hence the total energy of a pair of neutral defects (Se_1^0 and Se_3^0) is higher than the total energy of VAP. Therefore with course of time, the two neutral defects can change to VAP by exchanging an electron. This means, the trapped electrons in D^- centers (form D^0 centers) are supposed to recombine with drifting holes and trapped holes in D^+ centers (form D^0 centers) are supposed to recombine with drifting electrons; instead of recombining with drifting carriers, the two trapped carriers (two D^0 centers) can change to D^+ and D^- centers by exchanging an electron, i.e. $2D^0 \rightarrow D^+ + D^-$